PhD Thesis
Improved beam extraction for a negative hydrogen ion source for the LHC injector chain upgrade, Linac4

Øystein Midttun
University of Oslo & CERN

November 21, 2014

Series of dissertations submitted to the
Faculty of Mathematics and Natural Sciences, University of Oslo
No. 1585

ISSN 1501-7710

Cover: Hanne Baadsgaard Utigard.
Printed in Norway: AIT Oslo AS.

Produced in co-operation with Akademika Publishing.
The thesis is produced by Akademika Publishing merely in connection with the
thesis defence. Kindly direct all inquiries regarding the thesis to the copyright
holder or the unit which grants the doctorate.

Preface and acknowledgements

I first started my work on ion sources with a fellowship for the commissioning of the Linac4 H^- ion source. The commissioning did not go as expected, and it became evident that a new extraction system was needed in order for the ion source to deliver an H^- beam with the required energy. I then transformed my work into a study for the design of a new beam extraction system for the ion source.

I would like to express my gratitude towards my two supervisors for making this work possible. Steinar Stapnes kindly agreed to let me join the University of Oslo, and made sure all the administrative work was done in an orderly fashion and on time. Richard Scivens took me under his wing as a PhD student after I finished my fellowship in the Hadron Sources and Linacs section at CERN. He has served as a great inspiration of how one can work as a leader without stressing or panicking, and finding time to show newcomers around and give detailed explanations about ion sources and accelerators.

I would also like to thank Jacques Lettry who has worked hard to build several prototypes of new ion sources and extraction systems. Because of the tight production schedule, there was plenty of time left for me to test the new extraction system.

Special thanks to Taneli Kalvas who wrote the plasma extraction simulation code IBSimu. This tool was indispensable during my work, and made it possible to "look" inside the beam extraction system, which for most is considered to be a black box.

My time at CERN would not be so pleasant without my colleagues and friends. Daily coffee meetings were held for either discussing today's measurement plan or last night's football game. Thanks to: Patrik Andersson, Sebastien Bertolo, Daniel Fink, Christiano Mastrostefano, Stefano Mattei, Matthias Kronberger, Michael O'Neill, Fadmar Osmic, Iulia Pascu, Hugo Pereira, Juergen Pfingstner, Jose Sanchez Arias, Claus Schmitzer, and Cristhian Alfonso Valerio-Lizarraga. Also thanks to Yngve Levinsen for all help with setting up this document, and for keeping the door open for the most basic accelerator questions.

I thank my parents for their support, and my brother for making me interested in science at an early age.

Last, but no least, I would like to thank my wife, Elisabeth. Not only did she support me to start this PhD, she encouraged me. Throughout the whole time she kept on inspiring me to continue, and let me stay on working in order to finish. Finally I thank our son Henrik for providing me the necessary distraction during the finalization of this thesis.

Abstract

In the scope of an upgrade of the injector chain of CERN's accelerator complex, a new linear accelerator, Linac4, is under construction. This accelerator will replace the existing 50 MeV proton linac, Linac2. By increasing the beam energy to 160 MeV, Linac4 makes it possible to double the brightness in the PSB, and ultimately increase the luminosity in the LHC.

Linac4 will accelerate beams of negative hydrogen (H^-) to be injected into the PSB by multi-turn, charge exchange injection. The ion source was initially based on the non-caesiated RF-volume source from DESY. However, the beam extraction from this source could not handle the 45 keV beam energy required by the RFQ. A new beam extraction system has therefore been designed, via IBSimu simulations [1], to extract and transport the H^- ion beam respecting the Linac4 requirements. Key features of the extraction system is a tuneable puller voltage to adapt the extraction field to the ion and electron beam currents, and a magnetized Einzel lens to dump the co-extracted electrons with an energy below 10 keV.

This new extraction system has been successfully commissioned at the Linac4 ion source test stand, and is currently being used during the commissioning of the components of Linac4. An H^- beam peak current of 60 mA has been measured at the test stand, and long-term stable H^- beams of 35 mA have been demonstrated. The extraction system is flexible for the connection of different plasma generators, and can also be used to extract a proton beam by inverting the polarities of the high voltage transformers.

Contents

Chapter 1

Introduction

Particle accelerators have, since the days of the cathode ray tubes in the 1890s, evolved as tools of basic science. Even though most of today's accelerators rely on the same principle of resonance acceleration that Norwegian engineer Rolf Widerøe explored when he built the world's first accelerator in 1928, particle accelerators have come a long way since then, creating brighter beams of particles with greater energies than previously imagined possible. Besides basic science, particle accelerators cover various applications, and exciting new technology. The development of fusion reactors relies on accelerator driven systems, both for magnetically confinement and inertial fusion. Accelerators are also foreseen to drive next-generation reactors that burn non-fissile fuel, such as thorium, that can be burned with the use of particle beams. In medicine, hadron beam therapy has improved cancer treatment by maximizing the beam energy delivered to a tumour while minimizing the damage to normal tissue. In addition, particles accelerators are essential in the semiconductor industry to manufacture computer chips, and they are as well widely used for material analysis and small-scale imaging. [2]

Today's largest and most powerful particle accelerator is the 27-km-circumference Large Hadron Collider (LHC) at CERN in Geneva, Switzerland. As part of an upgrade of CERN's accelerator complex, a new linear accelerator for negative hydrogen (H^-) ions, Linac4, is under construction. Linac4 is intended to replace the currently operating proton accelerator, Linac2, to provide an initial condition for increasing the luminosity in the LHC. The negative ion beam is produced by an *ion source*, which is the first, and probably the most critical part of every particle accelerator.

1.1 Motivation for this work

The work presented in this dissertation focuses on the Linac4 H^- ion source, and in particular its *beam extraction system*. The H^- beam is extracted from a hydrogen plasma by a strong electric field, and then transported at low energy (45 keV) in order to be focused into the 3 MeV Radio Frequency Quadrupole (RFQ) accelerator. In this low energy part of the accelerator the space charge effect on the beam is strongest, which leads to emittance growth and reduced beam brightness. In addition, since we extract negative ions, electrons present in the plasma will also be extracted. These *co-extracted electrons* are traditionally removed from the ion beam by a magnetic dipole field and guided into an *electron dump* (usually an electrode or a cup) as illustrated in Figure 1.1. The magnetic dipole only slightly affects the much heavier H^- ions.

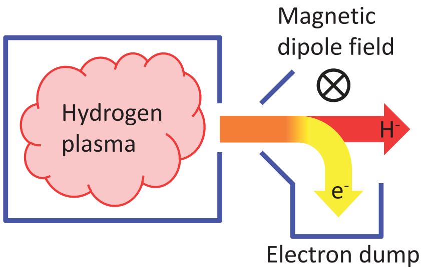

Figure 1.1: Sketch of a negative hydrogen ion source illustrating the ion beam extraction and the dumping of electrons by a magnetic dipole field.

The co-extracted electrons do, however, complicate the ion beam extraction. Their contribution to the beam space charge leads to additional emittance growth, and they should therefore be removed from the beam as early as possible. Furthermore, the extracted beam current from a plasma is inversely proportional to the square root of the mass. This relation means that the electron current is about 40 times higher than the H^- current for the same particle density in the plasma. The increase of total extracted current makes it more difficult for the power converters to keep a constant voltage, which then affects the beam energy during the pulse. Moreover, the magnetic dipole field causes asymmetry to the H^- beam, which leads beam losses.

In addition, as observed during the first H^- beam test at 45 keV, the electron beam might damage the electron dump. The high power density of the electron beam impacting on the electron dump can sublimate the dump material and release charge carriers into the extraction area. This evaporation of the electron dump triggers frequent high voltage breakdowns that stop the beam and reduce the ion source *reliability*. The reliability is an important requirement of the ion source. Whereas less beam current or poor beam quality can be accepted to a certain extent, any interruption of the source stops all fixed-target experiments, and also the filling of the LHC. Linac2 performed with a remarkable uptime of 98.4 % over a period of 10 years with just 0.2 % downtime attributed to the ion source. To achieve a similar performance for Linac4, which is required, it is mandatory that the ion source reliability exceeds 99 %.

The motivation for this work is to improve the ion beam extraction system of the Linac4 H^- ion source leading to an ion source that meets the Linac4 requirements with a reliable and stable operation. One of the most challenging requirements to meet is the H^- beam current, which directly depends on the production performance of the plasma generator. However, if the extraction system is not able to transport and handle this high beam current correctly, improvements of the plasma generator may not improve the beam current to the same extent. The beam current must also be transported within the required emittance, if not, the consequence will be beam losses further down the accelerator.

Existing H^- ion sources with similar requirements as Linac4 have solved the problem of beam extraction and dumping of the co-extracted electrons in different ways. The Penning source at the Rutherford Appleton Laboratory (RAL) extracts the ion beam into a 90° magnetic box, where the electrons are dumped on the sidewalls [3]. At the Spallation Neutron Source (SNS) in Oak Ridge National Laboratory, the electrons are dumped on a puller electrode at low voltage [4], and the Japan Proton Accelerator Research Complex (J-PARC) uses a similar system [5]. The negative ion source for the world's largest experimental tokamak nuclear fusion reactor, ITER, has incorporated magnets in the multi-aperture plasma grid, which deflect the electrons directly back to the grid [6]. Brookhaven National Laboratory's (BNL) magnetron uses the magnetic field of the plasma generator and dumps the electrons on the puller electrode (described in Section 5.2.3). The solution for the Linac4 ion source extraction system is a different method that incorporates the electron dump in a magnetized Einzel lens. The extraction system uses, in addition, a tuneable puller voltage that adapts the extraction field to the ion plasma density for optimum beam optics. The extraction system is described in detail in Section 5.3.

1.2 Scope of work

The work presented in this thesis consists of the study of ion beam extraction from a plasma, which leads to the design of a new extraction system. The design is based on simulations with IBSimu, which is a general-purpose three-dimensional simulation code for charged particle optics with space charge [1]. The extraction system design, production and implementation have been made in close collaboration with the design office at CERN. In this way it is possible to make all components fit in the small available space while respecting the mechanic and electromagnetic constraints.

The scope of the work consists of the following points:

1. Study of the ion beam extraction from a plasma.
2. Design of a new H^- ion beam extraction system.
3. Keep under control the power density of co-extracted electrons impacting on the electron dump.
4. Minimize the emittance growth in the extraction system.
5. Keep the beam size within the boundaries of the Low Energy Beam Transport (LEBT).
6. Demonstrate the validity of the beam extraction modelling by experiments.

The commissioning of the new extraction system, and the validation of the beam extraction modelling have been performed at a dedicated test stand for the Linac4 ion source. Figure 1.2 shows an overview of this test stand.

1.3 Outline

Chapter 2 gives an introduction to the high energy physics at CERN, and describes CERN's accelerator complex. The need for increased luminosity in the LHC requires the upgrade of the injector chain, starting with the construction of Linac4.

Chapter 3 presents an overview of existing ion sources, starting with a description of the requirements given by the particle accelerator. In Chapter 4 we will review the fundamental working principles of ion sources with a focus on negative ion production.

Chapters 5 and 6 constitute the main part of the results of the work for this dissertation. First we will describe the development of the Linac4 ion source, with the evolution of the plasma generators, and the design of the extraction system. The work

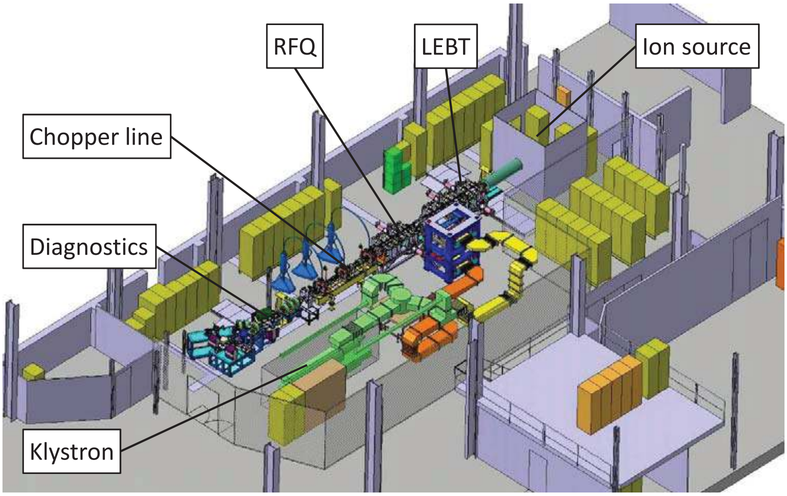

Figure 1.2: Overview of the ion source and RFQ test stand.

is then concluded by a characterization of the extraction system with a comparison of measurements and simulations. This part verifies and leads to a benchmarking of the simulations that led to the extraction system design. It also provides understanding of the processes happening during ion beam extraction, which are important for further improvements.

Appendix A provides a list of abbreviations, symbols, and constants frequently referred to in this dissertation. Appendix B shows a semi-empirical function for calculating the work function of a material covered by an alkali metal. Finally, a collection of publications from this work is given in Appendix C.

Chapter 2

Particle physics at CERN and motivation for Linac4

Particle physics is the branch of physics that deals with the properties, relationships, and interactions of subatomic particles. It is sometimes referred to as high energy physics since most elementary particles do not occur naturally at a precise time and location; instead they are created by collisions at high energy of other particles such as protons or electrons in particle accelerators, and observed in particle detectors.

2.1 CERN is a high energy physics research laboratory

CERN is the European Organization for Nuclear Research, an international scientific collaboration located on the Franco-Swiss border near Geneva. The organization operates the world's largest particle accelerator: the LHC, where particle beams are accelerated close to the speed of light and brought to collision in four different locations along the 27 km circumference.

The idea of a European collaboration first came up in 1949, at a time when European science was recovering after the Second World War. Inspired by other international organizations, a European atomic physics laboratory was proposed to unite scientists and to share the costs of nuclear physics facilities. At first a provisional council was established; *le Conseil Européen pour la Recherche Nucléaire*. Even though the organization later changed its name, the acronym remained. Geneva was selected as the CERN site in 1952, and the construction started in 1954.

The CERN convention was signed in 1953 by its 12 founding states[1], and the number of members has increased to 21 in 2014[2]. Membership was originally restricted to European countries; however in 2010, the organization was opened for applications from all nations, given that the convention did not explicitly exclude membership of non-European states. In addition to the member states come collaborations with more than 50 non-member states, and over 600 institutes and universities.

2.1.1 The accelerator complex contains four synchrotrons

CERN's accelerator complex, as shown schematically in Figure 2.1, consists of several machines that accelerate particles to increasingly higher energies [7]. The latest and highest energy accelerator is the LHC, where particle bunches of either protons or lead nuclei are accelerated up to the nominal beam energy of 7 TeV for protons and 2.76 TeV/u for lead ions ($^{208}\mathrm{Pb}^{82+}$). Presently, LHC has operated at approximately half the nominal beam energy (4 TeV for protons).

The proton physics program is the principal one and runs for about 10 months per year. The proton beam originates in Linac2, a 50 MeV linear accelerator that injects the beam into the Proton Synchrotron Booster (PSB). From PSB, the beam is sent to the Proton Synchrotron (PS) at 1.4 GeV, and then to the Super Proton Synchrotron (SPS) with an energy of 26 GeV. SPS gives the final acceleration step for LHC injection at 450 GeV. In the LHC, the beam is split into two beam pipes allowing the transmission of the beam in two different directions and the collision of the particle bunches in four experiments: ATLAS [8], CMS [9], ALICE [10] and LHCb [11]. For each bunch collision event, only about 20 out of more than one billion proton actually collide, so after the interaction points, the particle bunches continue their flight to collide with different bunches in the other experiments. LHC runs with collisions for about 10 hours before the beam is dumped, and the accelerator is prepared for a new injection from SPS.

The lead beam starts in Linac3 and is accumulated and accelerated in the Low Energy Ion Ring (LEIR) before injection into the PS. The beam then follows the same chain of accelerators as the proton beam. Lead collisions in the LHC, run for about one month per year.

---

[1] Belgium, Denmark, France, the Federal Republic of Germany, Greece, Italy, the Netherlands, Norway, Sweden, Switzerland, the United Kingdom and Yugoslavia

[2] Additional member states: Austria, Bulgaria, the Czech Republic, Finland, Hungary, Israel, Poland, Portugal, the Slovak Republic, and Spain. Yugoslavia left CERN in 1961.

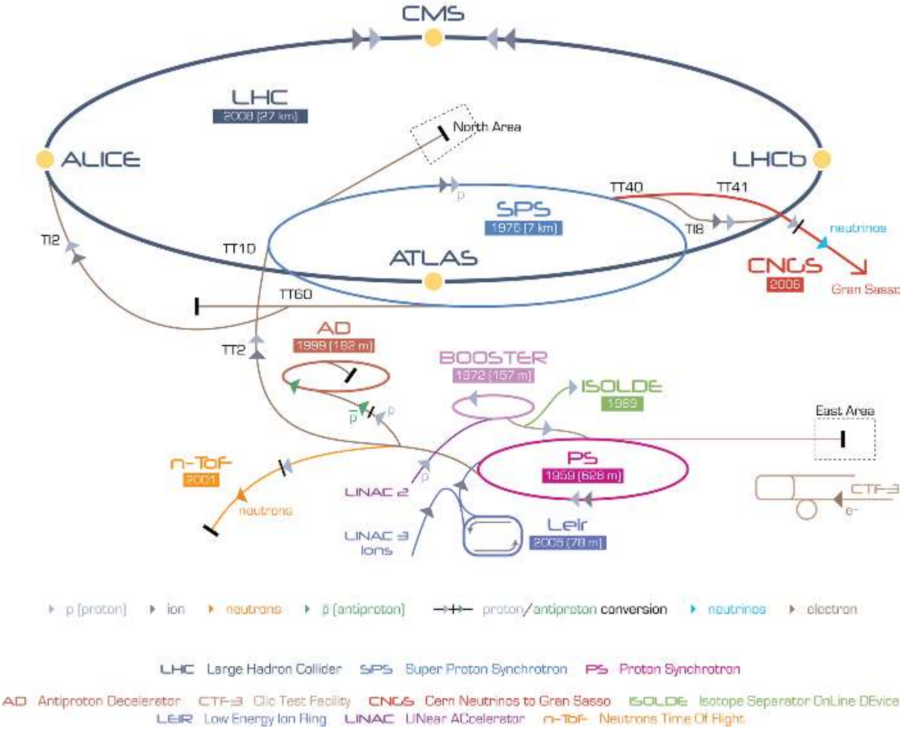

Figure 2.1: Overview of the CERN accelerator complex.

2.1.2 Other accelerators and experiments depend on the proton beam

Besides the LHC physics program, CERN also includes other accelerators and experiments, some of which depend on a reliable proton beam. In the following paragraphs, the accelerators and experiments shown in Figure 2.1 are briefly described.

ISOLDE

The Isotope Separator On Line DEvice (ISOLDE) is a facility for the production and studies of radioactive nuclei [12]. The facility produces radioactive nuclei by spallation, fission, or fragmentation reactions in thick targets that are irradiated with the proton beam from the PS Booster. The radioactive atoms are ionized, accelerated, separated according to mass, and delivered to experiments.

AD

The Antiproton Decelerator (AD) provides a 100 MeV antiproton beam for the study of antimatter [13]. The physics goals are the production and spectroscopy of antihydrogen to study fundamental symmetries, and to study interactions of antiprotons with atoms and nuclei. The decelerator uses the proton beam from the PS and fires it into a thin rod (about 3 mm diameter) of a heavy metal such as iridium or tungsten, which then produces a 3.5 GeV antiproton beam. About 10^{13} protons are needed for the production of 5×10^7 antiprotons. During the deceleration, the transverse temperature of the beam is lowered by stochastic and electron cooling.

n-TOF

The neutron Time-Of-Flight facility (nTOF) is a spallation neutron source that studies neutron-nucleus interactions for neutron energies ranging from a few meV to several GeV [14]. This facility takes the proton beam from the PS and shoots it on a lead target for the production of up to 600 neutrons per incoming proton. The separation distance of the target to the experiment allows the distinction of different neutron energies by their time-of-flight.

CNGS

The CERN Neutrinos to Gran Sasso (CNGS) project aims to study a phenomenon called neutrino "oscillations" [15]. Similar studies have shown that neutrinos can oscillate between two types of neutrinos given a long enough time-of-flight. To achieve a sufficient time-of-flight, CNGS sends a neutrino beam 732 km, through the Earth's crust, to Gran Sasso in Italy, where the neutrinos are detected. The neutrino beam is created by shooting the SPS proton beam into a series of small graphite cylinders, which produces a beam consisting of pions and kaons that decays to neutrino and muon pairs. The last beam was sent in 2013, and will not be restarted.

CTF3

The CLIC Test Facility (CTF3) is a project independent of the CERN accelerator facilities, studying the development of an electron-positron linear collider, the Compact Linear Collider (CLIC) [16]. This new linear collider would complement the experiments at LHC in the TeV energy range. The reason for a straight accelerator is because of the synchrotron radiation emission that is inversely proportional to the fourth power of the mass, making the energy loss per turn for an electron/positron beam too high for ring colliders. CLIC is designed to be 48.4 km long with an acceleration gradient of 100 MV/m.

2.1.3 Some of the greatest scientific achievements in modern times have been made at CERN

During more than 50 years, several important achievements in particle physics have been made at CERN. They include the following [17]:

1965 First discovery of an *antinuclei*: antideuteron, consisting of an antiproton and an antineutron.

1983 Discovery of the *W and Z bosons*, carriers of the weak nuclear force, by proton-antiproton collisions in the SPS. Carlo Rubbia and Simon van der Meer received the Nobel Prize in Physics the following year for their decisive contribution to the work leading to this discovery.

1995 First *antiatoms* produced: antihydrogen (antiproton with a positron).

2011 Trapping of antihydrogen for more than 1000 seconds, long enough to start detailed studies of *antimatter*.

2012 Announcement of the discovery of a new boson with a mass around 126 GeV: *the Higgs particle*, carrier of the Higgs field that gives mass to elementary particles through interactions with them. Peter Higgs and François Englert were awarded the 2013 Nobel Prize in Physics for their theoretical work that predicted the existence of this particle.

2.2 LHC needs higher luminosity for future discoveries

When trying to make new discoveries in particle colliders such as discovering the Higgs boson, we need a large number of collisions to distinguish the discovery from the background data. This is because these new particles are not directly observed in the particle detector, but very rapidly decay into other particles such as photons, quarks and leptons. These end products, predicted by the Standard Model, are common in particle collisions and they will be produced orders of magnitudes more often than the new particle or signs of new physics we are looking for. For this reason, it is necessary to repeat the production process a large number of times to find an excess from this background data.

The figure of merit for the collision rate in particle colliders is the *luminosity*, a measure of numbers of particles per cross section and time. The instantaneous luminosity, $\mathcal{L}$, is expressed as

$$\mathcal{L} = f\frac{N_1 N_2}{4\pi\sigma_x\sigma_y}, \tag{2.1}$$

where f is the bunch collision frequency, N_1 and N_2 are the number of particles for the two bunches, and σ_x and σ_y characterize the transverse beam profiles in the horizontal and vertical directions. Here we assume that the transverse profile of the two bunches are identical and Gaussian shaped, independent of the position along the bunch, and remain unchanged during the passage.

The number of production events, N_{prod}, then equals the cross section of interest, σ_{col}, times the time integral of the luminosity, $\mathcal{L}$:

$$N_{prod} = \sigma_{col} \times \int \mathcal{L}(t)dt. \tag{2.2}$$

LHC's luminosity at the end of 2012 was $1.0 \times 10^{34}\mathrm{cm}^{-2}\mathrm{s}^{-1}$. With a proton-proton cross section for inelastic collisions of $6 \times 10^{-26}\mathrm{cm}^{-2}$ at LHC energy, the number of collisions per second is roughly 600 million or 19 per crossing.

2.2.1 The first luminosity bottleneck originates in the Proton Synchrotron Booster (PSB)

The luminosity value of the LHC is presently not only limited by the LHC itself, but the injector chain delivering the beam also affects it. To identify potential bottlenecks, we start by rewriting and expanding Equation 2.1 to better represent the LHC case, assuming equal horizontal and vertical beam size, and knowing that $\sigma = \sqrt{\varepsilon\beta}$ (described in Section 3.1.3):

$$\mathcal{L} = \left(f_{rev} n_b \frac{\gamma F}{4\pi\beta^*} \right) \left(\frac{N_b^2}{\varepsilon_N} \right), \tag{2.3}$$

where f now is represented as the product of the revolution frequency, f_{rev}, and the number of bunches in the beam, n_b. F is a geometrical reduction factor from the crossing angles in the detectors, β^* the beta value at the interaction point, N_b the number of particles in each bunch, and ε_N the normalized emittance. The Lorentz factor, γ, is appearing from the normalized emittance: $\varepsilon_N = \varepsilon\beta\gamma$, where β in this case is the relativistic factor v/c, which for LHC energies is equal to 1.

The second term in this formula shows that the LHC luminosity directly depends on the characteristics of the injected beam. More precisely, it depends on the beam *brightness*, which is representing the number of particles that can be delivered within the transverse beam emittance. This value is limited by space charge effects in synchrotrons, especially at low energies, meaning that the effect is highest for the beam injection into the first circular machines of the accelerator chain.

The space charge from the beam acting on itself affects an important synchrotron parameter called the *tune*, Q. The tune represents the number of *betatron oscillations* per turn. If the tune equals an integer or a low order fraction of integers, machine errors excite beam resonances, causing high beam losses. When accelerating the beam, one has to find a favourable working point to avoid these resonances in both transverse planes, or in a combination of the two. The tune is, however, affected by the Coulomb forces between the charged particles. These forces create a self-field, which defocuses the beam [18]. The effect is a reduction of the tune by the so-called *incoherent space charge tune shift* ΔQ.

$$\Delta Q \propto \frac{N_b}{\varepsilon_N \beta \gamma^2}, \tag{2.4}$$

where β and γ are the relativistic factors.

In the case of a coasting (unbunched) beam, one could increase the synchrotron tune by the tune shift, and the space charge would no longer be an issue. However, for a bunched beam the space charge is not uniform across the bunch length: instead there is a tune spread. In order not to have parts of the beam in the lower order resonance regions, it is therefore vital to keep the tune spread low. As seen from Equation 2.4, ΔQ scales with $1/\gamma^2$, meaning that the effect is largest at injection and reduces at higher energies. Figure 2.2 shows the tune diagram for the PSB where the horizontal and vertical tune is represented at injection, after 120 ms acceleration, and at ejection (400 ms). The tune spread (neck-tie shaped area) is largest at injection, and causes a brightness limit of the PSB, which later affects the LHC luminosity.

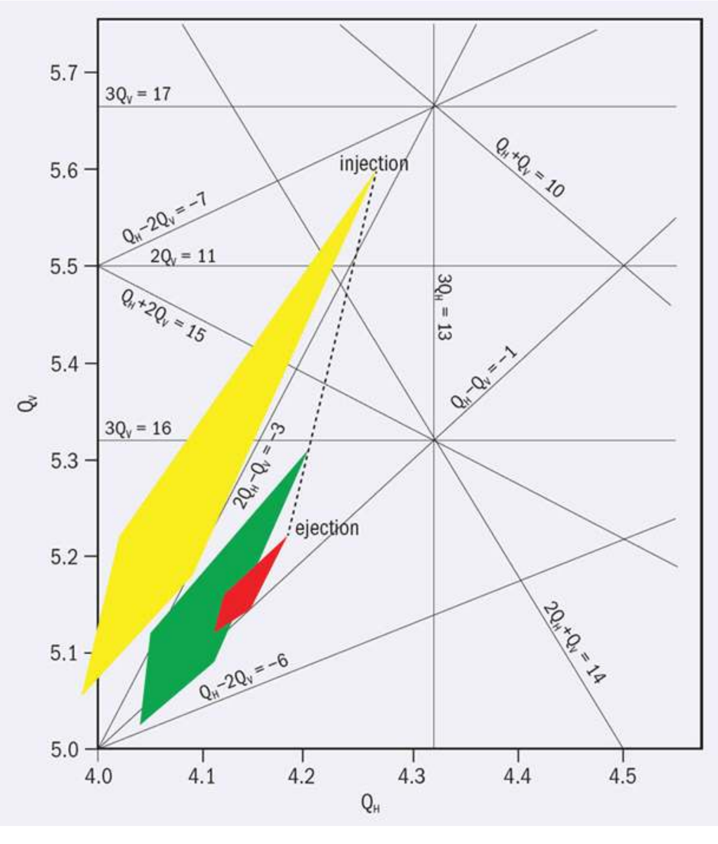

Figure 2.2: Horizontal and vertical tunes Q_H and Q_V, and the space charge tune spread ΔQ during acceleration in the PSB [19]. The yellow area is for the injection at 50 MeV, green after 120 ms acceleration, and red at ejection (400 ms, 1.4 GeV).

2.2.2 Linac4 is a linear accelerator designed to overcome the brightness limit in the PSB

From Equation 2.4, we see that doubling the brightness and keeping the present tune shift is possible if the relativistic factor $\beta\gamma^2$ is increased by a factor 2 at injection. The doubling of $\beta\gamma^2$ corresponds to an increase in energy from 50 MeV to 160 MeV [20].

Post-acceleration of the Linac2 beam before PSB injection is not a feasible option because of several reasons. First of all, being close to 30 years old, finding spare parts for maintenance will become more and more difficult in the future. Important vacuum leaks on the large accelerating tanks have been progressively appearing, and are a constant concern for future operation. In addition, the technology of linear accelerators has advanced, now using H^- acceleration and injection instead of protons. In a circular machine, it is impossible to inject a proton beam in the same phase-space (position-angle) as the circulating proton beam itself. The result is an increased emittance of the circulating beam, leading to reduced (or at least not increased) beam brightness. In addition, beam losses can reach up to 50 % from protons hitting the septum magnet[3]. The high beam loss together with higher proton energy would then cause concern for the radiation level at the PSB injection. The principle of charge exchange injection of H^- in a ring through a stripping foil is shown in Figure 2.3. This method has the advantage that one can accumulate protons over many turns without increasing the emittance (except by foil scattering). The peak current in the linear accelerator can then be reduced, thus saving cost of the accelerating structure. The beam losses are also dramatically reduced as the stripping foil has an efficiency close to 99 %.

The solution for upgrading CERN's accelerator structure and increasing the LHC luminosity is to replace Linac2 with a new linear accelerator for H^- ions; Linac4. Linac4 (Figure 2.4) is a normal conducting linear accelerator composed of an H^- ion source, an RFQ, Alvarez Drift Tube Linacs (DTL), Cell-Coupled Drift Tube Linacs (CCDTL), and Pi-mode structures (PIMS). The overall linac length is 76 m with an additional 70 m long transfer line that links to the present PSB injection line, as shown in Figure 2.5. Table 2.1 summarizes today's nominal LHC luminosity together with the parameters for a high luminosity LHC (HL-LHC) after the upgrades of the accelerator complex and the implementation of Linac4 [21].

---

[3] A septum is a magnet with a high magnetic field gradient, which allows a beam to circulate in a low B-field, but can be moved in to the high B-field region of the septum for extraction (or the opposite for injection)

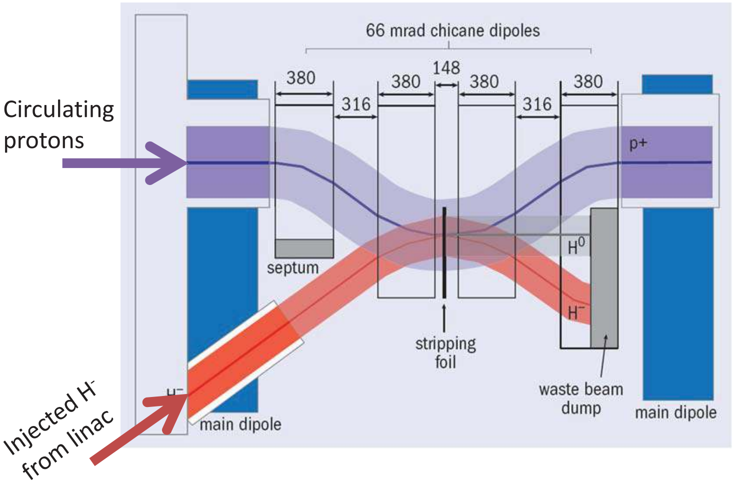

Figure 2.3: Schematic of H$^-$ injection into a circular machine. Figure adapted from [19].

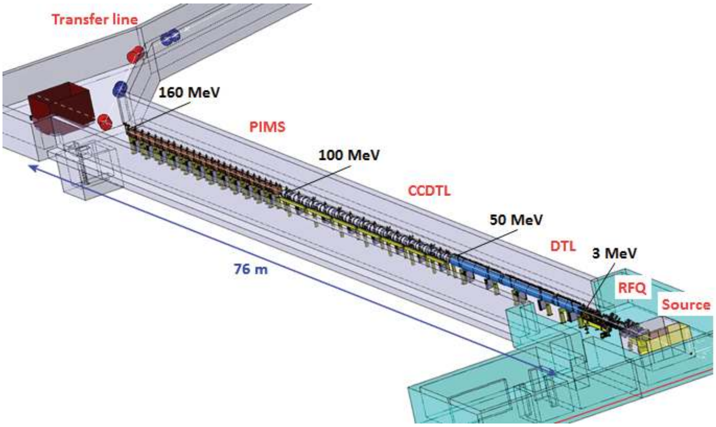

Figure 2.4: Linac4 tunnel layout. The accelerator consists of an H$^-$ ion source, Radio Frequency Quadrupole (RFQ), Alvarez Drift Tube Linac (DTL), Cell-Coupled Drift Tube Linac (CCDTL), and Pi-mode structure (PIMS).

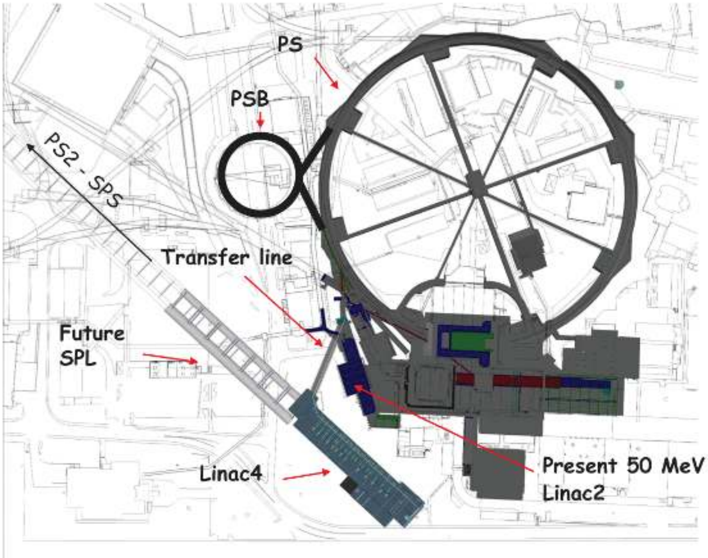

Figure 2.5: Linac4 will be linked to the PSB with a transfer line to the present injection line. The straight continuation from Linac4 was intended for upgrading to a higher energy superconducting linac, Super Proton Linac (SPL), for direct injection into PS2 (a new proton synchrotron). This project is for the moment stopped, thus leaving Linac4 in its current location.

Table 2.1: LHC parameters for today's nominal operation, and for the high luminosity (HL) upgrade of the accelerator complex with 25 ns and 50 ns bunch spacing [21].

	Linac2	Linac4	
Parameter	Nominal	HL 25 ns	HL 50 ns
f_{rev} [s^{-1}]	11 245	11 245	11 245
n_b	2 808	2 808	1 404
γ (p^+, 7 TeV)	7 460	7 460	7 460
F	0.83	0.37	0.37
β^* [m]	0.55	0.15	0.15
N_b	1.15×10^{11}	2.0×10^{11}	3.3×10^{11}
ε_N [µm]	3.75	2.5	3.0
$\mathcal{L}$ [$\mathrm{cm}^{-2}\mathrm{s}^{-1}$]	1.0×10^{34}	7.4×10^{34}	8.4×10^{34}
Events/crossing	19	141	257

Chapter 3

High intensity ion sources for particle accelerators

Particle accelerators accelerate and focus beams of *ions*. An ion is an atom (or a molecule) with a charge, which means that one or more electrons have been added or removed, as shown in Figure 3.1. Because of their electric charge, ions obey the Lorentz force, $\mathbf{F}$ [1]:

$$\mathbf{F} = q(\mathbf{E} + \mathbf{v} \times \mathbf{B}), \tag{3.1}$$

where q is the ion charge, $\mathbf{E}$ an electric field, $\mathbf{v}$ the ion velocity, and $\mathbf{B}$ a magnetic field. We can accelerate and steer ions in the same direction as an applied electric field. However, since the force originating from the magnetic field is always perpendicular to the ion velocity and the field itself, magnetic fields can never be used to accelerate ions, only to change their trajectories.

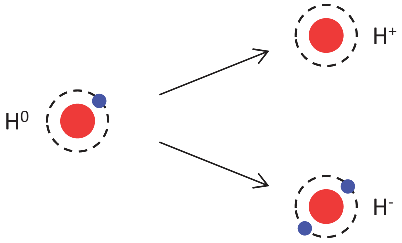

Figure 3.1: A neutral hydrogen atom can be ionized by either losing the electron and become H^+ (proton), or adding a second electron and become H^-.

---

[1] We use the convention to specify vectors with bold characters.

Beams of ions are created in the *ion source*. An ion source typically consists of a *plasma generator* that produces the desired ions, and an *extraction system* to accelerate and focus these ions (Figure 3.2). There exist numerous different ways of producing ion beams, and just as many different types of ion sources. Before we look into some types of ion sources, it helps to take a step back and get an overview of the requirements that are given by the accelerator.

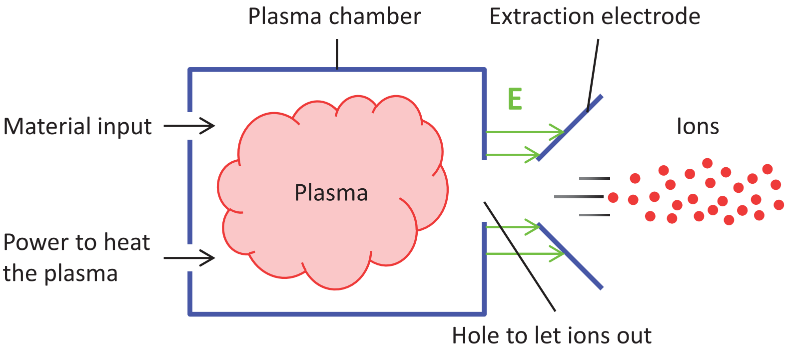

Figure 3.2: Basic scheme of a plasma ion source. The ion source basically consists of a plasma chamber into which one feeds the material to ionize, and power for the ionization process. The desired ions are extracted through a hole with an electric field.

3.1 Requirements of particle accelerators

Different particle accelerators have differing requirements. Whereas a medical accelerator for cancer treatment by hadron therapy typically needs a precisely focused low intensity beam of light ions with a well defined energy, ion sources for fusion use high current beams for injecting hydrogen and deuterium atoms into the fusion chamber. The LHC at CERN uses both protons and lead ions for studying fundamental physics, and there are also future plans for using other ions such as argon.

This section starts by defining some basic ion source parameters, and then continues to characterize the different types of ion sources.

3.1.1 Particle type and charge state

The first and most obvious parameter is the *particle type*. It can be either an atom (H, C, Au) or a molecule (H_3, CO). Together with the particle type comes its *charge state*. Both positive and negative charges are used (H^+, H^-), and the charge state number may also vary (Pb^{25+}, Pb^{27+}). Symbolically, the particle type can be represented by:

$$^{A}E_{n}^{q\pm}, \tag{3.2}$$

where E represents the element, A is the mass number indicating different isotopes of the element, $q\pm$ is the charge state, which can be either positive up to the fully stripped nucleus, or negative with the addition of an electron, and n is added for ionized molecules.

3.1.2 Energy

The charged particle's kinetic energy is gained by the electric potential energy, which depends on the particle's charge, q, and the difference in electrostatic potential, V:

$$E_k = qV, \tag{3.3}$$

where q is the product of the particle's charge state, $q\pm$, and the elementary charge, e.

The energy unit commonly used in particle physics is electron volts (eV), equal to the energy when accelerating a singly charged ion with one volt. Instead of using the standard energy unit of Joules (J), electron volts makes energy calculations for specific extraction voltages easier. For example, a $^{208}Pb^{25+}$ ion accelerated over 20 kV gains an energy of 500 keV, which equals 8.0×10^{19} J.

Radio frequency particle accelerators often require a fixed velocity at their input. It is therefore common to express the beam energy as the energy per nucleon, E_u, which only depends on the ion velocity, v:

$$E_u = \frac{E_k}{A} = \frac{qV}{A} = \frac{1}{2}m_u v^2, \tag{3.4}$$

where A is the mass number of the ion, m_u is the rest nuclear mass unit (1.67×10^{-27} kg). For the previous $^{208}Pb^{25+}$ ion, E_k = 500 keV, whereas E_u = 2.4 keV/u.

Using high energy beams has several advantages such as reduced space charge that leads to higher beam currents, lower energy spread ratio ($\Delta E/E$), reduced geometrical emittance that gives a smaller beam, and easier injection into an RF accelerator such as a DTL. On the other hand, a high energy beam is technically more difficult to achieve, it has a higher risk of high voltage sparking, and it requires a longer acceleration length. In addition, higher energy leads to higher power, which has consequences for beam intercepting devices.

3.1.3 Intensity, emittance and brightness

The beam *intensity* is defined in terms of the beam current, I_{beam}, which in principle is the same as an electric current.

$$I_{beam} = \frac{qN}{t}, \tag{3.5}$$

where N is the number of ions and t the time. In multiple charge state sources, the beam intensity is sometimes given as the particle current, I_{part}. This parameter makes it easier to compare the intensity of sources with different charge state ions.

$$I_{part} = \frac{eN}{t} = \frac{I_{beam}}{q\pm}. \tag{3.6}$$

For a pulsed ion source, it is usual to give the peak current, together with the time structure of the beam (Section 3.1.4).

To express the density of particles in the ion beam, it is not sufficient to only quote the beam size. A beam can be focused down to a very small beam size; however, most of this beam would be lost afterwards because of the individual particles' large angles. The term beam *emittance* is therefore introduced, which includes the positions and angles of all the particles in the beam, as shown in Figure 3.3 (a). The total geometrical emittance, ε, is defined as the beam area (A) in the position-angle phase space divided by π:

$$\varepsilon = \frac{\mathrm{A}}{\pi}. \tag{3.7}$$

When a single particle is orbiting in the periodic structure of a circular accelerator, the motion of the particle can be described by the so-called *Hill differential equation* [22]. The solution to this equation shows that, at a fixed position along the accelerator, the particle makes the shape of an ellipse in phase space when making multiple turns. It is therefore common to represent the total emittance as the area of this ellipse (divided by π). This definition is also used for linear accelerators. The emittance ellipse is described by the *Twiss parameters*: α, β, and γ.

$$\alpha = -\frac{\langle xx' \rangle}{\varepsilon},\ \beta = \frac{\langle x^2 \rangle}{\varepsilon},\ \text{and}\ \gamma = \frac{\langle x'^2 \rangle}{\varepsilon}. \tag{3.8}$$

Figure 3.3 (b) shows the emittance ellipse with the most important characteristic values.

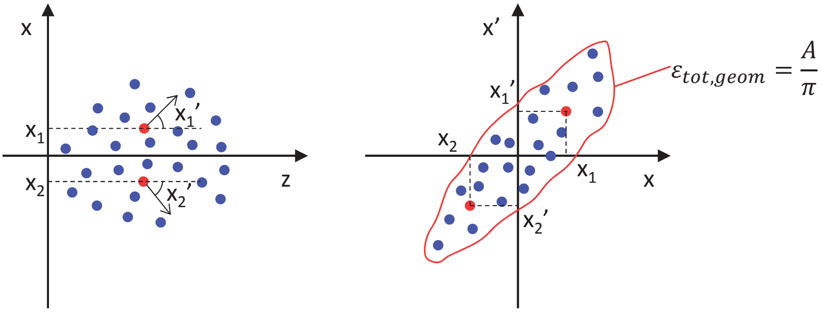

(a) Particles travelling along the z-axis with different positions x, and angles x'. The particle distribution in the plane x-x' is called the phase-space, within where the emittance is defined as the area covered by the beam divided by π. This figure represents a diverging beam.

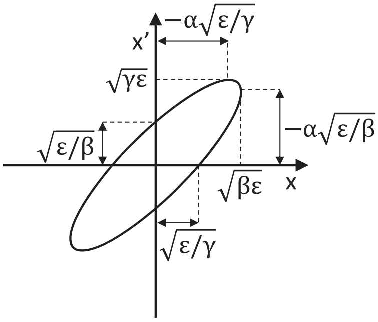

(b) Emittance ellipse with the most important characteristic values.

Figure 3.3: Illustrations of ion beam emittance.

As an ion beam gains higher energy, the angle of the particles, being the transversal divided by the longitudinal velocity, reduces. We therefore introduce a new term called the *normalized emittance*, ε_N, which is conserved with acceleration. ε_N, is obtained by multiplying the geometrical emittance with the relativistic factors β and γ (not to be confused with the Twiss parameters):

$$\varepsilon_N = \beta\gamma\varepsilon. \tag{3.9}$$

The above given definition of beam emittance represents the total geometrical emittance.

It is, however, more common to use the root mean square (rms) emittance, which is a statistical definition of the amount of phase space covered by the beam. In the case of beam centred in both position and angle, the rms emittance is defined by

$$\varepsilon_{rms} = \sqrt{\langle x^2\rangle\langle x'^2\rangle - \langle xx'\rangle^2}, \tag{3.10}$$

with

$$\langle x^2\rangle = \frac{\Sigma x^2 I(x,x')}{\Sigma I(x,x')},\ \langle x'^2\rangle = \frac{\Sigma x'^2 I(x,x')}{\Sigma I(x,x')},\ \text{and}\ \langle xx'\rangle = \frac{\Sigma xx' I(x,x')}{\Sigma I(x,x')}, \tag{3.11}$$

where $I(x,x')$ is the beam current passing through the phase-space at (x,x').

The ion plasma temperature, and the size of a circular aperture where the beam is extracted from define a minimum emittance of an ion beam [23]. The emittance of an ion beam with a Maxwellian ion temperature distribution can be calculated by

$$\varepsilon_{N,rms} = \frac{1}{2}\sqrt{\frac{kT}{m}}\frac{r}{c}, \tag{3.12}$$

where T is the plasma ion temperature, and r is the aperture radius.

The ion beam *brightness* is merely the beam current, I, normalized over the emittance in the two transversal planes, ε_x and ε_y:

$$B = \frac{I_{beam}}{\varepsilon_x \varepsilon_y}. \tag{3.13}$$

Low and high brightness beams are illustrated in Figure 3.4. For a circular plasma aperture the beam emittance is proportional to the aperture radius, and the beam current is approximately proportional to the area of the aperture. Changing the size of the aperture does therefore not influence the beam brightness.

The unit of the emittance unit can be expressed in different ways. π mm mrad is often used, however neither π nor radians (meters/meter) are units. This topic has been discussed in [24], and following the paper's suggestion, the emittance is expressed as µm throughout this dissertation.

3.1.4 Time structure

Ion sources can operate either pulsed or in continuous mode. The *pulse length*, t_{pulse}, and the *repetition rate*, $1/t_{rep}$, are two important parameters for pulsed ion sources. The

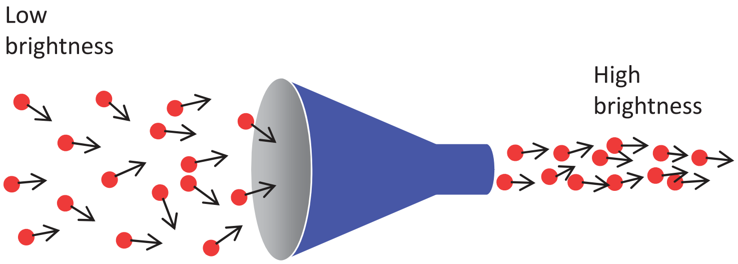

Figure 3.4: The ion beam brightness relates the beam current and emittance. A high brightness beam carries a high beam current (high number of charged particles) within a small emittance (small beam size and angular distribution).

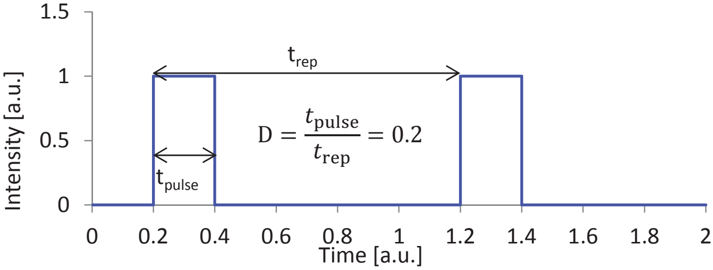

Figure 3.5: The duty factor is the product of the pulse length and the repetition rate.

duty factor, D, is simply defined as the product of the pulse length and the repetition rate:

$$D = \frac{t_{pulse}}{t_{rep}}. \tag{3.14}$$

With a high duty factor, the ion source plasma is on more permanently, and it can reduce the ion source lifetime by sputtering off some of the material in the plasma chamber. On the other hand, with a low duty factor, external heating might be needed to reach the optimum operational temperature. Figure 3.5 illustrates the time structure of a pulsed ion beam.

3.1.5 Material efficiency and beam purity

The material efficiency, $\eta = N_{ions}/N_{atoms}$, defines the fraction of atoms of the material that are converted to ions. This parameter can be of interest if the raw material is expensive, limited, dangerous, or polluting.

Some applications may require high beam purity such as medical accelerators. The beam purity, $\kappa = N_{ions}/N_{beam}$, is the fraction of the desired ion compared with the total number of ions in the beam. Some ion sources can minimize beam contamination, for example with selective ionization. The purity can also be improved by electro- and magnetostatic spectrometers or radio-frequency acceleration. Another way is by using stripper foils to produce charge states out of reach for the contaminants. For example: suppression of ^{17}O from ^{17}F by stripping to $^{17}O^{8+}$ and $^{17}F^{7+}$, or breaking up contaminant molecules such as H_2^+ background on D^+.

3.1.6 Reliability and stability

Depending on the accelerator, the ion source *reliability* can be more or less important. In the case of the LHC or for a spallation neutron source, beam downtime is frustrating and costly. Cancelling the hadron therapy treatment of a cancer patient, however, is much worse. Ion source faults can be classified in the following way:

Intermittent fault The beam performance changes drastically, but returns without intervention. Downtime: Seconds.

Protection fault A sub-system switches off because of an interlock or a protection circuit. Downtime: Minutes.

Fault outside vacuum A sub-system breaks outside the vacuum, and does not affect the vacuum or thermal stability. Downtime: Minutes to hours.

Fault inside vacuum A sub-system breaks inside the vacuum, or the heating system fails. Downtime: Hours.

Figure 3.6 illustrates the typical downtimes associated with these four classes. The reliability can be characterized by uptime or availability, mean time between failures (MTBF), or mean time to repair (MTTR).

The ion source is a sensitive piece of equipment, and may cause accelerator downtime. Some precautions should be taken such as: (1) improve the electromagnetic configuration to avoid high voltage breakdowns across insulators, (2) use uninterruptible power supplies to reduce sensitivity due to power cuts, (3) keep installations clean, (4)

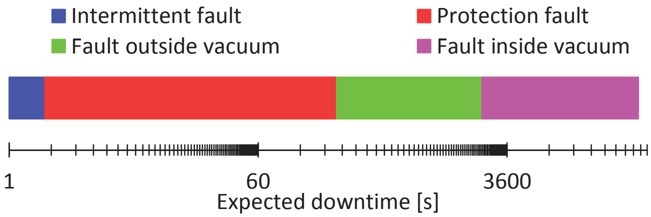

Figure 3.6: Four classes of ion source faults and their respective downtimes.

have maintained and tested spare parts ready in case of failures, (5) have a cold spare source fully built, tested and ready for installation, and (6) have a hot spare source ready to be implemented with a switch yard.

The *stability* of the ion source is characterized by variations in the beam performance, and may cause problems for the accelerator or experiments. Improvement of the stability can be made by for example adding feedback loops on critical parameters, over-specifying the ion source and not running at maximum performance, and monitoring and storing ion source parameters in databases to analyse causes of instabilities or breakdowns.

3.2 Types of ion sources

3.2.1 Electron bombardment

When an electron strikes an atom, ion or molecule, there is a chance that one or more electrons are removed from the target particle, which increases its charge state and becomes ionized. A simple way of achieving this is to accelerate thermionic emitted electrons to sufficient energy to cause ionization of the atoms in a chamber. This type of ion source is called an *electron bombardment ionization* ion source. It is a cheap and simple ion source, but the beam currents are too low for high power accelerators.

3.2.2 Plasma discharge

As the density of charged particles increases, a plasma is formed, which influences the electric and magnetic fields in the source. This principle is used in an improved version of the electron ionization ion source, called the *plasmatron*. In this type, a conical shaped cathode funnels down the electrons towards a higher density region near the anode extraction aperture as shown in Figure 3.7(a). The higher density means that more electrons will cause ionization in this region leading to a plasma discharge. The high ion density in the plasma near the extraction aperture leads to higher beam currents. An improved version of the plasmatron is the *duoplasmatron*; in which the plasma density is further increased by placing the source inside a solenoid, and making the conical electrode of magnetic steel (Figure 3.7(b)). The magnetic field lines are now squeezed towards the anode, and together with the funnelling effect of the cone, a very high plasma density is achieved in front of the extraction aperture. The plasma is actually too dense for a beam extraction with uniform distribution and low emittance, and the plasma is therefore allowed to expand in a so-called expansion cup before the extraction. This type of ion source is commonly used because of its high beam currents, and is implemented as the proton source for Linac2 at CERN.

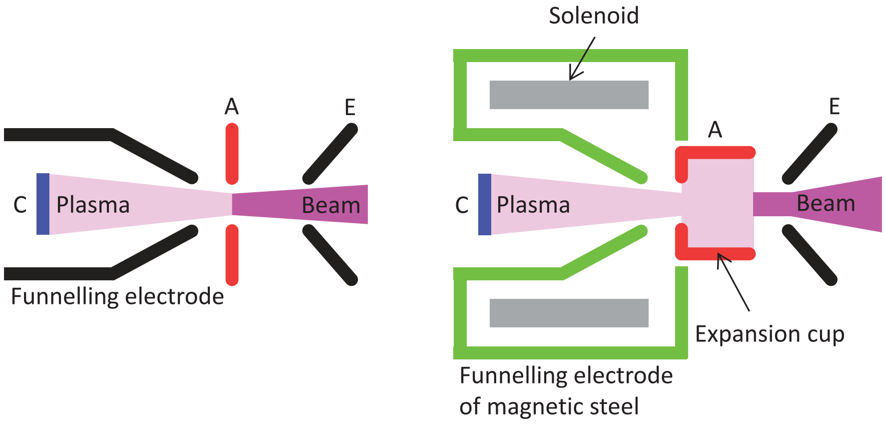

(a) Plasmatron (b) Duoplasmatron

Figure 3.7: Diagram of a plasmatron and a duoplasmatron ion source. C: Cathode, A: Anode, E: Extraction electrode.

Magnetron and *Penning* sources are other types that use discharge driven electron ionization. In principle they both consist of a shaped anode with magnetic field lines running along its axis as shown in Figure 3.8. The magnetron has a cathode in the centre, whereas the Penning has two cathodes at either end of the anode. The combination of electric and magnetic fields increases the distance travelled by the electrons, which leads to a sustained gas discharge and high ion and electron densities. A common problem with these ion sources is that the ions in the plasma are accelerated towards the cathode, sputtering off the cathode material. This limits the lifetime, and might change the performance of the ion source during operation. The problem can be addressed by using other methods to heat the plasma's electrons and favour ionization such as radio frequency (RF) or microwaves.

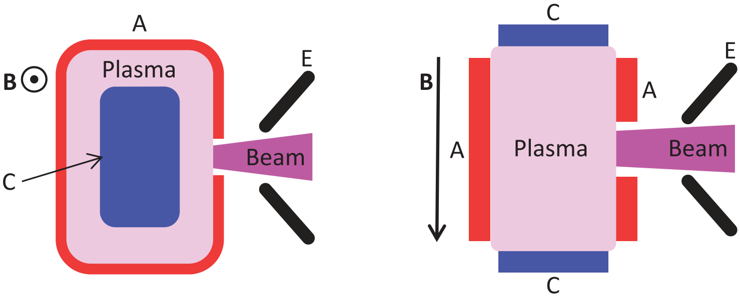

(a) Magnetron (b) Penning

Figure 3.8: Diagram of a magnetron and a Penning ion source. C: Cathode, A: Anode, E: Extraction electrode, **B**: Magnetic field.

3.2.3 Plasma heating with time varying electric fields

RF driven ion sources use a time varying electric field for creating a plasma discharge and heating instead of a cathode-anode electron acceleration. The coupling to the plasma can either be capacitive by using two electrodes, or inductive by using a coil. In *microwave ion sources*, electric fields in GHz frequency regime generate the plasma. The microwave energy is coupled via a waveguide to the plasma discharge, which is located in a chamber with similar dimensions as the wavelengths and is surrounded by solenoids that produce an axial magnetic field. The static magnetic field makes the electrons gyrate with the cyclotron frequency

$$f = \frac{1}{2\pi}\frac{eB}{m_e}, \tag{3.15}$$

where e is the elementary charge, B the magnetic field strength, and m_e the electron mass. If the microwave matches the cyclotron frequency, there is a resonant condition that allows the electrons to absorb the microwave energy. Ion sources that operate with this condition are called *Electron Cyclotron Resonance (ECR)* ion sources. They can produce a large variety of ions, and have the capability of achieving high charge-states. The heavy ion source at CERN, Linac3, uses an ECR ion source for the production of $^{208}\mathrm{Pb}^{27+}$ ions.

3.2.4 Electron beam ionization

Electron beam ion sources (EBIS) are capable of producing very high charge states of positive ions, even completely stripped heavy elements. In order to ionize the particles, this ion source type uses a high current, high-density electron beam, which is compressed by a strong magnetic field generated by a solenoid. The positive ions are then trapped transversally by the negative potential well of the electron beam, and longitudinally by static electric fields. The REX-ISOLDE facility at CERN uses this type of source as a charge breeder of radioactive ions [25].

3.2.5 Surface evaporation

Laser ionization ion sources use a powerful laser to vaporize particles from a target, which is made out of the material to ionize. During the evaporation process, a plasma is generated, and the electrons of the plasma are heated by the laser radiation. The ions are produced by electron impact ionization of the ablated atoms from the surface. When the particles are removed from the surface, the target has to be moved to expose a fresh area for the next laser beam pulse. Laser ion sources can be used to produce a large range of ions by changing the target material. However, they can only produce short beam pulses at a low repetition rate, and with a high energy spread.

Vacuum arc ion sources produce a metal-plasma that jets away form the surface similar to laser ion sources. However, this type of ion source vaporizes the cathode target material by a high power arc. These sources can produce high currents of metal ions, but the beam can be quite noisy as the arc spots on the cathode are moving around. The cathode lifetime is limited to about one day depending on the duty cycle.

3.2.6 Surface ionization

Surface ionization ion sources are efficient sources for producing positive ions from neutral atoms with low ionization energy such as alkali metals. If a layer of atoms coats a heated surface of a material with a high work function, the outer layer electrons of the atoms can populate energy levels of the material. If these atoms are desorbed from the surface (by heating or bombardment), a fraction will be liberated in an ionized state.

The ratio of atoms desorbed as ions can be calculated by the Saha-Langmuir equation [26, 27, 28]:

$$\frac{N_i}{N_0 + N_i} = \left[1 + \frac{g_0}{g_i} \exp\left(\frac{E_i - W}{kT}\right)\right]^{-1} \tag{3.16}$$

with N_i and N_0 the number of positive ions and atoms evaporated form the surface, g_i and g_0 statistical weights for the ions and atoms (for alkali metals, $g_0/g_i = 2$), E_i the ionization energy of the atom, and W the work function of the surface. The ratio is highest for a surface with a high work function (W) and/or atoms with a low ionization energy (E_i).

Figure 3.9 shows the ratio of desorbed ions from a tungsten surface (W = 4.54 eV) for two temperatures. The circles indicate the ratio for different alkali metals, which are suited for surface ionization because of their low ionization energies.

If the chamber material is made out of low work function material instead, this method can be used to create negative ions from atoms with a high electron affinity.

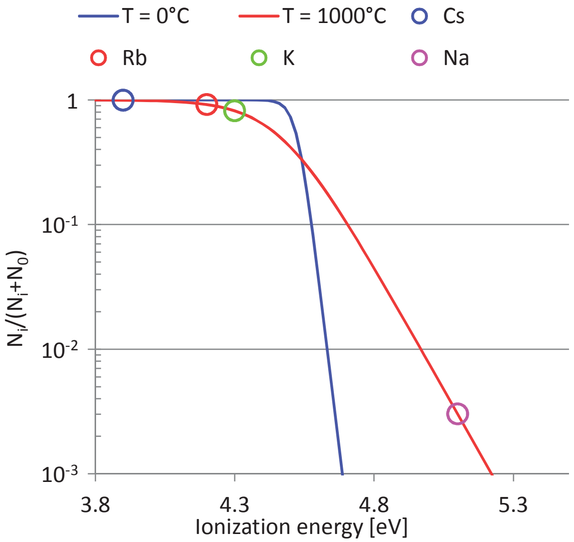

Figure 3.9: Fraction of atoms emitted as positive ions from a tungsten surface for two different temperatures. The circles indicate the ratios for four alkali metals.

3.3 Negative ion sources

When creating a plasma, we produce a quasi-neutral mixture of charged particles, mostly consisting of positive ions and electrons. The cross section for atom ionization by electron bombardment is high for electron energies of more than approximately 3 times the atom ionization energy. However, to create negative ions, we have to attach an electron instead: a process with typically a lower cross section.

The binding energy of the additional electron is called the electron affinity. Stable negative ions are possible for elements with a positive electron affinity, meaning that once the electron is bound to the atom, energy is required to release it. Halogens and hydrogen atoms are good candidates to become negatively charged, whereas elements such as the noble gases with negative electron affinities are not able to form stable negative ions.

A common problem for negative ions is that the electron affinities are quite small. For the case of hydrogen, the value is 0.75 eV compared with the electron binding energy for neutral hydrogen of 13.6 eV. This means that the extra electron is very loosely bound, and the ions are likely to be destroyed. Negative hydrogen (H^-) is the most commonly produced negative ion, and is used as an example in the following descriptions of production methods. Other types of negative ions can also be produced in similar ways, such as D^-, O^-, B^-, and C^-.

3.3.1 Applications using negative ions

Negative ions are more challenging to produce than positive ions. The beam extraction is, in addition, more complicated because of the electrons that are co-extracted with the beam. Nevertheless, because of the opposite charge of the ions, there are benefits for the following accelerator. Negative ions are oppositely affected by electric and magnetic fields, and they are easily stripped to neutrals or positive ions. Here are presented five applications where it is interesting to use negative ions:

Tandem accelerator

Tandem sources accelerate negative ions to a stripping foil at high voltage and the resulting positive ions back to ground potential on the other side of the foil. The ions gain twice the energy of the applied terminal voltage as illustrated in Figure 3.10.

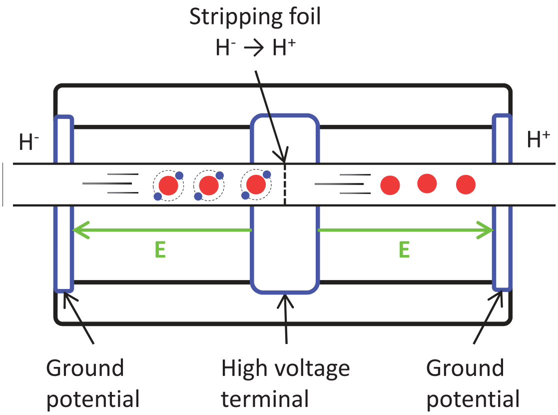

Figure 3.10: Illustration of a tandem accelerator.

Cyclotron

In cyclotrons, the ion beam is accelerated by an oscillating electric field through a static magnetic field. The result is a beam that spirals outwards as the energy increases making the bending radius from the magnetic field larger (Figure 3.11). By using negative ions, one can change the charge of the ions by sending them through a stripping foil. The positive ions extract themselves by curving the opposite direction through the magnetic field, having a specific energy defined by the radius of curvature of the negative ions before stripping.

Charge exchange injection

Charge exchange injection into synchrotrons allows overlapping the incoming negative ion beam with the circulating positive ion beam (Figure 3.12). After injection, the negative ions are stripped to positive, as described in Section 2.2.2 for the Linac4 injection into the PSB.

Tokamak plasma heating

The plasma in a magnetic confined system for hot plasmas can be heated using neutral beams (Figure 3.13).

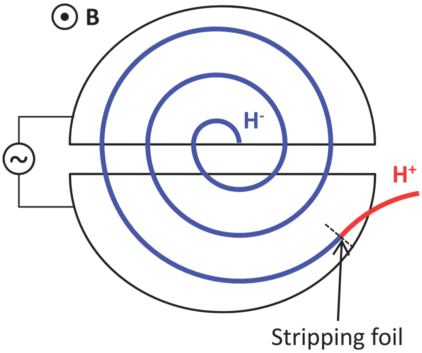

Figure 3.11: Illustration of a cyclotron.

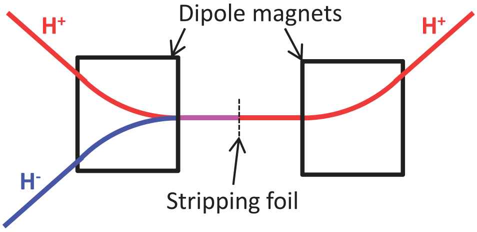

Figure 3.12: Illustration of the charge exchange injection.

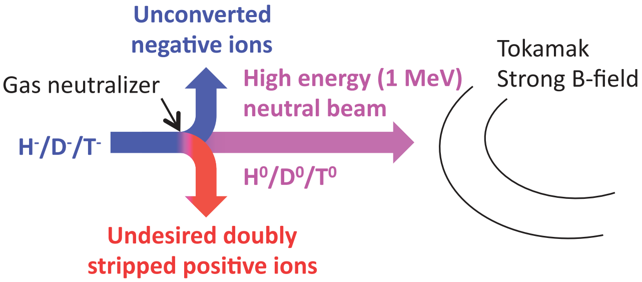

Figure 3.13: Illustration of neutral beam injection for fusion reactors.

Space propulsion

Ion sources for space propulsion traditionally use a positive ion beam for providing thrust of the spacecraft. When the positive ions leave, the spacecraft charges up negatively, and an electron beam needs to be ejected at the same time to neutralize the charge. This can be avoided by using an alternating extraction of positive and negative ions form an ion-ion plasma, as shown in Figure 3.14.

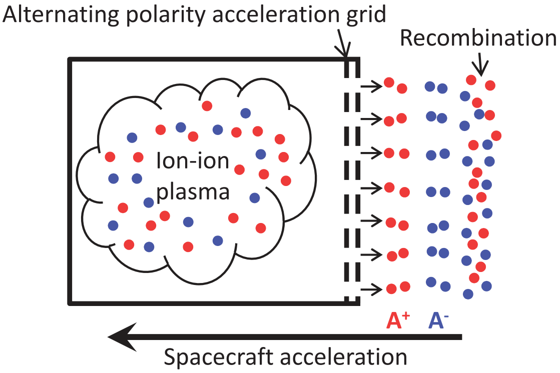

Figure 3.14: Illustration of an ion source for space propulsion.

3.3.2 Methods of producing negative ions

There are generally three methods of producing beams of negative ions: (1) *charge exchange*, (2) *volume production*, and (3) *surface production*.

Charge exchange

Charge exchange ion sources transfer electrons directly to a positive ion beam with an energy in the order of 10 keV. The beam is sent through a target (foil or gas), and the negative ions are produced by sequential electron capture: first the positive ion is neutralized, and then converted to a negative ion. Alkali-metal vapours are efficient to use as electron donors because of their low ionization energies. The charge exchange efficiency can reach about 10 % [29].

An interesting application of this ion source type is the production of polarized ion beams [30]. Lasers are used to achieve electronic spin alignment in the alkali vapour, and this spin alignment is preserved during the charge exchange by the presence of a strong magnetic field. The beam then consists of electron spin polarized neutrals.

Volume production

In volume production, the formation of negative ions happens in the volume of the plasma. There are many ways for an electron to be attached to a neutral hydrogen atom in a plasma such as direct attachment of a free electron, or charge exchange between two neutrals leading to one H^- and one proton. However, most of these interactions have smaller cross sections than the destruction cross sections of H^-, and are therefore not efficient.

One process that does have a higher production than destruction cross section, is the dissociative attachment of vibrational and rotational excited hydrogen molecules, $H_2(\nu, J)$, where ν and J denote the vibrational and rotational quantum numbers, respectively [31]. The most important of these excitations is the vibrational, ν, that has more than one order of magnitude higher cross section for dissociative attachment than for a rotational excitation, J, with approximately the same internal energy [32].

A large contribution for creating vibrational excited states comes during hydrogen desorption from surface walls. In the case of gas hydrogen excitation, levels up to $\nu = 9$ have been observed [33]. Another important production mechanism happens in the volume by collisions with high energy electrons (E > 10 eV) [34]. These collisions lead to electronic excitation of the hydrogen molecules, which then decay to vibrational states:

$$H_2(\nu = 0) + e_{fast} \rightarrow H_2^*(\nu') + e_{slow} \tag{3.17}$$

$$H_2^*(\nu') \rightarrow H_2(\nu'') \tag{3.18}$$

The dissociative attachment by electron collision has the highest cross section for low energy electrons ($E \sim 1$ eV).

$$H_2(\nu'') + e_{slow} \rightarrow H_2^- \rightarrow H^- + H^0 \tag{3.19}$$

The cross sections for these two processes leading to the production of H^- ions are shown in Figure 3.15.

Surface production

Surface ionization was introduced in Section 3.2.6. There it was described how a surface of a high work function material can capture an electron from an atom sticking to the

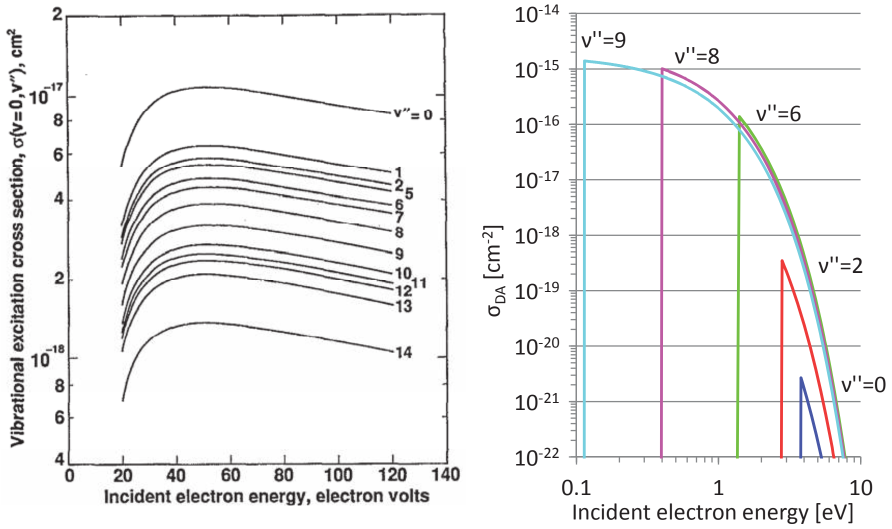

(a) $H_2(\nu=0)+e \rightarrow H_2(\nu'')+e$. Vibrational excitation cross sections for ground state hydrogen molecules via electron collision [34].

(b) $H_2(\nu'')+e \rightarrow H^- + H^0$. Dissociative electron attachment cross sections for excited hydrogen molecules as a function of the electron energy. [35].

Figure 3.15: Cross sections leading to volume production of H^- ions.

surface, which then can desorb as an ion. If the work function of the surface is small, it is possible that the atom desorbs with an additional electron instead. The Saha-Langmuir equation describing the fraction of negative ion desorbed is given by:

$$\frac{N_i}{N_0+N_i} = \left[1+\frac{g_0}{g_i}\exp\left(\frac{W-E_a}{kT}\right)\right]^{-1} \tag{3.20}$$

with N_i and N_0 the number of negative ions or atoms evaporated form the surface, g_i and g_0 statistical weights for ions and atoms, W the work function of the surface, and E_a the electron affinity of the atom. This relation is lowest for surface with a low work function, W, and/or atoms with a high electron affinity, E_a.

Figure 3.16 shows the ratio of negative ions emitted from two materials with different work function, both heated to 1000°C. For H^- production ($E_a(H^0)$ = 0.75 eV), the ratio is very sensitive to the work function. For example, by reducing W from 2.14 eV to 1.5 eV, the negative ion production rate increases by two orders of magnitude.

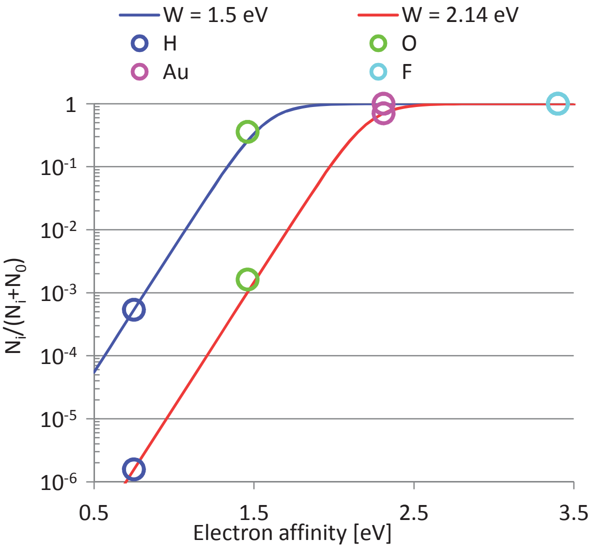

Figure 3.16: Fraction of atoms emitted as negative ions from a surface with a low work function material. Two different work functions are represented, and the circles indicate the ratios for four different elements.

The formation of negative hydrogen ions by scattering protons from a metal surface has been described with two models: a probability model [36], and an amplitude model [37]. The probability model gives the following probability for negative ion formation:

$$\beta^- \propto \frac{v_\perp}{W - E_a - \Delta E_a}, \tag{3.21}$$

where $v_\perp$ is the ejected atom velocity normal to the surface, and ΔE_a the level shift of the electron affinity. The amplitude model provides the following probability for negative ion formation:

$$\beta^- \propto e^{\frac{E_a - W}{v_\perp}}. \tag{3.22}$$

Similar for both these models and the Saha-Langmuir equation, is that they all show the importance of having a low work function material for maximum negative ion yield.

Caesium is the element with the lowest work function, $W = 2.14$ eV. However, even lower work functions can be achieved by covering a metal surface with a thin (less than a monolayer) layer of an alkali metal such as caesium. The most likely theory is that in this thin layer, the alkali atoms are arranged in a different manner than in the bulk [38]. The maximum reduction of the material work function has been described by a semi-empirical formula, which is detailed in Appendix B. The work function of a molybdenum surface as a function of the fractional coverage of caesium is shown in Figure 3.17. Because of the weak bonding between caesium atoms compared with the bonding to the material surface, no further caesium adhere to the surface at room temperature when a monolayer is reached. If the surface is cooled too much, multiple layers can form, and the work function would then reach the one for bulk caesium. It is normal that the surfaces operate in the presence of hydrogen, oxygen or carbon, in which case the work function could be substantially different [38].

Caesium has the disadvantage that it may cause problems for the accelerator such as instabilities (differences in caesium layer), high voltage breakdowns (caesium accumulation), and safety hazards (caesium is chemically highly reactive). For obtaining low work function materials without caesium, one proposal is to use so-called negative electron affinity materials such as hydrogen-terminated boron nitride and diamond [39].

Negative ion destruction

The extra attached electron of the negative hydrogen ion is very weakly bound to the atom. The ions are therefore easily destroyed by interaction with other particles in the

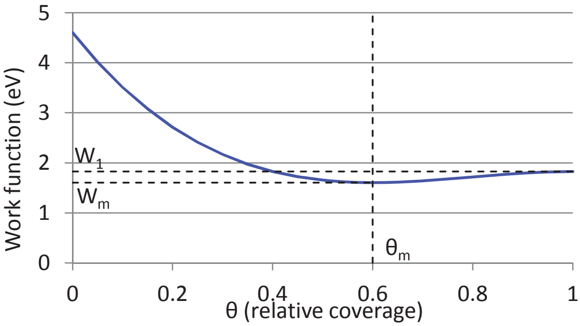

Figure 3.17: Work function of a molybdenum surface with a fractional coverage of caesium. As the coverage increases, the work function decreases to a minimum value, W_m, located around 60 % of a monolayer. Adding more caesium then increases the work function to an equilibrium value, W_1, which has a value between W_m and the work function of bulk caesium. The plot is made by using the semi-empirical polynomial fit described in Appendix B [40].

plasma. The destruction process is usually one of the following:

$$\text{Mutual neutralization:} \quad H^- + H^+ \rightarrow H^0 + H^0 \tag{3.23}$$

$$\text{Electron detachment:} \quad H^- + e \rightarrow H + 2e \tag{3.24}$$

$$\text{Associative detachment:} \quad H^- + H^0 \rightarrow H_2^* + e \tag{3.25}$$

The cross section for destruction by electron detachment is highly dependent of the electron energy as shown in Figure 3.18. The plot shows that the electron energy should be kept as low as possible (E∼1 eV) to avoid H$^-$ destruction by electron detachment. In H$^-$ volume sources, a magnetic filter is placed close to the extraction aperture to avoid high energy electrons to diffuse into this region (described in Section 4.1.4).

3.3.3 H$^-$ ion sources for particle accelerators

A variety of H$^-$ ion sources are in use at accelerator laboratories around the world. These include surface plasma sources with magnetron, Penning and surface converter geometries as well as magnetic-multipole volume sources with and without caesium. Reviews of operational ion sources can be found in references [41, 42].

J-PARC uses a LaB$_6$ filament driven caesium free source to produce a 38 mA H$^-$

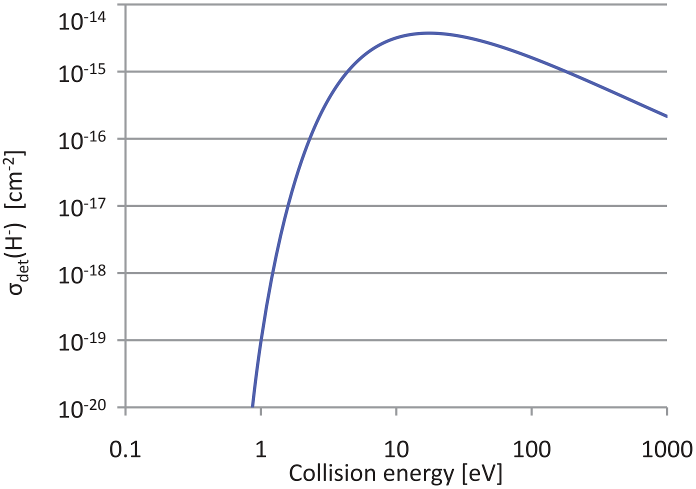

Figure 3.18: Cross section for electron detachment in e + H^- collisions. Figure adapted from [35].

beam with a duty factor of 0.9 % at 50 keV. The plasma is confined with a multicusp magnet arrangement, and the filter magnets are outside of the plasma saddled on the top and bottom cusp magnets. The insulated plasma electrode plate has a 9 mm diameter beam hole, and a thickness of 10 mm with an internal angle of 45°. The plate was run with a negative bias to the source body of 12.6 V to attract positive ions.

The SNS RF ion source is required to produce 40 mA of H^- at a 6 % duty factor, 1 ms pulses at 60 Hz. During ion extraction, the plasma of the SNS multicusp source is excited using 20–50 kW of 2 MHz RF. To speed the high-powered ignition, the plasma is sustained continually with 200 W of 13.56 MHz RF. The RF power is coupled into the plasma using an internal water-cooled copper-antenna that is coated with porcelain. The SNS source can run both with and without caesium. It is estimated that the surface production is directly responsible for 70 % of the beam current.

A Penning H^- source is being used at the RAL, ISIS spallation neutron source. The ISIS source operates at 50 Hz, 200 μs beam (1 % duty factor) while the discharge pulse width is 400–650 μs long (2 %–3.2 % duty factor). The operating current is 45 mA H^-. While operating at this duty factor, the source lifetime is up to 40–50 days. The beam is extracted from the plasma at 17 kV through a 10×0.6 mm^2 slit.

Table 3.3.3 summarizes the main operational parameters of a selection of H^- ion sources.

Table 3.1: List of H^- ion sources for particle accelerators with main operational parameters (values are from 2005). P_d = discharge power, fil. = filament, SPS = surface plasma source, SCS = surface converter source, DESY = German Electron Synchrotron, Hamburg, TRIUMF = Canada's national laboratory for particle and nuclear physics, Vancouver, INR = Institute for Nuclear Research, Moscow, Russia, BINP = Budker Institute of Nuclear Physics, Novosibirsk, Russia, LANSCE = Los Alamos Neutron Science Center, New Mexico, USA. Table adapted from [42].

Source type	Source location	I_{H^-} [mA]	Duty factor [%]	Rep. rate [Hz]	$\varepsilon_{N,rms}$ x/y [μm]	P_d [kW]	e/H^-	Life-time [months]
Multicusp volume, H_2								
RF	DESY	40	0.12	8	0.25	~20	26	>12
LaB_6 fil.	J-PARC	38	0.9	25		35		
Multicusp volume, $Cs+H_2$								
RF	SNS	33	6.0	60	0.22/0.18	~40		
W fil.	TRIUMF	20	100	dc	0.022	~5	4-5	
W fil.	J-PARC	72	5.0	50	0.13/0.15	~5	4-5	
SPS								
Magnetron	BNL	100	0.5	7.5	0.4	~2	0.5	~6
	Fermilab	60	0.1	15	0.2/0.3	~7		~6
	DESY	50	0.05	6	0.46/0.31	~5		~9
Penning	RAL	45	1.0	50	0.6/0.7	~4		~2
	INR	50	2.0	100	0.4/0.7	~10		~0.5
Hollow cath.	BINP	8	100	dc	0.2/0.3	0.4		~0.2
SCS								
W fil.	LANSCE	17	12.0	120	0.13	~6	2.5	~1
LaB_6 fil.	J-PARC	20	0.5	20	0.33	~4	4.5	3-4

Chapter 4

Fundamental working principles of ion sources

Ion sources generally consist of a plasma generator and an extraction system, as explained in Chapter 3. In order to understand the process of ion beam formation, some basic knowledge of plasma dynamics and ion beam extraction is required. This chapter describes the creation and transport of an ion beam from a plasma starting with basic plasma parameters, then the process of beam extraction, and finally the beam transport.

4.1 Basics of ion source plasmas

A plasma can be described as a *quasineutral* gas of charged and neutral particles which exhibits *collective behaviour* [43]. Since a plasma consists of charged particles, the forces acting between them are much stronger than for example in a neutral gas. The interactions between particles are no longer dominated by direct collisions, but rather by long range electromagnetic forces. This means that each plasma particle interacts with many other particles at the same time. The plasma is therefore able to show a collective response to an external stimulus, which is what we mean by collective behaviour. The term quasineutral means that the plasma is able to shield off external electric potentials. Quasineutrality is further described in Section 4.1.2.

4.1.1 Thermal properties

An idealized gas in thermal equilibrium has a distribution of particles speeds known as the Maxwell-Boltzmann distribution of molecular speeds:

$$f(v) = \left(\frac{m}{2\pi kT}\right)^{3/2} 4\pi v^2 \exp\left(-\frac{mv^2}{2kT}\right), \tag{4.1}$$

where m is the particle mass, k the Boltzmann constant, T the temperature, and v the particle speed. As the temperature increases, the distribution function broadens, and the maximum shifts towards higher molecular speeds as shown in Figure 4.1. It then becomes probable that some of the particles in the gas will be ionized through collisions. At very high temperatures, a large fraction of the particles will be ionized, and start to show plasma behaviour.

Thermalisation happens when there are sufficient collisions to distribute the energy. Neutral-neutral and electron-electron collisions have different character, but the result is the same. A Maxwell-Boltzmann distribution function can therefore also be considered for a plasma.

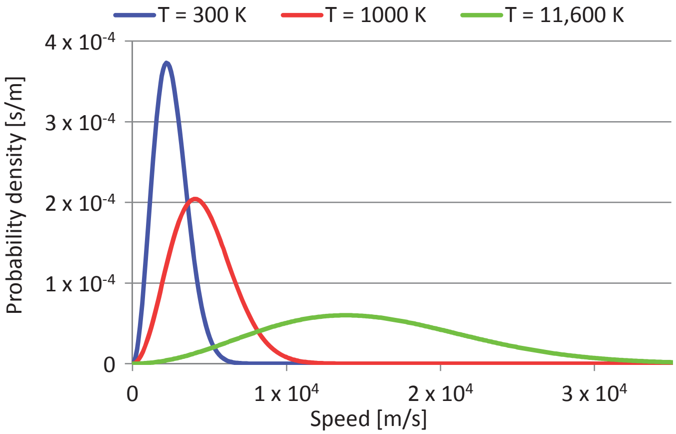

Figure 4.1: The Maxwell-Boltzmann speed distribution function for hydrogen atoms at different temperatures. As the temperature increases, the distribution function broadens, and the maximum shifts towards higher speeds.

The mean particle speed is given by

$$\langle v \rangle = \sqrt{\frac{8kT}{\pi m}}, \tag{4.2}$$

and the mean energy is

$$\langle E_k \rangle = \frac{3}{2}kT. \tag{4.3}$$

The energy corresponding to kT is normally used to denote the temperature. For a 1 eV plasma, we then have T $\approx$ 11,600 K.

A plasma can have several temperatures at the same time. Usually, ions and electrons can have different temperatures, T_i and T_e. This effect can occur if the collision rate between among ions or among electrons themselves is larger than rate of collisions between an ion and an electron. Each species can then be in its own thermal equilibrium, but the plasma might not last long enough for the temperatures to equalize. With the presence of a magnetic field, a single species can also have different temperatures. This is because the forces acting along **B** are different from those acting perpendicular to **B**. A Maxwell-Boltzmann distribution function is normally used to describe the temperature of each particle type, and for the different temperatures of a single species.

4.1.2 Plasma criteria

In order for an ionized gas to be considered as a plasma, it must fulfil the following three criteria: (1) the *Debye length* must be much smaller than the dimensions of the system, (2) the *plasma parameter* must be much larger than 1, and (3) the *plasma frequency* must be larger than the collision frequency with neutral atoms.

Debye length

A fundamental characteristic of a plasma is its ability to shield out electric potentials that are applied to it. If we insert a positive test charge into a plasma, electrons would immediately be attracted by this test charge and form a cloud around it. For a negative test charge, the cloud would be formed by positive ions. The shielding distance from the test charge to the bulk plasma is called the *Debye length*, λ_D, given by

$$\lambda_D = \sqrt{\frac{\varepsilon_0 kT}{e^2 n}}, \tag{4.4}$$

where ε_0 is the permittivity of free space, e the elementary charge, and n the plasma density. When the density increases, λ_D decreases as expected. With higher temperatures, the shielding distance increases as a result of the thermal agitations. λ_D is normally defined with the temperature being the one for electrons, because electrons are more mobile than ions and will generally do the shielding by moving towards or from the perturbation of electric potential.

A plasma is defined as *quasineutral* if the dimensions, L, of a system are much larger than λ_D. This is the first criterion for an ionized gas to be considered as a plasma.

Plasma parameter

In order for the Debye shielding to be a statistically valid concept, it requires a sufficient amount of particles to create the shielding cloud. The number of plasma particles is characterized by the dimensionless *plasma parameter*, N_D, defined as the number of charged particles in a so-called "Debye sphere" (a sphere with radius λ_D):

$$N_D = n\frac{4}{3}\pi\lambda_D^3. \tag{4.5}$$

The second plasma criterion is $N_D \gg 1$. When this condition is fulfilled, the collective interactions of the charged particles dominate over the binary interactions, and the plasma particles can be treated as if they interact with a smooth background. The Maxwell-Boltzmann distribution functions that describe the thermal properties of the plasma are then still valid.

Plasma frequency and collisions

If an electron in the plasma is displaced, an electric field will build up as to restore the neutrality of the plasma. The electron is then pulled back by this electric field. This restoring force has the characteristics of simple harmonic oscillation, leading to a resonant frequency know as the *plasma frequency*, ω_p. The plasma frequency for electrons is represented by

$$\omega_{pe} = \sqrt{\frac{e^2 n}{\varepsilon_0 m_e}}, \tag{4.6}$$

where m_e is the mass of the electrons. For ions, the relation becomes

$$\omega_{pi} = \sqrt{\frac{Z^2 e^2 n}{\varepsilon_0 m_i}}, \tag{4.7}$$

where Z and m_i are the charge state and mass of the ions, respectively.

The third plasma criterion has to do with collisions. In the case of a very weakly ionized gas, neutral atoms will dominate the charged particle collisions, and the charged particle motion is described by hydrodynamic forces rather than by electromagnetic forces. In order to be considered as a plasma, the plasma frequency must be larger than the *collision frequency* with neutral atoms:

$$\omega_p \tau > 1, \tag{4.8}$$

with τ representing the mean time between collisions with neutral atoms:

$$\tau = \frac{1}{n_n \sigma v}, \tag{4.9}$$

where n_n is the neutral density, σ the cross-sectional area of the neutrals, and v the charged particle velocity.

4.1.3 Plasma sheath and potential

In all practical plasma devices, the plasma boundary is the vacuum chamber wall. When ions and electrons hit the chamber wall, they recombine and are lost. The potential of the plasma is then modified. Since electrons have much higher thermal velocities than ions, they are lost faster and leave the plasma with a net positive charge with respect to the wall. This potential difference cannot be distributed over the entire plasma since the Debye shielding will confine it to a layer of the order of a few Debye lengths: this layer is called a *plasma sheath*.

The plasma/sheath transition takes place where $\Phi = 0$, and the potential in the sheath is described by Poisson's equation [43]:

$$\frac{d^2\Phi}{dx^2} = \frac{e(n_e - n_i)}{\varepsilon_0} = \frac{en_0}{\varepsilon_0}\left[\exp\left(\frac{e\Phi}{kT_e}\right) - \left(1 - \frac{2e\Phi}{m_i v_0^2}\right)^{-1/2}\right], \tag{4.10}$$

where n_e and n_i are the densities of electrons and ions, respectively, n_0 the density in the main plasma, and v_0 the initial velocity of the ions arriving to the sheath. Equation 4.10 is only valid when it satisfies the *Bohm sheath criterion*:

$$v_0 \geq v_B = \sqrt{\frac{kT_e}{m_i}}. \tag{4.11}$$

This relation gives a minimum velocity of ions arriving at the sheath, the Bohm velocity, v_B. In order for the ions to gain this velocity, there exists a *pre-sheath* in which the ions are accelerated to the required velocity by a potential drop of $\Delta\Phi \geq kT_e/2e$. The potential variation of the plasma close to the chamber wall is shown in Figure 4.2.

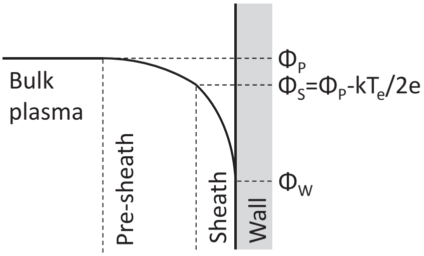

Figure 4.2: Plasma sheath at a wall boundary. Φ_P and Φ_W represent the plasma and wall potentials, respectively.

To estimate the plasma potential, we assume equal particle fluxes of ions and electrons at the border between the plasma sheath and the pre-sheath [44]. The Bohm velocity gives the ion flux in this region.

$$\Gamma_i = n_0 v_B, \tag{4.12}$$

and the electron flux by the average thermal electron speed modified by the Boltzmann relation according to the potential variation in the plasma sheath:

$$\Gamma_e = \frac{1}{4} n_0 \langle v_e \rangle \exp\left(-\frac{e(\Phi_S - \Phi_W)}{kT_e}\right). \tag{4.13}$$

By inserting the relations for the Bohm velocity (Equation 4.11) and the mean particle speed (Equation 4.2), we obtain

$$n_0 \sqrt{\frac{kT_e}{m_i}} = \frac{1}{4} n_0 \sqrt{\frac{8kT_e}{\pi m_e}} \exp\left(-\frac{e(\Phi_S - \Phi_W)}{kT_e}\right), \tag{4.14}$$

which simplifies to

$$\Phi_S - \Phi_W = \frac{kT_e}{2e} \ln\left(\frac{m_i}{2\pi m_e}\right), \tag{4.15}$$

and the plasma potential with respect to the wall becomes:

$$\Phi_P - \Phi_W = \frac{kT_e}{2e}\left[1 + \ln\left(\frac{m_i}{2\pi m_e}\right)\right]. \tag{4.16}$$

4.1.4 Magnetized plasmas

In ion sources, magnetic fields are often used for enhanced ion production. These B-fields can for example be used to confine the plasma, or to increase the probability of collisions leading to ionization. The magnetic field acts on the charged particles of the plasma by the Lorentz force. Following are a few examples of plasma magnetization.

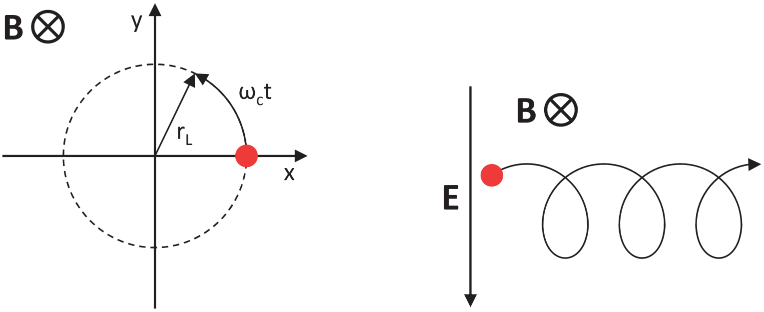

(a) Gyration.

(b) **E** × **B** drift.

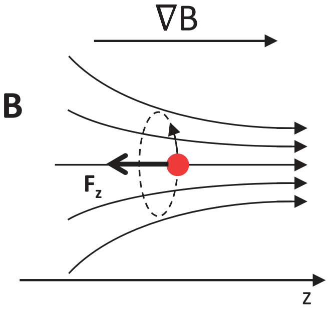

(c) Magnetic mirror.

Figure 4.3: Examples of single charged particle motion. Figures are adapted from [43, 45].

Gyration

In the presence of a uniform magnetic field, the Lorentz force is expressed as

$$\mathbf{F} = q(\mathbf{v} \times \mathbf{B}). \tag{4.17}$$

The motion created by the B-field is a gyration around the field line as shown in Figure 4.3 (a). The radius of circular orbit is called Lamor radius, r_L:

$$r_L = \frac{mv_\perp}{qB}, \tag{4.18}$$

where $v_\perp$ is the charged particle's velocity perpendicular to the magnetic field. The gyration frequency is expressed as

$$\omega_c = \frac{qB}{m}. \tag{4.19}$$

ECR ion sources use the electron gyration to effectively heat the plasma. By injecting a time varying electric field with the same frequency as the gyration frequency, the electrons in phase will continuously increase their energy as they spiral around the B-field line.

$\mathbf{E} \times \mathbf{B}$ drift

When a constant electric field is perpendicular to a magnetic field, the Lorentz force acts only in the plane perpendicular to **B**. The motion created by the magnetic field is the gyration that was described above. It can be calculated that the electric field does not contribute to a net acceleration of the particle, but displaces its gyration centre [43]. Since there is no net acceleration of the particle, the Lorentz force reduces to

$$\mathbf{E} = -\mathbf{v} \times \mathbf{B}. \tag{4.20}$$

By crossing each side with **B** we obtain:

$$\mathbf{E} \times \mathbf{B} = -\mathbf{v} \times \mathbf{B} \times \mathbf{B} = -\mathbf{B}\left(\mathbf{v} \cdot \mathbf{B}\right) + \mathbf{v}B^2, \tag{4.21}$$

and we can now express the velocity of the gyration centre:

$$\mathbf{v} = \frac{\mathbf{E} \times \mathbf{B}}{B^2}. \tag{4.22}$$

A perpendicular electric and magnetic field induce a drift that is perpendicular to both fields, and independent of the particles' charge and mass. The $\mathbf{E}\times\mathbf{B}$ drift is illustrated in Figure 4.3 (b).

Magnetron and Penning sources use the $\mathbf{E}\times\mathbf{B}$ drift to increase the path lengths of the electron trajectories to increase the probability of collision with an ion or neutral before reaching the anode. $\mathbf{E}\times\mathbf{B}$ drifts might also cause surprising high voltage breakdown when a magnetic field is present in a high electric field region.

Magnetic mirror

A magnetic field that varies in magnitude along the same direction as the field, gives rise to a force that acts on charged particles. If we consider the field to be in the z-direction, the force is expressed as

$$F_z = -\mu\frac{\partial}{\partial z}B_z, \tag{4.23}$$

where μ is the *magnetic moment* of the gyrating particle:

$$\mu = \frac{1}{2}mv_\perp^2/B. \tag{4.24}$$

This force acts in the opposite direction of the increasing B-field magnitude, irrespective of the direction of the field. The origin of this force is quite simple to understand. When the ion moves along the positive direction B-field line, it starts gyrating around this line, as shown in Figure 4.3 (c). However, when the B-field magnitude increases, the gyrating particle is affected by a B-field component pointing towards its gyration centre. The cross product of the particle's velocity and this field component results in a force directing towards the low field density region. If the direction of the field lines would be opposite, the particle would gyrate in the opposite direction, and the force would still point towards the low B-field density region. With a simple pair of coils, we can form two magnetic mirrors between which a plasma can be trapped (Figure 4.4 (a)).

The magnetic mirror is, however, not a perfect trap. A particle moving along the z-axis with no perpendicular velocity ($v_\perp$), will not be affected by the force and escape. By using the ratio of perpendicular to parallel velocity, we can determine which particles will be trapped in the mirror. First, we define the pitch angle, $\theta = \tan^{-1}(v_\perp/v_\parallel)$. The smallest allowed pitch angle for confined particles is given by

$$\theta = \sin^{-1}(\sqrt{B_0/B_m}), \tag{4.25}$$

where B_0 is the magnetic field in the centre of the magnetic bottle and B_m the maximum field of the mirror [43].

This type of particle losses is shown for a dodecapole multicusp magnetic confinement in Figure 4.4 (b). 12 magnets surround the plasma with magnetizations alternating between pointing inwards or outwards. The purple arrows represent the magnetic field vectors with sizes corresponding to the field magnitude. The orange traces inside are trajectories from electrons with a randomly chosen starting energy of 5 eV. We see that the electrons that encounter the transverse field lines (between the magnets), are immediately reflected back to the centre. The only electrons that are allowed to escape the magnetic mirror that has been formed are those with small enough pitch angle.

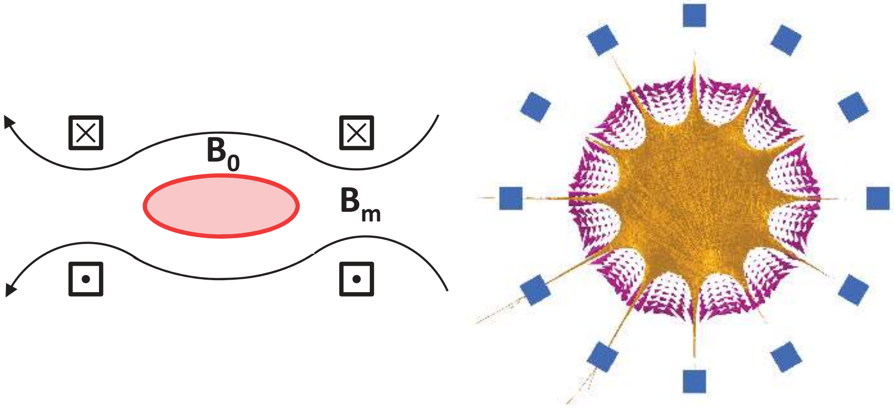

(a) A plasma trapped between magnetic mirrors. Figure adapted from [43].

(b) Magnetic multicusp confinement of charged particles. Simulated with Vector Fields Opera [46].

Figure 4.4: Two examples of magnetic confinement of a plasma.

Diffusion in magnetic field

A magnetic dipole field perpendicular to a charged particle's velocity will change the trajectory of the particle and reflect it back to where it came from. This was illustrated in Figure 4.4 (b). However, in a plasma there are also collective effects that can make particles diffuse across magnetic dipoles. The diffusion across a magnetic field is expressed

Table 4.1: Dependence of the electron temperature at the extraction aperture by introducing a magnetic filter field [47].

Parameter	No filter	Weak B-field	Strong B-field
Max B-field on axis [mT]	0	8.4	20.5
Electron temperature [eV]	4.5	2.5	0.5

as

$$D_{\perp} = \frac{kT\nu}{m\omega_c^2}, \tag{4.26}$$

where ν is the collision frequency of the particle, and ω_c the gyrating frequency around the B-field (Equation 4.19) [43].

The collision frequency, ν, is not actually an expression of how often particles collide, which is an event that rarely happens. Instead it is a measure of the effect of many small Coulomb interactions that eventually leads to a trajectory deviation of $\pi/2$. ν has a different expression for electron-electron, electron-ion, and ion-ion collisions. However all these interactions have the following relation in common:

$$\nu \propto m^{-1/2}(kT)^{-3/2}, \tag{4.27}$$

where m is the mass and T the temperature for the electron/ion. Including this in Equation 4.26 leads to

$$D_{\perp} \propto m^{1/2}(kT)^{-1/2}B^{-2}. \tag{4.28}$$

As we would expect, this relation shows that a stronger magnetic field will slow the diffusion of the charged particles. It also shows that the ions diffuse more easily than the electrons because of their larger mass. Finally we see that the magnetic field has a selectivity depending on the temperature: cold particles diffuse easier than hot particles. This effect is used in the so-called filter fields in volume production negative ion sources. The plasma can thus be separated into a hot and a cold region; these two regions are optimized for creating vibrational exited hydrogen molecules and creating H^- ions by dissociative electron attachment, respectively.

The effect of the filter field on the electron temperature has been confirmed by Langmuir probe measurements on the SPL plasma generator [47]. Two different B-field strengths were used, including a measurement without magnets. The electron temperature at the extraction aperture is summarized in Table 4.1.

4.2 Ion beam extraction from a plasma

Extraction of ions from a plasma and ion beam formation is achieved by an *extraction system*. A simple single stage extraction system consists of two electrodes as shown in Figure 4.5. The electric field is given by the voltage difference and the distance, d, between the two electrodes, where the puller normally is kept at ground potential together with the following accelerator parts. The emission surface of the ions at the plasma boundary is called the plasma *meniscus*.

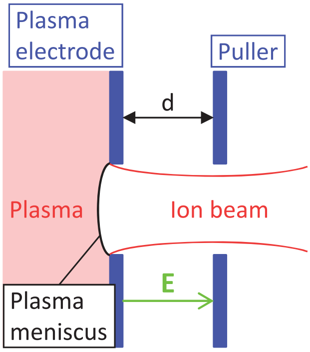

Figure 4.5: Simple single stage extraction system. The ion beam is extracted from the plasma held at a high voltage to the puller at ground potential.

4.2.1 Definition of plasma meniscus

The plasma meniscus in an ion source represents the transition from plasma to beam. The plasma meniscus and how the ions are extracted from the plasma are modelled differently for positive and negative ions.

The simplest case is the extraction of a positive ions beam. We consider a plasma with a plasma potential, Φ_P, with respect to the chamber wall. As described in Section 4.1.3, the potential in the plasma sheath naturally falls towards the wall. For a positive ion beam extraction, the model considers that this potential drop is continued by the acceleration field of the extraction potential [48]. We consider having a beam when the potential crosses the wall potential as shown in Figure 4.6(a).

In the case of a negative ion beam extraction, the natural potential fall needs to be reversed [49]. Combination of the potential drop of the plasma sheath and the potential rise of the extraction voltage creates a potential well, sometimes called a virtual cathode. Ions that have high enough thermal energy to overcome this potential well, or that are produced in this region are allowed to escape. Positive thermal ions can become trapped in the potential well, such that this region must still be considered as a plasma. The plasma meniscus is located on the rising part of the potential as shown in Figure 4.6(b).

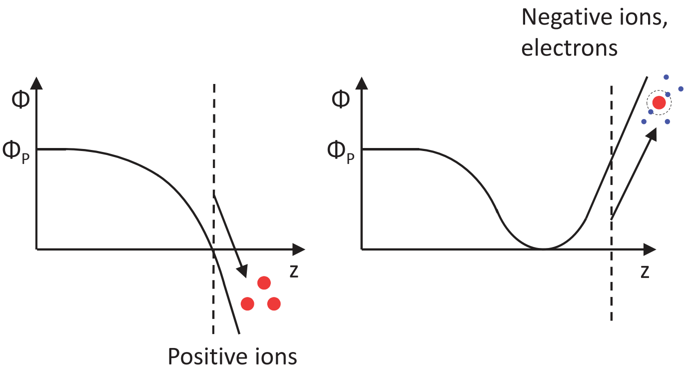

(a) Positive ion beam extraciton. (b) Negative ion beam extraciton.

Figure 4.6: Modelling of positive and negative ion beam extraction from a plasma. The plasma meniscus position is indicated with a dashed line.

4.2.2 Space charge limited extraction from a flat surface

We will now have a closer look at charged particle extraction from a plasma by treating a special case with a relatively simple analytical solution, adapted from [50]. We consider two infinite, parallel, conducting plates, as illustrated in Figure 4.7.

The first plate, which we call our plasma meniscus, is located at $z = 0$ with a potential of $\Phi = 0$. The other plate is the puller electrode at $z = d$ with a potential of $\Phi = V$. We assume that the particles are emitted with an initial velocity of $\mathbf{v} = 0$, which means that the particles are flowing on straight lines in the z-direction, and that the current density, J, is uniform and constant along z. We can now calculate the potential, Φ, as a function of the position in the gap, z, by solving the following three equations:

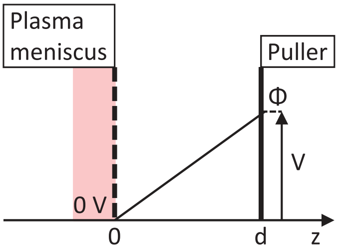

Figure 4.7: Simple one-dimensional model of positive ion beam extraction.

$$\nabla^2\Phi = \Phi''(z) = -\frac{\rho(z)}{\varepsilon_0} \tag{4.29}$$

$$\rho = -J/v \tag{4.30}$$

$$v = \left(\frac{2q\Phi(z)}{m}\right)^{1/2} \tag{4.31}$$

where ρ is the charge density,v the particle velocity along the z-direction, and q and m the particle charge and mass, respectively. We now insert 4.31 into 4.30, and substitute $\rho = -J/v$ from 4.30 into 4.29 to get

$$\Phi''(z) = \frac{J}{\varepsilon_0}\left(\frac{m}{2q}\right)^{1/2}\Phi(z)^{-1/2}. \tag{4.32}$$

By multiplying both sides of Equation 4.32 with $\Phi'(z)$, we can integrate and obtain

$$\Phi'(z) = 2\left(\frac{J}{\varepsilon_0}\right)^{1/2}\left(\frac{m}{2q}\right)^{1/4}\Phi(z)^{1/4}. \tag{4.33}$$

The integration constant here equals zero since $\Phi(0) = 0$ and $\Phi'(0) = 0$. We choose $\Phi'(0) = 0$ as the limit case for the maximum value of J. If $\Phi'(0) < 0$, the field of the surface will push charge carriers back to the emitter. An electron emitter satisfies $\Phi'(0) > 0$, but for a plasma this would pull electrons "out", and decrease d until $\Phi'(0) = 0$. A second integration gives us

$$\frac{4}{3}\Phi(z)^{3/4} = 2\left(\frac{J_{max}}{\varepsilon_0}\right)^{1/2}\left(\frac{m}{2q}\right)^{1/4} z. \tag{4.34}$$

Also here the integration constant is zero because $\Phi(0) = 0$. We have $\Phi(d) = V$, and the relation simplifies to

$$\Phi(z) = V\left(\frac{z}{d}\right)^{4/3}, \tag{4.35}$$

with

$$J_{max} = \frac{4}{9}\varepsilon_0\left(\frac{2q}{m}\right)^{1/2}\frac{V^{3/2}}{d^2}. \tag{4.36}$$

Equation 4.36 is know as the *Child-Langmuir law*, and represents the space charge limit, i.e. the maximum current density that can flow between the plates, given a zero initial velocity of the charge carriers. We observe that to increase the limit for current density, we can either increase the applied voltage, or reduce the extraction gap. We also notice that the maximum current is inversely proportional to the square root of the particle mass. The physical reason is that the velocity of the particles equals $\sqrt{2E/m}$. Lighter particles gain higher velocity, hence have a lower charge density for a given current. This means that the electron current becomes about 40 times higher than the H^- current for equal plasma densities, which must be considered when designing a H^- beam extraction system.

4.2.3 Space charge limit for a negative ion beam with co-extracted electrons

We now apply the Child-Langmuir law to a uniform round beam emitted from a circular area with radius, r, to better represent an ion source. The maximum beam current then becomes

$$I_{max} = \frac{4}{9}\pi\varepsilon_0\left(\frac{2q}{m}\right)^{1/2}V^{3/2}\frac{r^2}{d^2}. \tag{4.37}$$

To correlate this relation with the negative ion beam extracted from the Linac4 ion source, we assume that the beam only consists of electrons and H^- ions. The maximum total current that can be extracted then becomes

$$I_{max} = \frac{4}{9}\pi\varepsilon_0\,(2q)^{1/2}V^{3/2}\frac{r^2}{d^2}\left(R_{H^-}\frac{1}{\sqrt{m_{H^-}}} + R_e\frac{1}{\sqrt{m_e}}\right), \tag{4.38}$$

where R_{H^-} and R_e are the fractions of H^- ions and electrons in the plasma, respectively, and $R_{H^-} + R_e = 1$. The fractions are unknown, but we can estimate them by using the measurable e/H$^-$ ratio, which can be written as

$$e/\mathrm{H}^- = \frac{R_e}{R_{H^-}}\sqrt{\frac{m_{H^-}}{m_e}}. \tag{4.39}$$

Since $R_{H^-} + R_e = 1$, we can express R_{H^-} and R_e as functions of the measured e/H$^-$ ratio:

$$R_{H^-} = \frac{\sqrt{\frac{m_{H^-}}{m_e}}}{e/\mathrm{H}^- + \sqrt{\frac{m_{H^-}}{m_e}}} \tag{4.40}$$

$$R_e = \frac{e/\mathrm{H}^-}{e/\mathrm{H}^- + \sqrt{\frac{m_{H^-}}{m_e}}} \tag{4.41}$$

The expression of the space charge limited current for a beam consisting of electrons and H$^-$ ions yields

$$I_{max} = \frac{4}{9}\pi\varepsilon_0\left(\frac{2q}{m_e}\right)^{1/2} V^{3/2}\frac{r^2}{d^2}\left(\frac{1}{e/H^- + \sqrt{\frac{m_{H^-}}{m_e}}} + \frac{e/H^-}{e/H^- + \sqrt{\frac{m_{H^-}}{m_e}}}\right), \tag{4.42}$$

where the left and right part of the sum correspond to the contribution from H$^-$ ions and electrons, respectively.

4.2.4 Model of the plasma meniscus dynamics

Our examples have so far considered a beam emitted from a flat surface. However, a better approximation of the plasma meniscus' shape for a beam emitted from a circular aperture is a sphere. This sphere can change between a convex sphere, a flat surface, and a concave sphere depending on the extraction field and the plasma density. We describe this effect by using the *Langmuir-Blodgett equation*. This relation defines the limiting current between two concentric spheres [51], and is given by

$$J_{max} = \frac{4}{9}\varepsilon_0\left(\frac{2q}{m}\right)^{1/2}\frac{V^{3/2}}{r_0^2\alpha^2}, \tag{4.43}$$

where α is a function of the ratio of the radii r and r_0 of the spheres, r_0 being the radius of the emitter. We immediately recognize the similarity to the Child-Langmuir law where d has been replaced by $r_0\alpha$. The values of α can be obtained in terms of the following series:

$$\alpha = \gamma - 0.3\gamma^2 + 0.075\gamma^3 - 0.0143182\gamma^4 + 0.0021609\gamma^5 - 0.00026791\gamma^6 + \ldots, \quad (4.44)$$

where $\gamma = \ln(r/r_0)$. This series can be used to calculate α accurately to three places of decimals for values of r/r_0 up to 5.

We apply Equation 4.43 to our example by introducing the plasma meniscus as a part of an emitting sphere, and approximate the collecting sphere by a test sphere at the position of the puller. The two spheres are concentric, with a constant difference in radius, d. Our emitting plasma meniscus can either be the convex shaped inner sphere, or the concave shaped outer sphere as shown in Figure 4.8. Equation 4.44 applies for both cases, the difference being that γ changes sign, and thus the sign of the alternate terms.

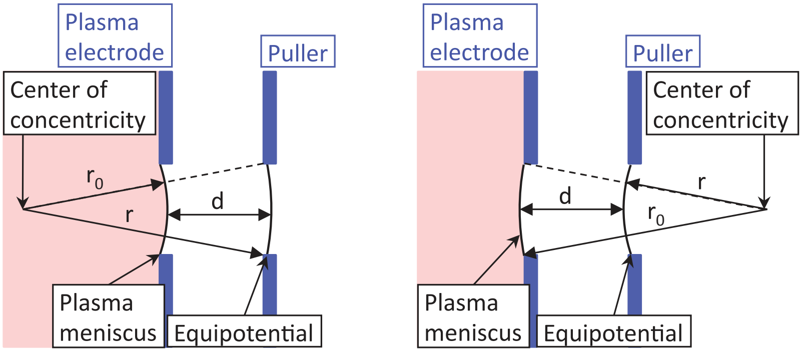

(a) Convex sphere.
(b) Concave sphere.

Figure 4.8: Model of plasma meniscus as part of an emitting shpere with radius, r_0, with the collecting sphere with radius, r, and with a constant distance, d, between the two radii.

Because we assume that d is constant, we can calculate α as a function of only the radius of the emitting sphere, r_0. In this way we can visualize how the plasma meniscus changes shape when for instance the extraction voltage is modified. Figure 4.9 plots r_0 as a function of $r_0\alpha$ where the distance between the two spheres has been fixed to 7 mm. As J_{max} is constant, $r_0\alpha$ is proportional to $V^{3/4}$. The plotted range is between $r/r_0 = 0.2$ and $r/r_0 = 5$, i.e. where α can be calculated accurately with Equation 4.44.

Starting from a low $r_0\alpha$, we see that the plasma meniscus is convex making the plasma bulge out of the plasma aperture. As $r_0\alpha$ increases, the radius of the convex sphere increases as well, and the plasma meniscus becomes flatter. When $r_0\alpha$ appraoches d, which in this case is 7 mm, r_0 increases towards infinity corresponding to two parallel plates. The Langmuir-Blodgett equation then becomes the same as the Child-Langmuir law (Equation 4.36). A further increase of $r_0\alpha$ makes the shape of the plasma meniscus concave with a smaller and smaller radius.

If the ion current provided by the plasma generator is lower than the space charge current limit, which often is the case, the effect would be similar to an increased extraction field. To compensate for the resulting over-focused ion beam, one can either decrease the extraction voltage or increase the extraction gap. Figure 4.10 illustrates the effects of the extracted current on the beam quality with a constant extraction voltage. The simulations show a negative ion beam extracted from the plasma generator to the left and through the puller to the right for a low plasma density, a matched condition, and an over-dense plasma, respectively. All simulations use an extraction voltage of 15 kV, and the beam consists of H^- ions and electrons. Only the H^- current density has been varied while the e/H^- ratio has been fixed to 50. The plasma aperture has a diameter of 6.5 mm, and the extraction gap is 7 mm. Case (a) shows an extraction of a 5 mA H^- beam, with which the strong electrical field gives an over-focused beam. In (b), the beam current is 20 mA and shows the ideal case where the plasma meniscus is slightly curved and provides a close to parallel beam. In case (c), the beam current is 50 mA, and here the beam is divergent and part of it is even lost on the puller. We can also arrive at the same conclusion by combining Equation 4.42, and Equation 4.43. The result estimates $r_0\alpha$ for these three examples of a negative ion beam with co-extracted electrons. The dashed lines in Figure 4.9 show the calculated values of $r_0\alpha$, which give an estimate of r_0. We see that these results correspond well with the plasma meniscus shapes in Figure 4.10.

The effect of the extraction voltage on the plasma meniscus can also be explained through simple reasoning. When for instance a negative beam is extracted, negative charges will fill the area in front of the plasma meniscus. This effect causes a drop of the voltage in the region in front of the plasma meniscus, and starts to attract positive charges. The region then consists of a mixture of positive and negative charges, which we now can consider to be a plasma. The plasma meniscus has then moved closer to the puller. By raising the puller voltage, the electric field now becomes stronger in the region in front of the plasma meniscus. The positive charges are now repelled, and the plasma meniscus moves away form the puller towards the plasma generator.

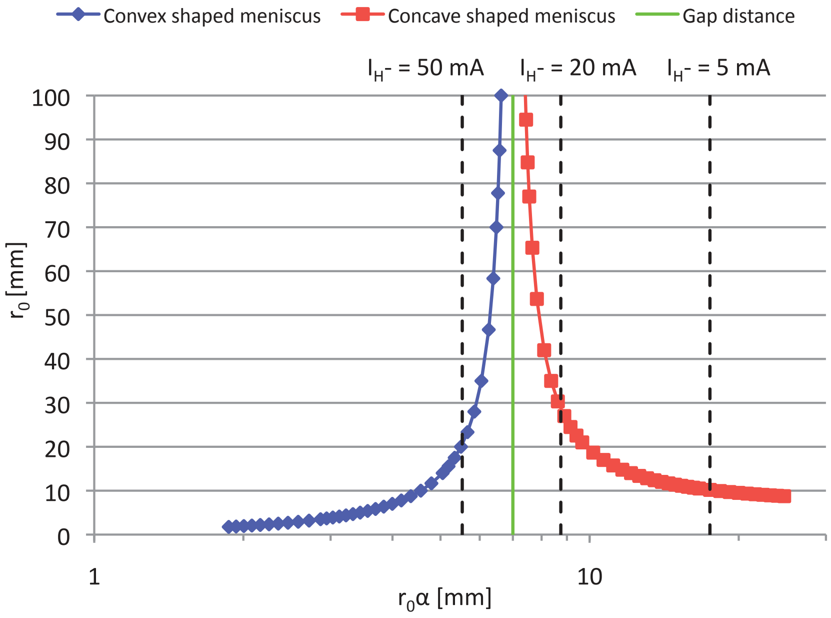

Figure 4.9: Evolution of a shperically shaped plasma meniscus radius, r_0, as a function of $r_0\alpha$. The dashed lines show the value of $r_0\alpha$ and r_0 for three different H^- beam currents with an e/H^- ratio of 50, extracted over a 7 mm gap by a 15 kV extraction field.

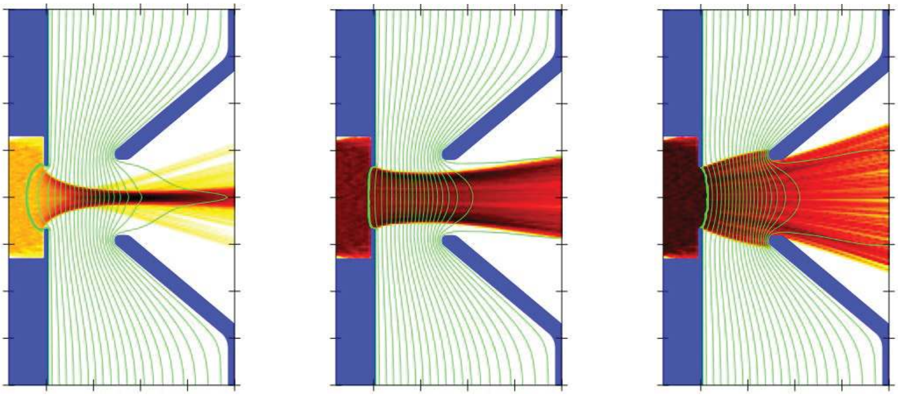

(a) I_{H^-} = 5 mA: too low plasma density and the beam is over-focused.

(b) I_{H^-} = 20 mA: matched condition and beam is almost parallel.

(c) I_{H^-} = 50 mA: too high plasma density and the beam is divergent.

Figure 4.10: Influence of plasma density on ion beam optics of an H^- ion beam with an e/H^- ratio of 50. The extraction voltage is 15 kV and the gap distance is 7 mm.

4.2.5 Plasma electrode geometry

The shape of the plasma electrode affects the beam quality. A flat surface makes the equipotential lines near the edge of the aperture to have a sharp bend, causing particles here to be extracted with a large angle. These particle leads to beam aberration, which results in an undesired increased emittance. Ideally, the outside of the plasma electrode should have an angle that follows the equipotential lines, making a smooth transition between the electrode and the plasma meniscus.

For space charge limited surface emitted electrons, there exists a perfect solution that gives a parallel beam extracted from the cathode [52]. The solution is to have an electrode shape around the cathode with a 67.5° angle with respect to the emitting surface normal. This is called a *Pierce electrode*. However, for plasma ion sources, this solution does not apply because the particles are emitted from a plasma with varying starting conditions as described in Section 4.2.4. Figure 4.11 compares the normalized rms emittance of three ion beams with different currents as a function of the angle of the plasma electrode. The beams consist of H^- ions and electrons with a fixed e/H^- ratio of 50, with H^- ion beam currents of 10 mA, 20 mA, and 30 mA. For a low beam current the extraction field pushes the plasma meniscus towards the source, giving the equipotential lines a sharp curve at the edge of the plasma electrode. In this case, a small angle gives the optimum emittance. For higher beam currents, the optimum angle becomes larger.

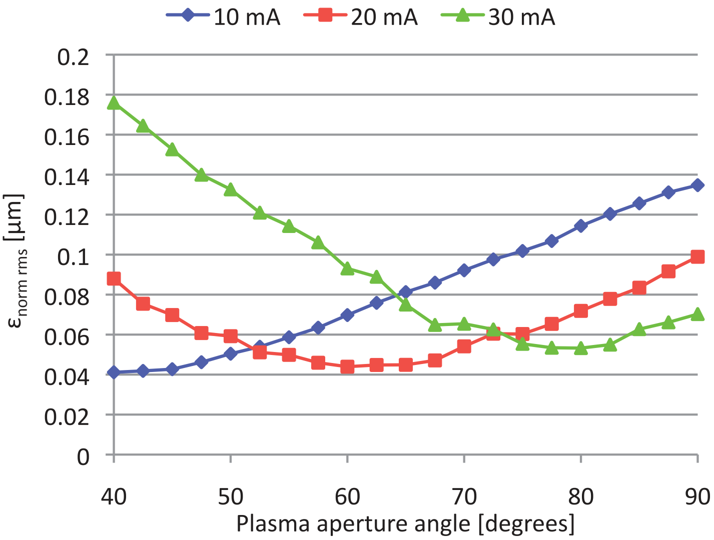

Figure 4.11: Normalized rms emittance of three H^- ion beam with different currents as a function of the plasma electrode angle with respect to the beam axis. The e/H^- ratio is 50 for all three cases.

Figure 4.12 shows the difference between two extraction geometries for a 20 mA H^- beam with an e/H^- ratio of 50, and with a voltage of 15 kV across a 7.0 mm extration gap. The first case has a flat plasma electrode, and the second has a plasma electrode shaped with a 65° angle. We observe, in the case of the flat electrode, that the electric potential lines (in green) have to bend around the sharp edge of the plasma aperture, creating electric fields perpendicular to the beam axis. The extracted particles at the edges have large transverse velocities, which cause an increased emittance. The 65° angle on the outside of the plasma chamber shapes the electric potential lines, and the meniscus surface is more homogeneous. Here, the extracted beam is more parallel, and the emittance is reduced by more than a factor two.

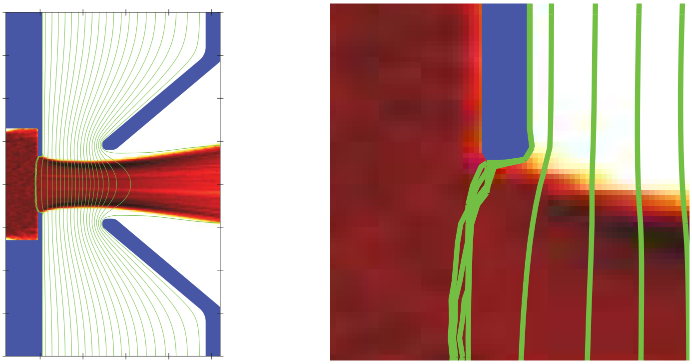

(a) Flat plasma electrode.

(b) Zoom of the flat plasma electrode.

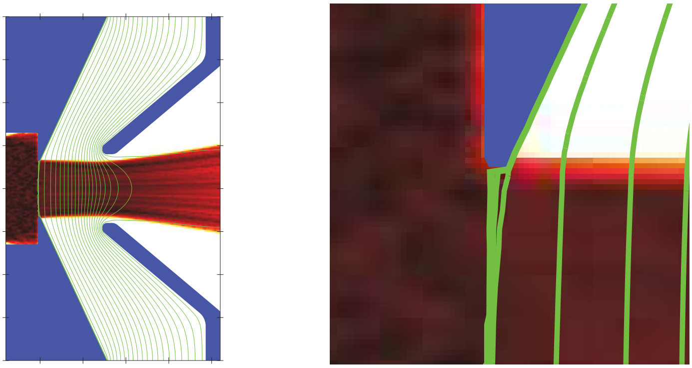

(c) Plasma electrode with a 65° angle.

(d) Zoom of the plasma electrode with a 65° angle.

Figure 4.12: Influence of the shape of the plasma electrode on the ion beam optics. The curved equipotential lines at the edge of the flat plasma aperture lead to beam aberrations that increase the rms emittance.

4.3 Ion beam transport at low energy

The LEBT is the part of the particle accelerator between the ion source and the first accelerating structure. The ion beam energy here corresponds to the plasma generator voltage, and is normally in the order of 10-100 keV. The purpose of the LEBT is to shape and steer the ion beam such that it matches the input of the accelerator, which in the case of Linac4 is an RFQ.

4.3.1 Optical elements

In the region of low energy, the space charge dominates and causes the beam to expand. It is therefore important to focus the beam as early as possible to avoid beam losses. The focusing is made with either magnetic or electric fields. At higher energy, however, only magnetic fields are efficient because the force is proportional to the particle velocity. When v approaches c a magnetic field of 1 T corresponds to an electric field of 300 MV/m.

With electrostatic devices, the particle trajectory only depends on the energy per charge. Hence, all charged particles starting from rest will follow the same trajectory path in a purely electrostatic system (the time of flight does still depend on the particle mass). By using magnetic fields instead, the trajectories depend on the charge-to-momentum ratio, which is not equal for all charged particles that have been electrostatically accelerated. Magnetostatic devices thus allow separation of charged particles of different mass or energy.

Electrostatic lens

An *electrostatic lens* is simply constructed of two hollow electrodes with a voltage difference between them as shown in Figure 4.13(a). In the gap between the electrodes, the electric field curves as a result of the curved equipotential lines. An off-axis positive ion that is travelling in the z-direction will first see a force pointing towards the beam axis, then a force pointing outwards. In either polarity, the electrostatic lens provides a net focus to the beam. The reason is because the focusing force is at the low beam energy side of the lens, and therefore has a larger impact on the particles of the beam.

The focal length, f, of an electrostatic lens is given by [53]

$$f = \frac{4L\left(\sqrt{V_2/V_1}+1\right)}{V_1/V_2+V_2/V_1-2}, \tag{4.45}$$

where L is the gap distance between the two electrodes with potentials V_1 and V_2. V =0 V is where the beam kinetic energy is zero.

Einzel lens

A special case of the electrostatic lens is the *Einzel lens* (Figure 4.13(b)), which is a three-electrode system with the middle electrode at a different potential. This type of lens can work in either accelerating or decelerating mode. Accelerating mode means that the ions are accelerated into the lens, and then decelerated at the exit. In this mode, as the ions pass through the lens, they will first be focused at the end of the low energy side, then defocused in the middle electrode, and focused again at the end. The opposite applies for a decelerating lens. As for the electrostatic lens, the focusing happens on the low energy side of the lens. This means that a decelerating lens is more effective than the accelerating one because of the reduced velocity of the ions where the focusing occurs. On the other hand, in this configuration, the space charge effects on the beam are stronger in the low velocity region, and causes larger emittance growth.

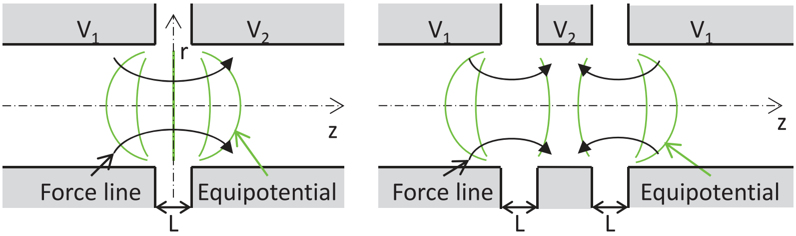

(a) Electrostaic lens, $V_1 > V_2$.   (b) Einzel lens, $V_0 > V_E$.

Figure 4.13: Two examples of electrostatic focusing. The radial component of the electric field focuses (or defocuses) the charged particles. The focusing takes place at the low energy side of the lens, resulting in a net focus of the beam.

To estimate the focal length of the Einzel lens f_E, we add the focusing effect of two electrostatic lenses (Equation 4.45) with equal gap lengths as shown in Figure 4.13(b). To simplify the problem, we do not consider the drift between the two gaps.

$$\frac{1}{f_E} = \frac{1}{f_1} + \frac{1}{f_2} = \frac{V_1/V_2 + V_2/V_1 - 2}{4L\left(\sqrt{V_2/V_1} + 1\right)} + \frac{V_2/V_1 + V_1/V_2 - 2}{4L\left(\sqrt{V_1/V_2} + 1\right)}. \tag{4.46}$$

We multiply Equation 4.46 by V_1V_2/V_1V_2, and simplify the relation to:

$$\frac{1}{f_E} = \frac{(V_1 - V_2)^2}{4LV_1V_2}. \tag{4.47}$$

Figure 4.14 compares of the focal lengths of an electrostatic lens and an Einzel lens. For the Einzel lens, the beam exits with an energy corresponding to V_1, whereas for an electrostatic lens the beam obtains an energy corresponding to V_2.

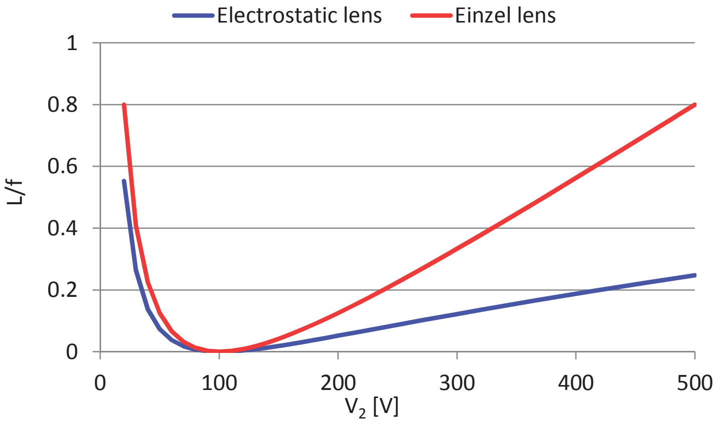

Figure 4.14: Comparison of the focal length (L/f) of an electrostatic lens and an Einzel lens. V_1 = 100 V.

Solenoid

A solenoid provides a magnetic field to focus the ion beam. Figure 4.15 shows a simple solenoid in cylindrical co-ordinates, r, θ, z. When a beam of charged particles travels along the z-axis and enters a solenoid, it first interacts with the r directed fringe field, which results in a force in the θ-direction. This force causes the beam to spiral. Inside the solenoid, v_θ now interacts with the now z-directed B-field, and creates a force pointing to the centre of rotation, which focuses the beam. The force will point to the centre irrespective of the ion beam charge, and the direction of the B-field. At the exit, the beam encounters the opposite fringe field, which cancels the beam rotation.

The focal length, f, of a solenoid (considered as a thin lens) is given by [50]

$$\frac{1}{f} = \left(\frac{q}{2mv}\right)^2 \int B^2 dz. \tag{4.48}$$

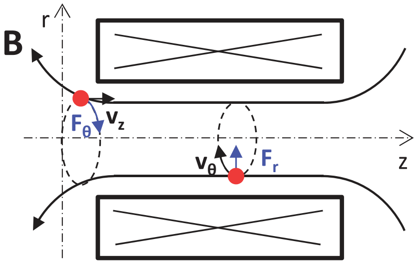

Figure 4.15: Scheme of particle dynamics in a solenoid magnet.

Dipole

Both magneto- and electrostatic dipoles, so-called *steerers*, are commonly used for beam corrections in the horizontal and vertical plane. Electric steerers are often used for beam chopping because of their fast rise time, whereas magnetic steerers are effective for beam position corrections. Magnetostatic dipoles, which are able to select ions according to the charge-to-momentum ratio, can also separate ions of different charge states, or measure the beam energy spread. This application is called a spectrometer.

4.3.2 Compensation of beam space charge

An ion beam consists of particles with the same charge polarity. Naturally, these particles will repel each other, and cause the beam to expand both transversally and longitudinally. This is what we call the *beam space charge effect*. The effect is strongest at low energy where the charge density is high. The lower longitudinal momentum also means that the momentum given by space charge has a larger proportion of the total momentum.

The potential well created by the ion beam forms a trap for oppositely charged particles in regions without electric fields. When these charges are trapped, they will lower the depth of the potential well, and reduce the space charge effect. We call this *space* *charge compensation*. The origin of the compensating particles is mostly due to ionization of the background gas in the beam pipe by the ion beam. For a positive ion beam, the compensating particles are the electrons created by the ionization, whereas for a negative ion beam, the space charge compensation comes from positive ions. In principle, the space charge compensation is just as effective for a positive as for a negative ion beam.

For a pulsed beam system, the space charge compensation is not immediately effective, but needs time to produce enough compensating particles. The characteristic space charge compensation time, τ, is the time it takes for a particle of the beam to produce a neutralizing particle of the residual gas:

$$\tau = \frac{1}{\sigma_i n_g v}, \tag{4.49}$$

where σ_i is the ionization cross section of the incoming particles on the residual gas, n_g the gas density in the beam line, and v the velocity of beam [54]. Measurements at the Linac4 test stand have shown space charge compensation times in the order of 100 µs for a 45 keV H^- beam with a residual hydrogen gas pressure of 3×10^{-6} mbar, which corresponds well with the theoretical value [55]. In a magnetic LEBT, the rise time of pulsed ion beams is dominated by the space charge compensation transient time, which is in the order of several tens of microseconds. A fast chopping system can be inserted to decrease rise times and reach orders of hundreds nanoseconds [56].

Measurements suggest that using heavier gases enhances the space charge compensation effect [57]. The most obvious choice of residual gas, however, is to use the same as the ion beam in order to not contaminate the ion source. The choice of gas must also take into account the surrounding accelerator elements and the pumping systems.

4.3.3 Particle impact induced electron emission from surfaces

Secondary electron emission from surfaces plays an important role in ion sources. In the case of beam current measurements with a Faraday cup for instance, a negative potential in front of the cup prevents secondary electrons emitted from the cup to escape and alter the measurement. Likewise, for negative ion sources where electrons are co-extracted with the beam, secondary electron emission from the electron dump needs to be taken into account for a correct electron current estimation. For a better understanding of the beam optics of the extraction system, secondary electrons emitted from the extraction electrodes need to be considered.

Theoretical approach

Emission of secondary electrons can originate from impact by ions and atoms, or electrons. We define the secondary electron emission induced by ions/atoms as γ, and by electrons as δ. There are three processes that give rise to secondary electron emission by particle impact [58]:

1. *Kinetic emission* relates to the transfer of the kinetic energy from the incoming projectile (ion or electron) to an electron in the target through a collision. Some of the excited electrons will escape the target provided that they migrate towards the surface with sufficient energy to overcome the potential barrier. The following model describes the mechanism of kinetic emission for impacting ions or electrons [59]: (1) *Primary ionization* of target atoms via direct Coulomb interaction with the projectile, or secondary ionization of target atoms by recoiling target atoms (only for heavy projectiles), energetic electrons, and possibly photons. (2) *Transport* of the liberated electrons towards the surface. (3) *Penetration* of electrons through the surface barrier into vacuum.

   The kinetic emission yield, γ_k for impacting ions (δ_k for electrons), depends on the projectile kinetic energy, E, through the following relation [59]:

   $$\gamma_k = \Lambda D(E). \tag{4.50}$$

   Here Λ is a target dependent constant describing transport of electrons inside the solid and their ejection through the surface barrier. This constant is in principle the same for ions and electrons for a given target material. However, primary electrons might be reflected back through the surface and excite additional electrons on their way out. $D(E)$ is a function that represents the production mechanism of electrons. At low projectile energies, primary ionization is dominant and the $D(E)$ is proportional to the ionization cross section of the target atoms. At higher energies, cascades induced by energetic excited electrons also produce electrons. $D(E)$ then becomes proportional to the *stopping power*, $S(E)$, which is the energy loss of the impacting particle per unit path length.

   γ_k has a maximum value of 1 to 5, and δ_k is about unity.

2. *Potential emission* occurs for impacting particles with a potential energy, i.e. ions. As the surface is approached, a target electron tunnels into a vacant electron shell of the projectile as illustrated in Figure 4.16. A secondary electron can then be emitted from the surface by an Auger transition if the ionization energy of the

incoming ion exceeds twice the material work function. This mechanism is most effective at low kinetic energy since the electron has to escape the surface before the ion reaches the surface. A fast travelling ion will probably hit the surface in a still ionized state.

The potential emission coefficient, γ_p, has been estimated to

$$\gamma_p = \frac{0.2}{E_F}\left(0.8E_i - 2W\right), \tag{4.51}$$

where W is the work function of the material, E_F the Fermi energy of the material, and E_i the ionization energy of the incident particle [58].

As an example, the potential emission coefficient for protons impaction on a gold surface is 0.02.

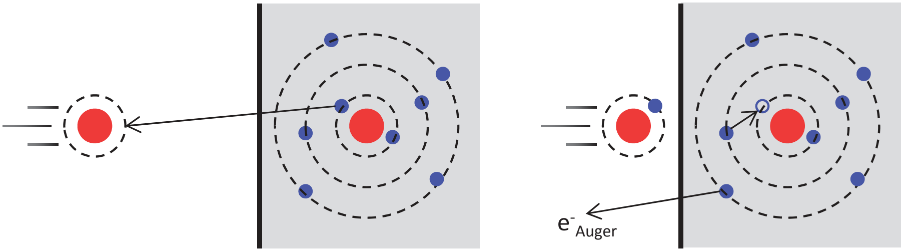

Figure 4.16: The potential energy of the impacting positive ion captures an electron from the target surface. A secondary electron can be emitted from the surface by an Auger transition.

3. *Reflections* of incident electrons. This process is strictly speaking not a secondary ejection process, but backscattering of incoming electrons. The reflection coefficient, η, varies with the target nuclear charge, Z, roughly as [58]:

$$\eta = 0.150 \ln Z - 0.206, \; Z \geq 4. \tag{4.52}$$

   The coefficient varies little with the energy of the incoming electron, and Equation 4.52 is suggested to be used in the energy region 0.3 keV to 50 keV.

   In the case of an iron target ($Z = 26$), the reflection coefficient is equal to 0.28.

In summary, secondary electron emission induced by ion (or atom) impact consists of kinetic and potential emission: $\gamma = \gamma_k + \gamma_p$. Secondary electrons originating from electron impact consist of kinetic emission and reflections: $\delta = \delta_k + \eta$.

Experimental data

Secondary electron emission coefficients can also be found from experimental data. Figure 4.17 plots the number of secondary electrons emitted per incoming electron (δ) as a function of the energy for two different target materials [60]. In this plot we see that the emission coefficient is correlated with the stopping power of electrons [61], which means that δ is dominated by kinetic emission.

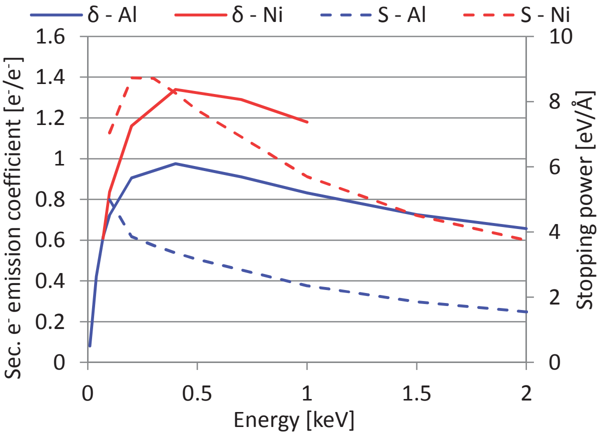

Figure 4.17: Solid lines: energy dependent electron induced secondary electron emission coefficients for an aluminium and a nickel target [60]. Dashed lines: energy dependent electron stopping power for aluminium and nickel [61].

Figure 4.18 contains relevant information for negative hydrogen ion sources. Here the secondary electron emission coefficients for protons (H^+), and neutral and negative hydrogen (H^0 and H^-) are plotted [59, 62, 60]. We observe that for energies below 8 keV, the secondary electron emission coefficient is similar for H^0 and H^-. However, at higher energies, an extra contribution adds to the H^- yield, reaching 0.2 electrons/projectile at E = 16 keV. The explanation is as follows [59]: the second electron of the H^- is bound very weakly in comparison with the first one. Therefore, we expect that this electron detaches as soon as the ion hits the surface. The now free electron has the same impact velocity as the H^- ion, and the energy thus equals the H^- energy multiplied with the quotient of the electron and H^- masses, $E_e = E_{H^-} \times m_e/m_{H^-}$. Plotted with dashed lines are the differences in secondary electron emission for H^- and H^0, and the experimental data for electron induced electron emission where the energy has been re-calculated to that of the impacting H$^-$ ion. These lines correspond well and suggest that the detached electron is causing emission of secondary electron independently of the H$^-$ ion. For H$^-$ ion energies of 50 keV, this would mean a contribution of 0.5 to the secondary electron emission yield of H^0.

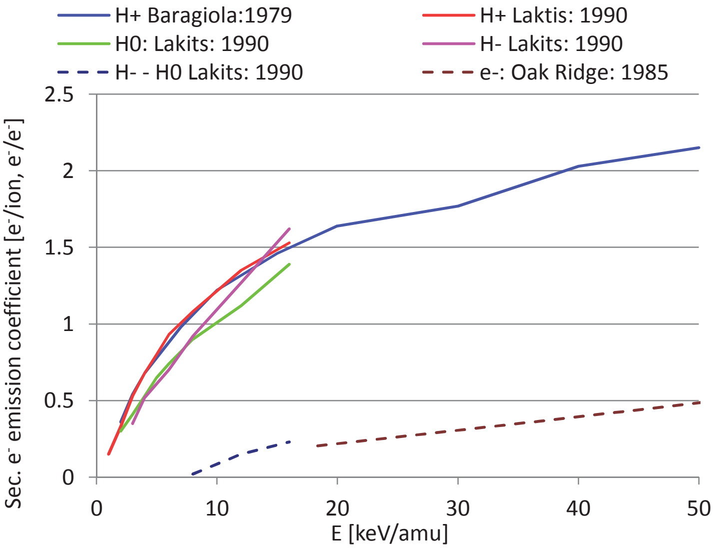

Figure 4.18: Solid lines: energy dependent secondary electron emission coefficients induced by H$^+$, H^0 and H$^-$ on a gold target [59]. Dashed lines: difference in secondary electron emission for H$^-$ and H^0, and experimental data for electron induced electron emission [60].

Figure 4.19 shows three other factors that influence the secondary emission coefficient [60]. An increased Z-value of the target material slightly increases γ for a 100 keV proton beam. The angle between the incoming projectile and the target surface plays a bigger role; an angle of 70° to the surface normal triples γ for a 120 keV proton beam on a nickel target. The dependency follows a $1/\cos\theta$ fit. A third dependency is the cleanness of the target material. A chemically etched molybdenum surface bombarded with protons emits three times more secondary electrons than a sample that was flashed to 1750°C.

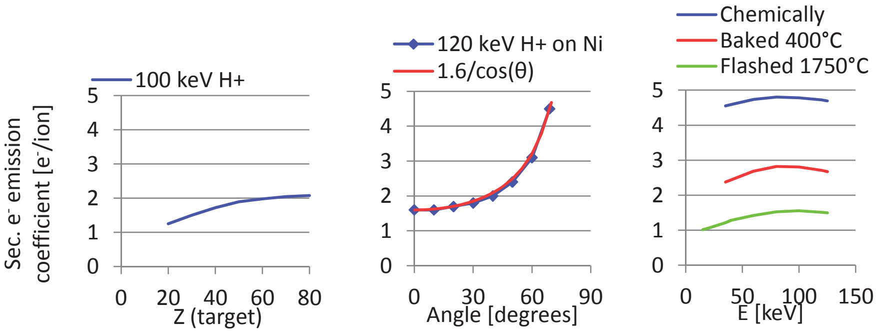

(a) γ as a function of the Z-value of the target material.

(b) γ as a function of the angle of the incident particle. 0° is normal to the surface.

(c) γ as a function of the degassing technique of the surface.

Figure 4.19: Effects on the secondary electron emission coefficient, γ.

4.4 Simulation of ion beam extraction from a plasma

For modelling of plasma ion sources, there exist a vast number of computer codes. *Plasma codes* simulate particle dynamics using particle in cell (PIC) or fluid models, or a combination of the two. These codes can predict the plasma processes leading to ion extraction to a reasonable accuracy. However, the calculation time in three-dimensions (3D) can be up to several weeks on high-performance parallel computers. The codes are also often customized to a specific problem, and are therefore not the best choice for the design of ion source extraction systems where several iterations for optimizing the geometry is necessary.

So-called *trajectory codes* tracks particle trajectories through beam transport lines. For standard optical elements, the particle trajectories can be calculated by using transfer matrices for each element, and the drifts spaces between them [63]. Ion beam extraction calculations often use very non-linear fields which do not fit well with the linearized models, and so the calculations are performed using tracking through the field configuration given by a finite element solver. Before staring the work on the new ion beam extraction system, the extraction system for a copy of the DESY H^- ion source (described in Section 5.1) was simulated with such a code: Opera/Scala by Cobham Vector Fields [46]. Even though this tool gave useful results, its predictive power was limited by the lack of modelling of the plasma to beam extraction process. The simulations were prepared by creating a fixed shape conductor at the plasma aperture, from where the particles were emitted, as shown in Figure 4.20. This particle emitter then represented the plasma meniscus. However, the shape of this plasma meniscus changes as a function of the plasma density and the extraction voltage when a beam is extracted from a plasma, as explained in Section 4.2.4. The disadvantage of particle trajectory codes, such as Opera/Scala, is that the user predefines the emitter/plasma meniscus shape, whereas the simulation tool should calculate it. For this purpose, a *plasma extraction code* is needed.

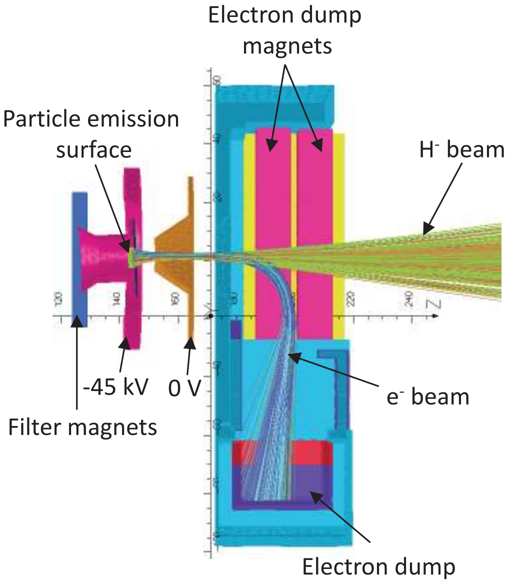

Figure 4.20: Simulation output from Cobham Vector Fields Opera/Scala. Dimensions are in mm.

Plasma extraction codes are similar to trajectory codes, but are in addition capable of tracking the beams from a space charge compensated plasma to an unneutralized extraction region. This is done by including the space charge from the beam to the simulation grid and using analytical models for the plasma space charge compensation. The result is a fast and sufficiently accurate modelling of the plasma meniscus formation and the beam space charge effects [64]. There exists a small selection of plasma extraction codes including PBGUNS [65] and IGUN [66] that can model two-dimensional and cylindrical symmetric, positive and negative ion plasma extraction systems. For three-dimensional simulations, there are KOBRA-INP [67] and IBSimu [1].

Out of these simulation tools, IBSimu was chosen for the design of the H^- beam extraction system. The code is not distributed as a pre-compiled computer program, but it is made as a C++ library, which contains the modules/classes performing the calculations [64]. A specific user-made program written in C++ then performs each simulation, which uses the computational tools of the IBSimu library. This means that the user needs to be familiar with the C++ language, and to have a good understanding of how IBSimu performs the calculations. In return, the user has the liberty to replace the built-in modules, and easily integrate geometries and magnetic fields from other simulation tools. The code includes a graphical user interface for plotting geometries, fields and particle trajectories, and can also give output in form of images and text files. As the code is primarily designed for Linux, there is the possibility to use batch processing that automatizes the simulations for systematic studies.

4.4.1 Description of IBSimu simulations

Ion Beam Simulator or IBSimu is a computer simulation package for ion optics, plasma extraction and space charge dominated ion beam transport [68]. One way to model time-independent extraction systems is by solving Poisson's equation

$$\nabla^2\Phi = -\frac{\rho}{\varepsilon_0}, \tag{4.53}$$

which relates the electric potential, Φ, with the space charge, ρ, and the time-independent Vlasov equation

$$\mathbf{v}\cdot\nabla f - \frac{q}{m}(\mathbf{E}+\mathbf{v}\times\mathbf{B})\cdot\frac{\partial f}{\partial \mathbf{v}} = 0, \tag{4.54}$$

which describes the behaviour of a particle distribution $f(\mathbf{r},\mathbf{v})$ in an electric field $\mathbf{E} = \nabla\Phi$ and an independent magnetic field $\mathbf{B}$ [64].

IBSimu solves the above given problem by representing Φ, ρ, and $\mathbf{E}$ on a grid of computation points in a bound geometry. The nodes that are on the boundaries of the simulation domain are constrained by a boundary condition. This boundary condition is either a Dirichlet boundary condition (fixed potential), or a Neumann boundary condition (fixed derivative with respect to the normal of the boundary).

The solution to the extraction system model is found by an iterative process called the Vlasov-Poisson iteration, and is shown as a flow chart in Figure 4.21. The iteration starts by an initial guess of the electric potential by solving the Laplacian $\nabla^2\Phi = 0$ in the geometry. The potential is assumed to be Φ_P inside the plasma for a positive ion plasma extraction, and 0 for a negative ion plasma extraction. If no plasma is present, as for a beam transport problem, the Laplacian is solved without the fixed potential plasma volume to provide a starting point for the iteration. The resulting Φ is then used to calculate the particle trajectories starting from a plasma, or a defined starting point. Next the simulation tool uses a method called ray tracing, which integrates the equations of motion of the particles in the calculated **E** and imported **B**-fields. The space charge density based on the ray tracing is then calculated on the grid. This space charge density is used together with the analytical space charge density from the plasma model to provide the electric potential, Φ, for the next iteration round. To avoid that the change in Φ overshoots and prevents convergence, the correction step is damped at each iteration round. When convergence is reached, the simulation data are saved, and/or diagnostics are made before the program ends.

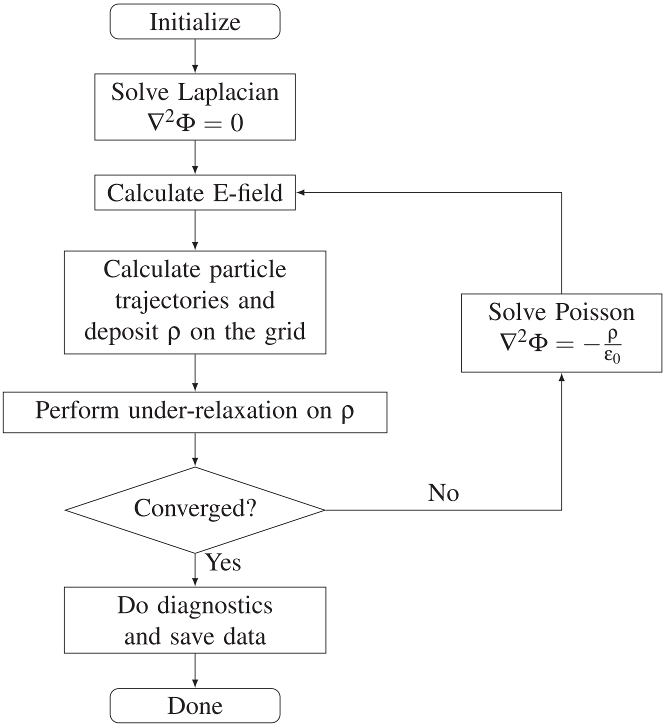

Figure 4.21: Flowchart of the IBSimu simulations. Figure adapted from [64].

4.4.2 Ion plasma extraction model

IBSimu restricts the modelling of the plasma beam formation to the sheath region (described in Section 4.1.3). The extracted positively or negatively charged particles arrive to this region with an initial velocity caused by the acceleration in the pre-sheath, and the charge density of the compensating charges is assumed to be dependent only on the potential [64].

Positive ions

For a positive ion beam extraction (Figure 4.22(a)), the compensating electron charge density is given by

$$\rho_e = \rho_{i0} \exp \frac{e\,(\Phi - \Phi_P)}{kT_e}. \tag{4.55}$$

The electron density equals the ion density at the potential of the sheath edge, and then decays exponentially as a function of the potential towards the extraction. The ray traced positive ions are injected at the pre-sheath/sheath boundary (at ϕ_P) with a velocity not less than the Bohm velocity, v_B, to achieve convergence.

Negative ions

In the negative ion beam extraction model, negatively charged particles form a potential well at $\Phi = 0$ V between the bulk plasma and the extraction region (Figure 4.22(b)). The potential increases towards the plasma because of the plasma potential, and towards the extraction region due to the acceleration voltage. The potential well acts as a trap for thermal positive ions, whereas fast positive ions are reflected back to the plasma by the extraction field.

The simulation region includes the area from the zero potential ion plasma sheath towards the extraction region, and is described by Poisson's equation with

$$\rho = \rho_{neg} + \rho_f + \rho_{th}, \tag{4.56}$$

where ρ_{neg} is the space charge density of the negative ray traced particles, ρ_f is the space charge of the fast positive ions, and ρ_{th} is the space charge of the trapped positive thermal ions. The thermal ion species is assumed to have a Maxwellian velocity distribution associated with the space charge distribution

$$\rho_{th} = \rho_{th0} \exp\left(\frac{-e\Phi}{kT_p}\right), \tag{4.57}$$

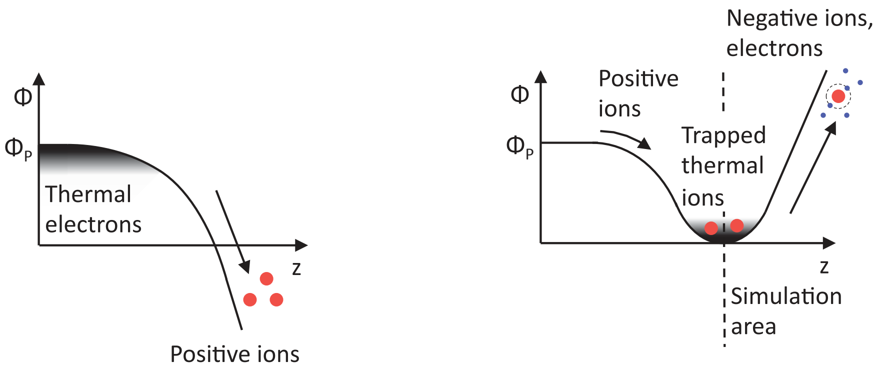

(a) Positive ion beam extraction model. Thermal electrons populate the plasma, and the extraction field accelerates the positive ions.

(b) Negative ion beam extraction model. Thermal positive ions populate the potential well at the plasma electrode potential, the extraction field accelerates negatively charged particles.

Figure 4.22: Modelling of positive and negative ion beam extraction from a plasma. Figure adapted from [64].

where ρ_{th0} is the thermal positive ion space charge density at the wall potential, and T_p is the thermal positive ion temperature. The space charge distribution of the fast ions is

$$\rho_f = \rho_{f0}\left(1 - \operatorname{erf}\left(\frac{\Phi}{\Phi_P}\right)\right), \tag{4.58}$$

where ρ_{f0} is the fast ion space charge density at the wall potential. The space charge neutrality at the wall requires

$$\rho_{neg0} + \rho_{f0} + \rho_{th0} = 0, \tag{4.59}$$

where ρ_{neg0} is the negative beam space charge density at the definition plane at zero potential. The beam space charge density is given by

$$\rho_{neg0} = \sum_j \frac{J_j}{v_{0,j}}, \tag{4.60}$$

where J_j is the current density and $v_{0,j} = \sqrt{2E_{0,j}/m_j}$ is the initial drift velocity of the extracted species j.

The negative ions and electrons starts at a definition plane and are ray traced on artificially straight lines until they are accelerated by the extraction field at the self calculated plasma sheath. In most negative ion sources, however, there is a strong magnetic field in this area that influences the particle trajectories. Because the real particle dynamics is difficult to model in this type of code, the magnetic field is suppressed in the plasma to provide an even flux to the plasma sheath. This suppression is cancelled once the particles have travelled to a potential higher than a certain threshold value, typically 1-20 V. The exact value is of little importance as the ion optics is not very sensitive to this parameter in most cases [69].

Chapter 5

Development of the Linac4 H^- ion source

Linac4 was first proposed in 2002 for injecting H^- ions into the PSB from the normal-conducting part of the future SPL [70]. The specification for the ion source was a pulsed H^- ion beam of 400 µs, 45 keV beam energy, 80 mA beam current within a normalized rms emittance of 0.25 µm, and at a repetition rate of 2 Hz [20]. These requirements were higher than the performances of any existing source, and soon began a study of which type of ion source to use. The first stage of the development program was testing a microwave-driven source, using the existing experience with the ECR technology for the heavy-ion physics program at CERN (Linac3) [71]. The tests early revealed that this type of ion source could not meet the requirements in time. Instead, the strategy changed to copy and upgrade one of the ion sources operating close to the Linac4 requirements. Five candidates were considered: the magnetron source of BNL, the 2 MHz RF source and the magnetron of DESY, the Penning source of RAL, and the caesiated hollow cathode source from BINP [71]. Among these, the external antenna DESY RF source, with its high reliability and 150 µs H^- pulses of up to 40 mA current, was already close to the Linac4 requirements as shown in Table 5.1. This source operated without caesium for more than 25,000 hours without degradation, whereas internal antenna sources had an average lifetime of 980 hours [72]. The DESY RF source was felt as a promising candidate, but required improving its performance to meet the Linac4 requirements.

During the commissioning of the DESY RF ion source, it became evident that this source could not fulfil the Linac4 requirements [78]. First of all, the source could not operate with a single stage extraction voltage of 45 kV because of high voltage sparks induced by evaporated material from the electron dump. The H^- production capability of the plasma generator was in addition limited by the RF antenna that started sparking

Table 5.1: Linac4 ion source requirements [20], operational parameters of the DESY [73], SNS [4, 74] and BNL [75] ion sources, and goals of the ion source development program [76]. The design value of the beam energy for the Linac4 ion source was originally 95 keV, but it later changed to 45 keV as a result of a modification of the RFQ design [77]. Vol = Volume, Surf = Surface (caesiated), M-dis = Magnetron discharge. Obtained values are shown in bold.

Parameter	Linac4	DESY	SNS	BNL	IS01	IS02	IS03
Beam energy [keV]	45	35	65	35	**45**	**45**	45
Pulse length [ms]	0.5	0.1	0.5	0.7	**0.5**	**0.5**	**0.5**
Repetition rate [Hz]	2	5	60	7.5	**0.8**, 2	**0.8**, 2	0.8, **2**
H$^-$ current [mA]	80	40	50	90-100	**20**	**40**	**80**
e/H$^-$ ratio		30-50	1	0.5-1	**50**	**5**	**1**
$\varepsilon_{\text{norm,rms}}$ [μm]	0.25	0.25	0.25	0.4	$\sim$ **0.5**	0.25	0.25
H$^-$ production		Vol	Surf	Surf	Vol	Surf	Surf
Plasma heating		RF	RF	M-dis	RF	RF	M-dis

at higher power due to insufficient insulation. Another issue was caused by the amount of co-extracted electrons, which once extrapolated to the Linac4 parameters, would have been too high for the capability of the power converters to deliver enough current. Moreover, the beam size out of the single stage extraction was too big and divergent for the beam pipe of the first solenoid of the LEBT causing important beam losses. These limitations triggered a dedicated ion source development program, which encompassed the investigation of the fundamental processes taking place in negative hydrogen ion source.

Two courses of action were taken for improving the ion source. (1) Creation of a new ion beam extraction system with the goal of reliably extracting and transporting the H$^-$ beam from the DESY plasma generator with an energy of 45 keV. In the meantime the commissioning of the LEBT proceeded with a 45 keV proton beam to optimize the beam matching to the RFQ. The DESY ion source produced this beam by inverting the polarity of the plasma generator. (2) Upgrade of the plasma generator in order to reach higher beam intensities. The proposed upgrade program consisted of three stages, each stage with an increased beam intensity to arrive at the goal of an 80 mA H$^-$ beam current. In this way the commissioning of other accelerator parts of Linac4 could proceed as foreseen with lower intensities. The three plasma generators were:

- IS01 – an upgraded version of the DESY RF-driven source for reaching higher RF-powers based on the study of a high duty factor plasma generator for SPL.
- IS02 – a caesiated version of IS01 for H$^-$ surface production, inspired by the SNS

source.

- IS03 – a magnetron type plasma generator from BNL.

The operational goals of these plasma generators and the performances of the SNS and BNL sources are summarized in Table 5.1. IS01 and IS02 were installed and tested with the same beam extraction system at CERN, and IS03 was first commissioned at the BNL test stand.

In addition to finding inspiration from the above mentioned ion sources; other collaborations were also essential for the ion source development. Despite of different ion beam requirements, the ITER ion source developed at the Max Planck Institute of Plasma Physics (IPP) in Garching, Germany had interesting similarities. This ion source aimed for a long duration (1 h), high current H^- beam (60 A) with no emittance requirement, extracted from a low current density plasma (0.033 A/cm^2) at low pressure (3×10^{-3} mbar) to avoid stripping losses after beam extraction [79]. In order to reach this high beam current, ITER used a multi-aperture extraction grid. In comparison, the Linac4 ion beam had much shorter duration and lower beam current, but needs higher ion current density (0.3 A/cm^2) to respect the emittance requirement, and higher pressure for plasma ignition (order of 10^{-2} mbar [80]). The plasma generators did, however, use similar systems for plasma heating, ITER with 1 MHz RF drivers at the back with a large expansion zone for the plasma, and DESY with a 2 MHz RF coil in front. Because of the power load by the co-extracted electrons on the grids, the ITER ion source was required to keep the e/H^- ratio below 0.5, which is achieved by ceasiation of the plasma generator. To keep the e/H^- ratio within the requirement during the whole pulse, the plasma was monitored using optical emission spectroscopy, which related the H_α, H_β, and H_γ Balmer lines' to the electron and H^- densities in the plasma. This know-how triggered a collaboration for caesium injection techniques, and for an optical emission spectroscopy monitoring system of the Linac4 ion source plasma [81]. Other collaborations included: JYU for the ion beam extraction system [78], RAL for the caesium oven and transport line [82], Keio University, Yokohama, Japan for plasma and collision radiative modelling using a particle-in-cell Monte Carlo collision method [83, 84], and IPP and University Paris-Sud, Orsay, France for simulations of the different states of caesium conditioning [85].

The following section describes the different plasma generators of the upgrade program, starting with the initial copy of the DESY source. Then follows the design of the beam extraction system, which is the main focus of this dissertation. Finally, the LEBT is described to give a complete overview of the ion source together with its diagnostics.

5.1 The DESY 2 MHz RF volume source

Figure 5.1 shows a cross section of the DESY RF ion source. The essential parts of this ion source were: a hydrogen gas feed via a pulsed piezoelectric valve, a high voltage spark gap, a cylindrical shaped Al_2O_3 ceramic plasma chamber with an inner diameter of 48 mm, 2×12 NdFeB magnets forming a dodecapole multi-cusp magnetic field, a 5.5-turn external antenna, 10 NiZn ferrites surrounding the antenna, and 2 NdFeB filter magnets. The extracted H^- ions were accelerated from the source body at -35 kV to the extraction electrode at ground potential over a gap of 6.5 mm. For an H^- beam energy of 45 keV the extraction gap was increased to 8.5 mm to obtain the same nominal electric field. A magnetic spectrometer separated the electrons from the H^- beam after the extraction.

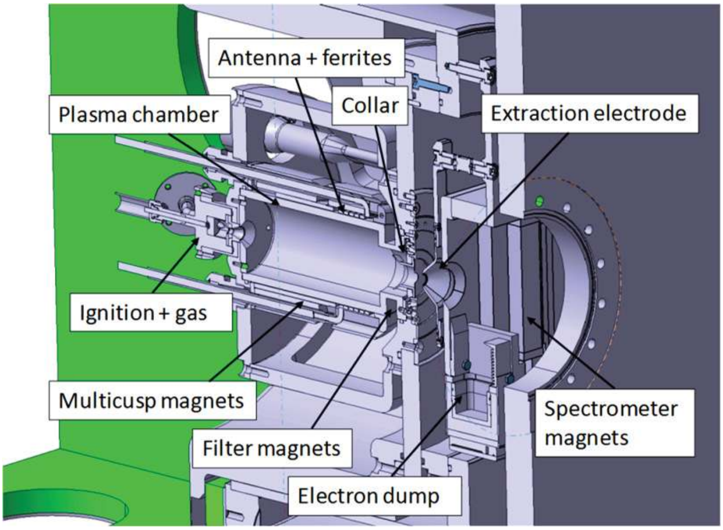

Figure 5.1: Cross section of the DESY source with the first version of 45 keV extraction and electron dumping at full energy, as installed at CERN in 2009.

The ion source operated in pulsed mode, and the plasma was on only when the beam was required in order to not overheat the plasma generator. The plasma generator itself was constantly held at high voltage (-35 kV or -45 kV), backed up by a 2 μF capacitor. The capacitor stored sufficient charge to allow the H^- and electron current to be accelerated out of the source, while keeping the source potential variation within 500 V.

The hydrogen gas was pulsed through a piezoelectric valve and in this way the vacuum was maintained at 10^{-6} mbar in the ion source and LEBT. Good vacuum conditions were needed to reduce beam losses from interactions with the rest gas, and also to reduce the risk of high voltage sparks across the extraction gap. The RF plasma ignition was assisted by an ignition source located in the gas line: before reaching the plasma chamber, the hydrogen gas entered a small volume where the pressure was locally increased. Here, a precisely timed ignition voltage of 600 V to 800 V created a discharge of a few amperes between an anode and a cathode element, and the electrons liberated in this spark entered the plasma chamber and assisted the plasma ignition.

The multi-cusp magnetic field configuration confined the plasma in the Al_2O_3 plasma chamber. RF heating was used, and the antenna itself was surrounded by ferrites that guided the magnetic field lines to improve the RF-coupling with the plasma. The magnetic filter field was located between the antenna and the extraction gap, and separated the plasma into two regions: one with hot electrons at the position of the RF antenna and one with cold electrons close to the extraction gap. The penetration of this magnetic field into the extraction region could affect the beam extraction and make the beam leave the plasma with an angle. This effect was corrected by tilting the collar electrode with an angle up to 3° in the plane perpendicular to the beam direction.

Negative ions and electrons were extracted from the plasma by a cone shaped puller electrode at ground potential. The puller was mounted on an eccentric ring that could be moved to correct for a beam displacement caused by the magnetic filter field and the collar electrode tilt. The 6.5 mm diameter puller aperture could then be displaced up to 3.5 mm from the centre. After the beam extraction, the electrons were deflected by a dipole magnet made from a pair of permanent SmCo magnets, and dumped in an electrically insulated graphite block that could measure the electron current. A second dipole pair corrected for the deviation of the H^- beam path.

5.1.1 Commissioning of a 35 keV H^- beam

The RF-driven ion source was at first commissioned with an extraction voltage of 35 kV, which was the operational value used at DESY. The operation was a success, and the ion source performance came close to the operational achievements at DESY with a stable H^- ion beam current of 23 mA during 500 µs at a repetition rate of 0.83 Hz, and within a normalized rms emittance of 0.26 µm [86]. Figure 5.2 shows eight traces of parameters that show the different steps for the creation of one H^- beam pulse. The piezoelectric valve was driven with a 0.5 ms sinusoidal shaped voltage pulse (1). A 40 µs ignition pulse (2) followed 0.635 ms after the valve voltage pulse, and created a discharge (3) and spark (4) in the ignition element. Then, the RF coupled with the plasma 0.2 ms after the ignition, as shown by the reflected RF-power (5) and the plasma light (6). An electron current of about 1 A hitting the electron dump was measured (7) and the H$^-$ beam had an intensity of 23 mA measured in a Faraday cup (8) with a beam length of 0.5 ms. The ion source also showed excellent short term stability as shown in Figure 5.3, where 100 consecutive waveforms of the beam current in the Faraday cup are plotted. Long-term stability was not measured since the ion source was switched off during nights and weekends for general safety.

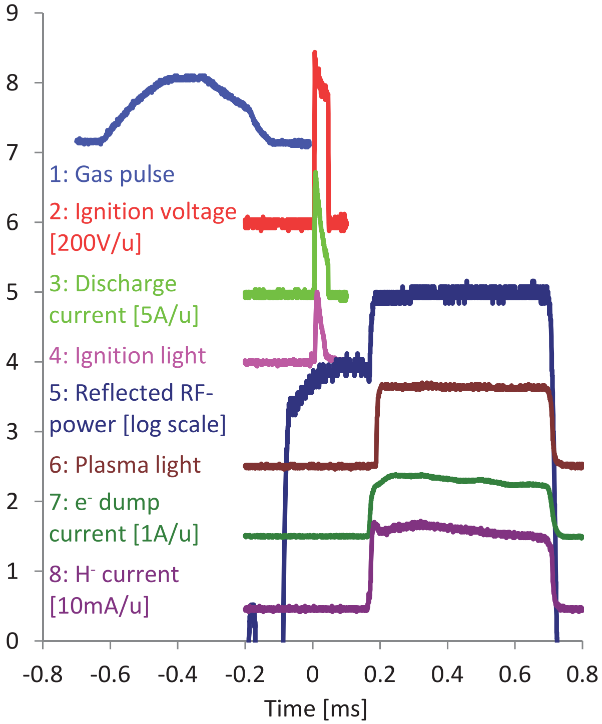

Figure 5.2: Plot of gas injection, ignition voltage and discharge current, reflected RF-power, and H$^-$ and electron beam. Baselines are offset.

Even though the commissioning at 35 kV was initially successful, the ion source could not reach the Linac4 requirements. The major constraint was the increased extraction voltage of 45 kV. Already at 35 kV, there were frequent high voltage breakdowns stopping the beam (about 15 per 24 hours). This was believed to be a problem of high

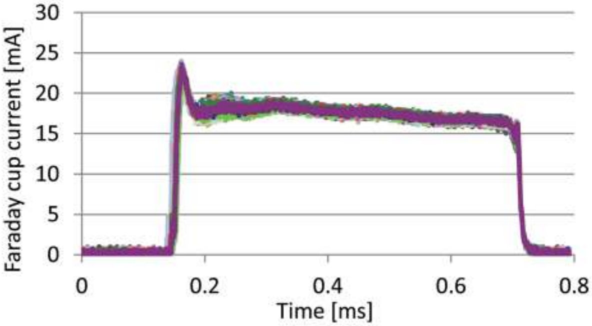

Figure 5.3: DESY source stability over 100 beam pulses.

voltage training. However, when the voltage was increased to 45 kV, it was impossible to run the source for more than a few pulses before the high voltage broke down. In addition to this problem, the ion source was still far from the Linac4 H^- beam current requirement of 80 mA. These limitations led to a dedicated ion source development program. However, the DESY plasma generator was still used with a new beam extraction system for the commissioning of the 3 MeV RFQ [87].

5.1.2 Limitations of the DESY ion source

During the commissioning of the DESY RF-driven ion source, several weaknesses were discovered. The most critical issue was that the source could not deliver a 45 keV beam, a requirement that had to be fulfilled for a correct matching to the RFQ. This section presents the limitations of the ion source performance.

The ion production was too low

The H^- beam current requirement of Linac4 is 80 mA. The DESY plasma generator could deliver a stable beam of 23 mA, and the maximum current that was observed was 30 mA. The e/H^- ratio during the commissioning was in the order of 50-100. Figure 5.4 shows the measured H^- and electron currents as a function of the RF-heating power delivered to the plasma (forward RF-power). The maximum power reached was 60 kW, and the coupling factor, calculated as the difference of forward and reflected RF-power, was 60-70 %. Above 60 kW, the ion beam measurement became unstable. The two points in the top right corner of the figure represent the H^- current goal of 80 mA with an expected co-extracted electron current of 5 A. These currents are plotted at the maximum available RF-power of 100 kW, and show that reaching the Linac4 beam intensity requirement was not realistic with the DESY plasma generator.

Running the ion source with parameters extrapolated to nominal beam and 100 kW of RF-power would be difficult because of the following reasons: (1) the capacitor would have to be changed to store the energy at 45 kV when drawing 5 A of current, (2) the electron beam power would reach 225 kW and cause great damage to the electron dump, and (3) the emittance growth of the H$^-$ beam would be increased due to the co-extracted electrons, causing reduced beam quality and possible beam losses.

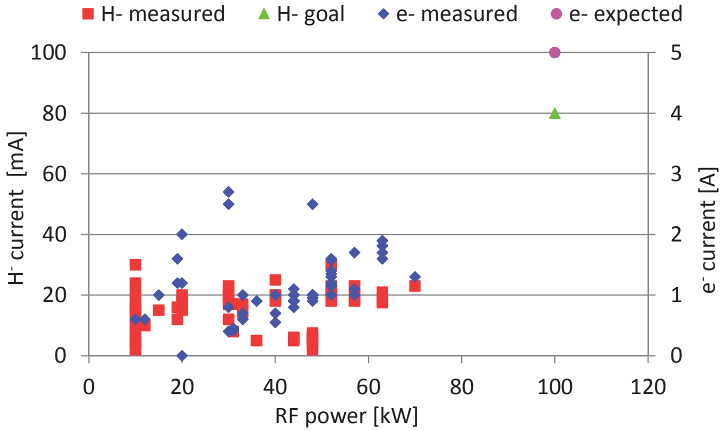

Figure 5.4: Measurements of H$^-$ and electron current as a function of the RF-power delivered to the plasma (forward RF-power). The two points in the top right corner show the expected electron current and the goal of 80 mA H$^-$ beam current with the DESY source. These currents are estimated with the maximum available RF-power of 100 kW.

The RF antenna did not resist high power

The DESY ion source has an external RF antenna for heating the plasma. The coupling factor to the plasma is reduced compared with an internal antenna, but the idea is to avoid sputtering of the antenna insulation by the plasma. Internal antenna sources need to change the antenna on a regular basis because of antenna failures, whereas external antennas can run for thousands of hours without problems.

The DESY ion source was running for most of the time with an RF-power of 20-40 kW. However, after running the source with 60 kW, the antenna started sparking. Furthermore, the maximum power that could be applied without sparking reduced slowly to 20 kW before the antenna inspection. The inspection showed that the air ionization from the antenna sparks had burned the Kapton foil and dug a groove in the Delrin insulation around the antenna, as shown in Figure 5.5. This weakness of the antenna was considered when upgrading the plasma generator.

Recent studies at SNS have, however, concluded that most internal antenna failures come as a result of defects on the antenna insulation before installation. With careful inspection of the antennas, the lifetime can be drastically increased. Since SNS has implemented these antenna inspections, they have experienced no ion source failures because of the antenna [88].

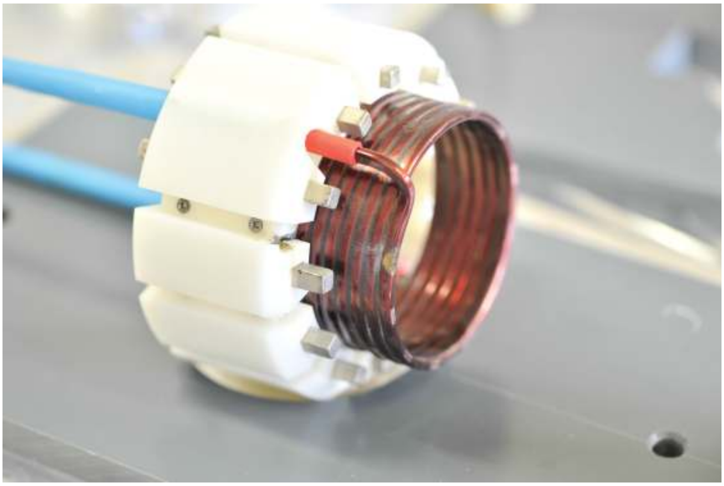

Figure 5.5: RF-sparks penetrated the Kapton insulation of the antenna and dug a groove in the Delrin insulation.

The dumping of electrons caused high voltage breakdowns

When running the DESY source with an extraction voltage of 45 kV, it was not possible to hold the voltage over the extraction gap for more than a few beam pulses. The inspection of the electron dump showed great damage on the graphite surface from the electron beam impact, and it was concluded that the evaporated material caused the high voltage breakdowns. The electron dump damage was already observed when operating at 35 kV, and was probably the cause of the less frequent high voltage breakdowns at that voltage. An observation that supports this theory is shown in Figure 5.6, where the breakdown time is plotted versus the number of beam pulses before a breakdown. The plot shows that the breakdowns always occurred 0-300 ms after the beam pulse. In the case of a spark triggered by the beam hitting the puller electrode, the breakdown would be during the beam pulse, which was not observed. Here the spark was delayed by the time it took for the dump material to travel to the extraction gap.

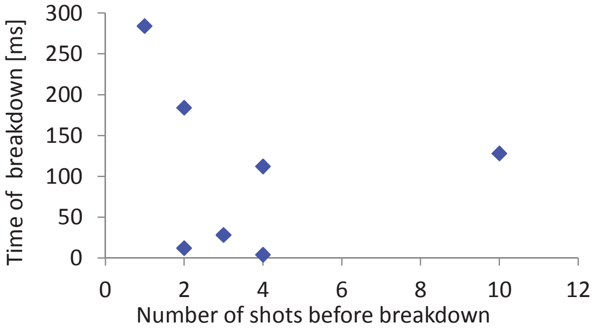

Figure 5.6: The high voltage breakdowns occurred from 0 to 300 ms after the beam pulse. The source could not run for more than 10 beam pulses before a breakdown.

Another verification came during the commissioning of the RFQ with a 45 keV proton beam. The beam was produced by the same source by inverting the polarity of the extraction voltage. During these proton beam tests, the high voltage breakdown rate was reduced to approximately 1 per 24 hours. This observation was also consistent with the co-extracted electron beam being the cause of the high voltage breakdowns, and not because of the ion beam hitting the puller electrode.

The first attempt to solve this issue was to change the electron dump material. In addition to the original graphite dump, titanium and tungsten were tested. Figure 5.7 show the three different electron dumps that were used, all showing signs of removed material from the surface by the electron beam.

The effect of the electron beam on the dump surface was analysed by transient thermal simulations made with ANSYS [89]. These simulations concluded that for a pulse length of 0.6 ms, the maximum allowed power density before melting or sublimation of a graphite surface was 0.9 kW/mm^2. The values for titanium and tungsten were

(a) Graphite dump after commissioning at 35 keV.

(b) Titanium dump. 500 electron beam pulses at 45 keV.

(c) Tungsten dump. 100 electron beam pulses at 45 keV.

Figure 5.7: Three different electron dump materials were tested, all showing signs of impact by the electron beam. The beam came from the left and a magnetic dipole field bent the electrons. The groove in the graphite cup going from the centre of the cup towards the left came from the ramp-up of the beam energy from 0-35 keV during the commissioning. With lower energy, the magnetic field had a larger influence, and the electron beam was bent back towards the source.

0.4 kW/mm^2 and 2.0 kW/mm^2, respectively. Figure 5.8 shows the simulated surface power densities from a 1.5 A electron beam at two different beam energies. The maximum values reached were 1.8 kW/mm^2 for 35 keV and 3.0 kW/mm^2 for 45 keV, consistent with the thermal simulations and the state of the electron dumps after use.

One solution for this issue could be to lower the energy of the impacting electrons by applying a negative voltage to the dump. The approach would, however, be difficult to implement because of the lack of space in the beam extraction design. The required bias of the electron dump would have to be at least 10 kV to arrive at the same conditions as for the 35 keV beam, and even then, the high voltage would break down about 15 times per 24 hours. In addition, with the goal of having an H$^-$ beam current of 80 mA, the electron current would also increase proportionally as well as the power density on the electron dump.

The resulting conclusion was therefore to completely redesign the beam extraction system, which is described in Section 5.3.

Issues with the capacitively stored energy

The high voltage system used a 2 μF capacitor to store the energy from which the beam charge was drawn, as illustrated in Figure 5.9(a). The plasma generator was kept at a constant voltage and the ion beam was extracted when the plasma was ignited. A 300 Ω

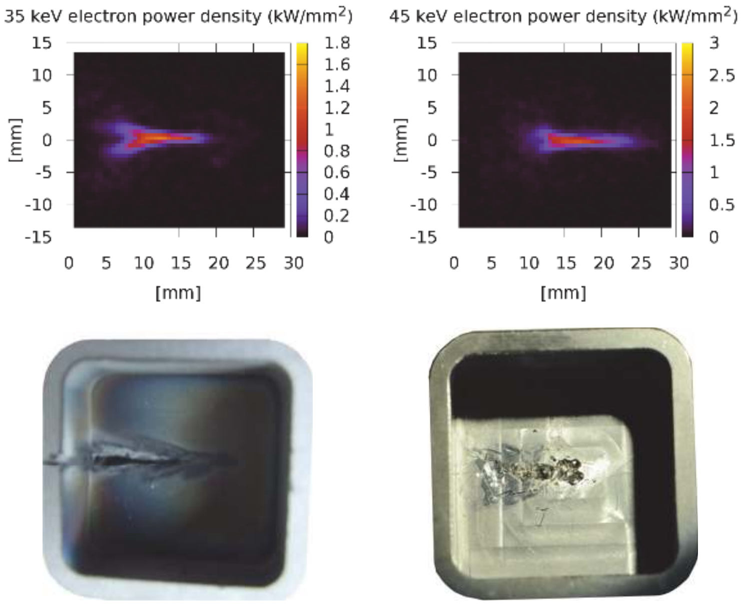

Figure 5.8: Comparison between photos of the graphite (left) and titanium (right) electron dump, used with beam energies of 35 keV and 45 keV, respectively. Above are shown IBSimu simulations of the surface power density from a 1.5 A electron beam. Both show surface power densities that would sublimate the dump surface for a duration of 0.6 ms.

resistor between the capacitor and plasma generator worked as a current limitation in case of high voltage breakdowns.

With this type of high voltage system, there was a sudden reduction of the plasma generator voltage as soon as the plasma ignited and the beam current was drawn through the 300 Ω resistor. Then followed a constant voltage droop due to the discharge of the capacitor. After the plasma was switched off and the current stopped, the voltage of the plasma generator came immediately back to the reduced capacitor potential. The blue trace in Figure 5.9(b) illustrated this behaviour of the high voltage system for a total beam current of about 2.5 A (purple trace).

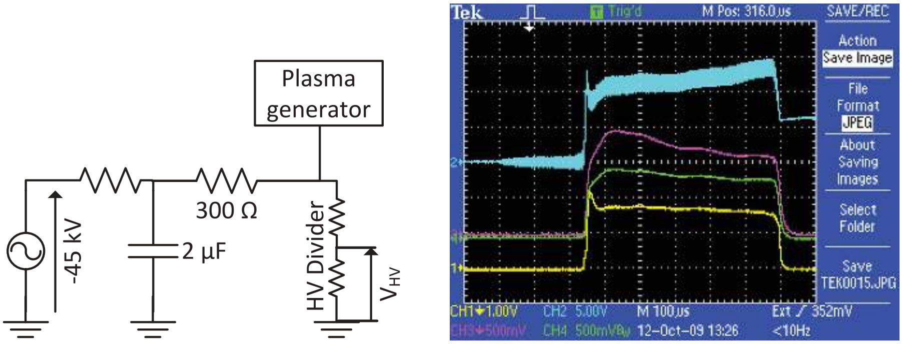

(a) High voltage system with a capacitor to store the beam energy. The plasma generator voltage was measured with a high voltage divider.

(b) High voltage drop during beam extraction. Faraday cup current (yellow, 10 mA/div), plasma generator voltage (blue, 500 V/div), plasma generator current (purple, 1 A/div), and electron dump current (green, 1 A/div).

Figure 5.9: High voltage system of the DESY source, and voltage drop during beam extraction.

When running the source with this type of high voltage system, one typically applies a higher voltage to the plasma generator to compensate for the first reduction. However, the voltage drop during the beam causes a dispersion of the beam energy. In order to stay within the RFQ tolerance of 1 %, the maximum allowed voltage change is only 450 V. The maximum current that can be pulled from the plasma generator during 500 µs is then equal to: (450 V * 2 µF) / 500 µs = 1.8 A. With maximum expected currents of 5 A, the capacitor to store the charge have to be increased, or a new type of high voltage system needs to be implemented. Another drawback of this capacitively backed high voltage systems is that when a high voltage breakdown occurs, a significant amount of the stored energy will go into this spark and can cause damage to the electrodes.

In addition, the investigation of the 45 kV high voltage breakdowns revealed that these breakdowns occurred after beam pulse, as shown in Figure 5.6. These breakdowns could then in principle be avoided if the high voltage was switched off at this time.

In order to avoid these problems for the future beam extraction system, pulsed high voltage power converters were designed [90].

5.2 Plasma generator upgrades

To address the issues identified in the previous section and then to increase the H$^-$ current in the Linac4 H$^-$ ion source, the plasma generator and the beam optics needed to be improved. The development program for the plasma generator was a three-stage improvement of the beam intensity, and in this way being able to deliver a 45 keV beam for the commissioning of the downstream parts of Linac4.

5.2.1 IS01: high power upgrade of the DESY plasma generator

IS01 is an upgraded version of the DESY plasma generator with the goal of producing a 20 mA H$^-$ beam. Many of the features are inherited from the study of the high duty factor plasma generator for CERN's SPL [91, 76]. The major difference between the DESY plasma generator and IS01, is the antenna that has better insulation to allow a higher RF-power, as shown in Figure 5.10. The antenna can also be replaced with versions having between 3 and 6 turns. Because of the larger antenna diameter, the cusp magnets have been moved outwards and replaced by a stronger octopole field made by Hallbach elements (Figure 5.11). Another novelty is a simpler Al_2O_3 cylinder to replace the complex shape of the old plasma chamber with the filter field magnets on the inside. The magnets are Nickel coated to protect the rare earth material (NdFeB) form reacting with the hydrogen gas [92]. The collar electrode has also been replaced by a more solid design without the tilting capability that added complexity. Aligning the extraction system instead now compensates any beam offset.

IS01 beam results

IS01 was first tested in December 2012 with a 6-turn antenna, and the beam extraction system described in Section 5.3. Figure 5.12 shows the first results with a 10 µs, 1 mA signal measured in the Faraday cup, and less than 0.1 mA during the remaining 0.4 ms of the plasma pulse.

The following modifications were made after the first test to produce more H$^-$ ions:

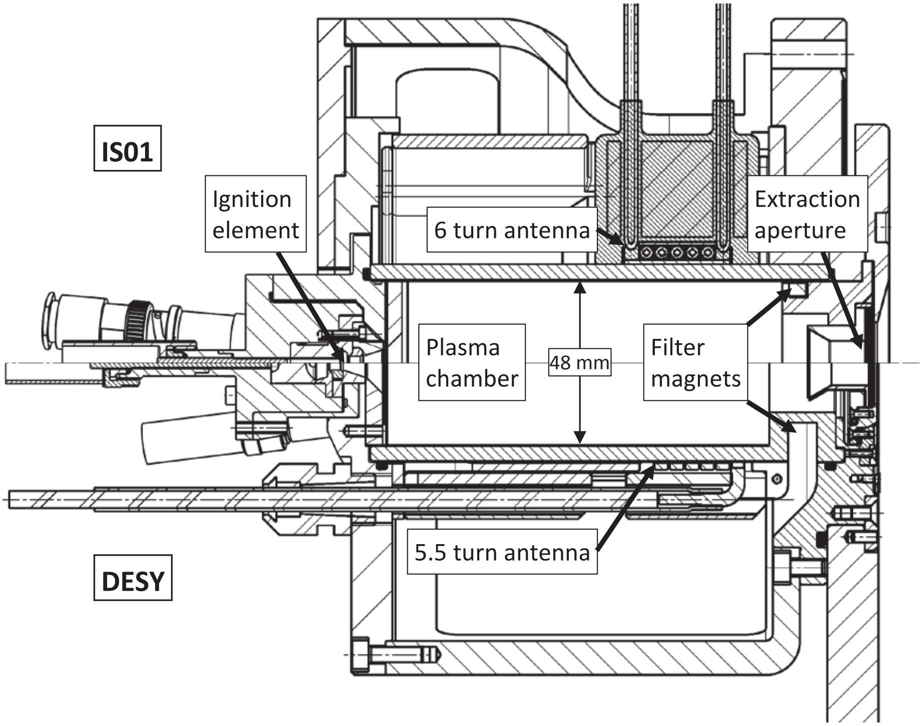

Figure 5.10: Comparison between IS01 (top) and the DESY plasma generator (bottom). The major difference in IS01 is the RF antenna with better insulation, here represented with 6 turns. The DESY antenna had 5.5 turns.

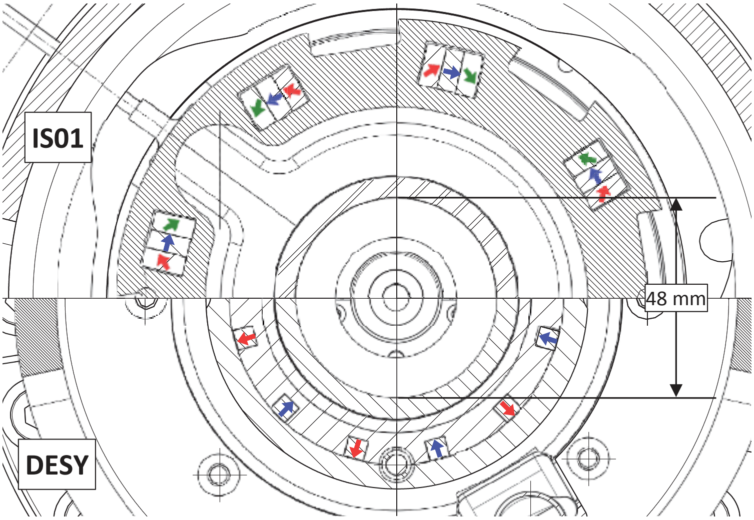

Figure 5.11: Cusp magnets configuration of IS01 (top) and the DESY plasma generator (bottom). The magnetization direction of the magnets is indicated with coloured arrows. DESY used a dodecapole cusp field, whereas IS01 had an octopole field made by Hallbach elements.

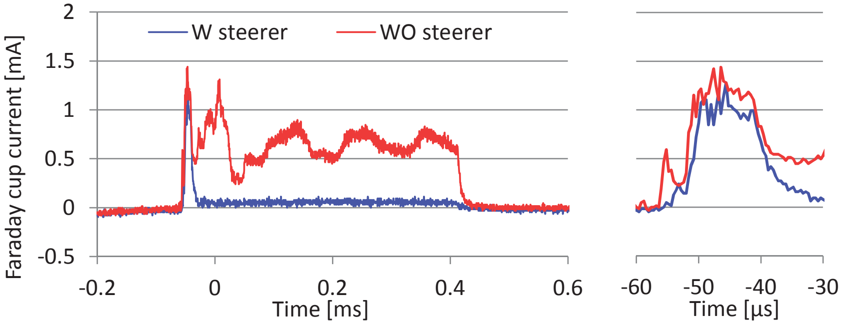

Figure 5.12: First negative ions observed from IS01. To the left is shown the whole Faraday cup signal with steerer in blue and without in red. To the right is a zoom of the first peak of the signal. The 10 µs peak is the 1 mA H^- beam, the remaining signal without steerer are electrons.

- Installation of an additional pair of filter field magnets to increase the magnetic field strength. However, this modification did not change the results.

- Exchange of filter field magnet holder material (AlN) with Macor that contains 10 % of potassium (K_2O). Macor was at this point not present in the plasma generator, but the DESY plasma generator contained this material. The theory was that the potassium could be sputtered off by the plasma and be deposited on the collar. The collar work function would then be lowered as it would for caesium deposition and become a source of surface produced H^- ions. Changing this material, however, did also not have any positive effect.

- Change of the polarity of the antenna. One of the antenna poles is connected to the plasma generator potential, so the electric field on this side will be much less than on the "high voltage" end. Initially the plasma generator potential side was closest to the extraction aperture to avoid heating electrons in this region that could destroy the H^- ions. Reversing the antenna potential, however, resulted in an electron current of tens of amperes that could not be supported by the high voltage power converters.

One explanation of IS01's malfunction was that the plasma was heated too much by the new 6-turn antenna. After 10 µs, electrons had then gained enough energy to destroy the H^- ions in the extraction region despite the magnetic filter field. The RF-power was lowered to the minimum necessary for creating a plasma, but still no H^- ions were produced. In order to be on schedule with the Linac4 commissioning, the DESY plasma generator was therefore installed with the new extraction system and succeeded in producing a 45 keV H^- beam. The IS01 development was thus put on hold, while the source was used for the commissioning of the extraction system and the LEBT. When IS01 was reinstalled with a 4-turn antenna, it succeeded in producing a 2 mA H^- ion beam with an e/H^- ratio of about 200. During one month of conditioning, the beam current gradually increased to 15 mA, and the e/H^- ratio reduced to 70. This achievement was, however, not sufficient to replace the DESY plasma generator for the commissioning of Linac4 at low beam current.

5.2.2 IS02: caesiated surface production RF plasma generator

A model of IS02 is shown in Figure 5.13 [76]. A new feature of IS02 is that there is no longer any ignition element. Both the DESY plasma generator and IS01 managed to create a capacitive discharge without the ignition element, therefore this part is removed from the design to make room for a central view port and the caesium injection. The H_2 is directly injected into the plasma chamber from the side. A 45° conical shaped molybdenum *converter* replaced the collar electrode. By depositing a thin layer of caesium on this part, the work function of the material will be lowered sufficiently for surface production of H$^-$ ions, as described in Section 3.3.2. The external part of the converter facing the puller electrode has a 65° angle for better shaping of the electric potential lines for the beam extraction. Similar to IS01, IS02 can operate with antennas with different number of turns.

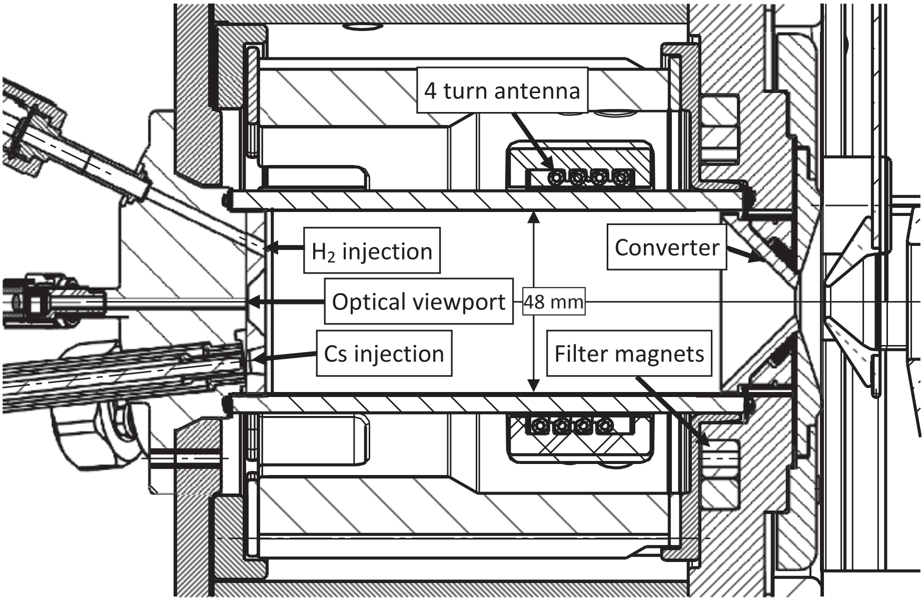

Figure 5.13: IS02 plasma generator. The filter magnets are moved outside the plasma chamber, and the first prototype was installed with a 4-turn antenna.

H$^-$ beam with a four-turn antenna IS02

IS02 was installed with a 4-turn antenna in November 2013. At first it was operated without caesium in order to see whether it could produce H$^-$ ions in volume mode, as predicted by [93]. The first tests were positive with H$^-$ beam currents yielding 30 mA with 30 kW RF-power, represented by the blue trace in Figure 5.14. The total current extracted from the plasma generator is plotted with a dotted line, and the e/H^- ratio was approximately 16.

The commissioning proceeded in December 2013 by depositing a 100 Å layer of caesium on the converter for enhanced H^- surface production near the extraction aperture. The caesium was injected by vaporization from the external oven, with the amount of caesium deposition estimated from measurements on a test set-up with a quartz microbalance. After caesiation, the H^- beam current reached 60 mA with 90 kW RF-power (red trace in Figure 5.14), and the e/H^- ratio was reduced to 1.6. After one month of operation, the ion source performance came back gradually to the values before caesiation.

Standard procedure for caesiated ion sources could be to re-caesiate several times during one ion beam run, or to have a constant flow of caesium injected during operation. IS02 will be tested with both modes of caesium injection to find the optimum for a stable high current H^- beam.

5.2.3 IS03: magnetron type ion source

IS03 is a magnetron plasma generator with a design copied from the ion source at BNL [76]. In this type of ion source, a discharge between the central cathode and the surrounding anode creates the hydrogen and caesium vapour plasma. The H^- ions are produced on the surface of the caesiated molybdenum cathode, and extracted through a hole in the anode. The layout of the magnetron source is shown in Figure 5.15.

Caesium is continuously injected during operation, and the hydrogen gas is pulsed by a custom made electromagnetic valve. A magnetic dipole field prevents the electrons from travelling directly to the anode, and additionally, they make an E×B drift motion leading to an increased path length. Collision processes allow electron migration to the anode. The magnetic dipole field is also used to deflect the co-extracted electrons and dump them on the puller of the single stage extraction system.

First test at BNL

The parts for the magnetron ion source were built at CERN. Since the auxiliary hardware was not in place at CERN, the plasma generator was shipped to BNL for the first beam tests in October 2013. Two tests were performed: one with the operational repetition rate at BNL of 6.6 Hz, and a second with 2 Hz as required at Linac4. The results are shown in Figure 5.16 together with the achievements of the BNL ion source from 2002. The extracted beam currents as a function of the extraction voltage had similar shapes

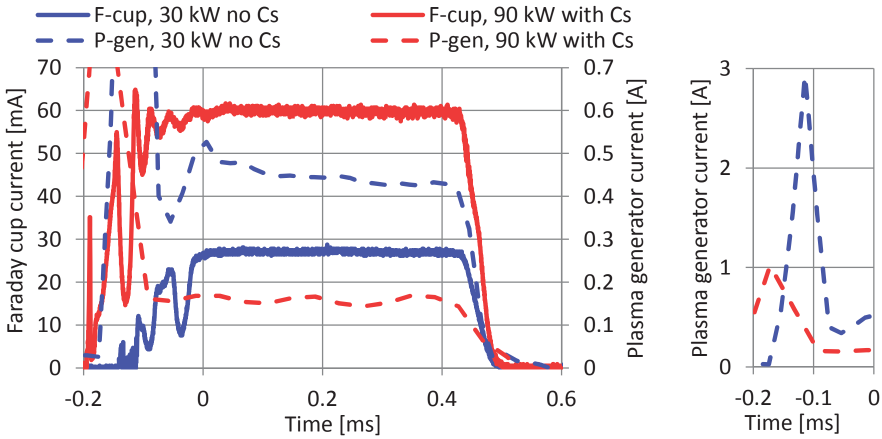

(a) IS02 measured Faraday cup (H^-), and plasma generator current ($H^- + e^-$). The plasma generator traces have been averaged to eliminate 2 MHz RF induced noise.

(b) Zoom of plasma generator current during plasma ignition.

Figure 5.14: (a) H^- beam current and total plasma generator current measured with IS02 before (blue) and after (red) caesiation. The RF-power was optimized for having a stable high current H^- beam. (b) The plasma ignition by capacitive discharge creates a high current electron peak at the start of the beam pulse. The peak disappears when the coupling mode changes to inductive.

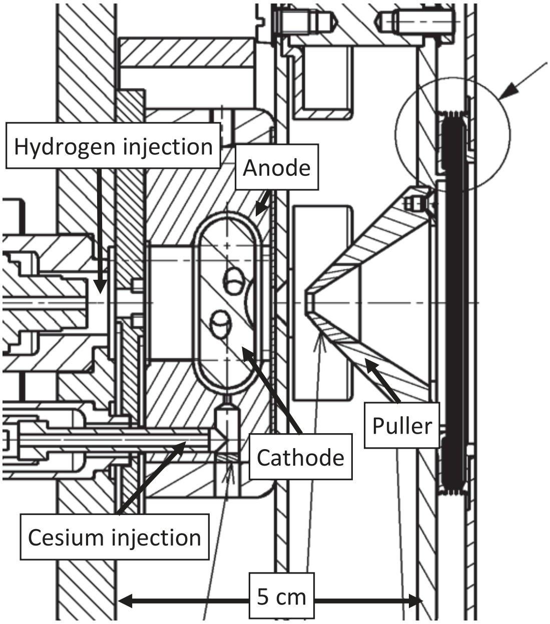

Figure 5.15: Magnetron ion source. A discharge between the inner cathode and surrounding anode heats the plasma. The co-extracted electrons are dumped directly on the puller, deflected by the perpendicular magnetic dipole field that is used for confining the plasma around the cathode.

for the three cases, and a maximum intensity of 135 mA H^- could be demonstrated. The power converters limited the extraction voltage to 40 kV.

These results are promising for the operation in Linac4, but there still remains to be a demonstrated beam of the required energy of 45 keV. Because of the low co-extracted electron current (e/H^- = 0.5-1), this beam extraction worked up to 40 kV. However, signs of wear were observed after the few days of testing. A new beam extraction needs to be designed for this system to ensure the stability and emittance quality of the beam.

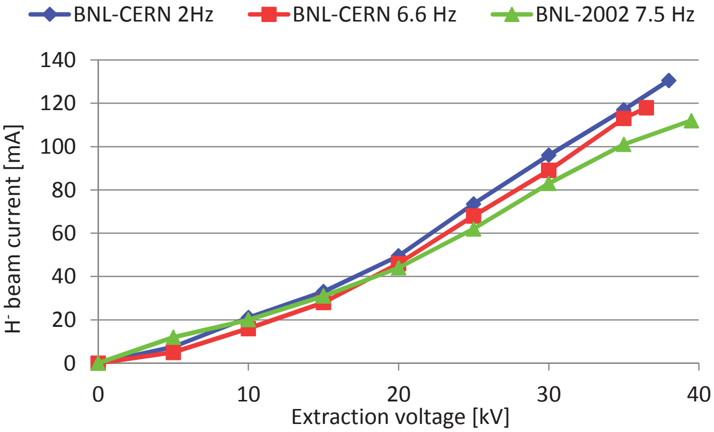

Figure 5.16: Results of the magnetron ion source test at BNL. The beam current increased as a function of the extraction voltage, and a maximum H^- current of 135 mA was reached.

5.3 A new extraction system for a high current H^- beam

After the DESY ion source could not be commissioned at 45 kV, the design of a new ion beam extraction system started with the following goals:

1. Extract and transport an H^- ion beam with an energy of 45 keV.

2. For a volume production ion source (IS01) with an estimated e/H^- ratio of 50: extract and transport 20 mA of H^- within a normalized rms emittance of 0.5 µm.

3. For a surface production ion source (IS02) with an estimated e/H^- ratio of 5: extract and transport 40 mA of H^- within a normalized rms emittance of 0.5 μm.

4. Correct for the deflection of the H^- beam that occurs when dumping the electrons.

5. Be flexible for different plasma conditions that might change the H^- beam current and emittance, and the e/H^- ratio.

6. For each case, keep the electron beam power density on the electron dump surface below 1 kW/mm^2.

7. By inverting the polarity of the extraction electrodes, extract and transport an 80 mA proton beam for RFQ commissioning with higher beam current.

This section presents the new extraction system that has been designed with IBSimu. The section starts with the simulation input and output parameters, and a verification of the simulation output compared with the experimental results from the DESY ion source commissioning. Then follows a description of the beam extraction system with the first experimental results.

5.3.1 Input parameters of the simulations

The simulation method of IBSimu was introduced in Section 4.4.1. Below are listed some of the most important input and output parameters used in the IBSimu simulations:

Co-ordinate system The simulations are made in a normal right handed Cartesian co-ordinate system. The z-axis is the beam direction with a vertical x-axis and horizontal y-axis. The reason for swapping the x- and y-axis compared with the traditional choice is to have the following positive directions of the beam: forward for the accelerating direction, and upward and to the right for vertical and horizontal movements, respectively. A simulation output image is shown in Figure 5.17.

Mesh size IBSimu uses a cubic mesh. For the simulations it is important to find the mesh size that is fine enough to give a correct output, and coarse enough to speed up the simulation time and avoid memory allocation problems. Figure 5.18 shows the simulated horizontal and vertical emittance of the DESY ion source as a function of the mesh size used with IBSimu. At 0.5 mm the result is starting to converge, and below 0.3 mm, the simulation failed because of memory allocation error. 0.5 mm mesh size was used for the new extraction system design.

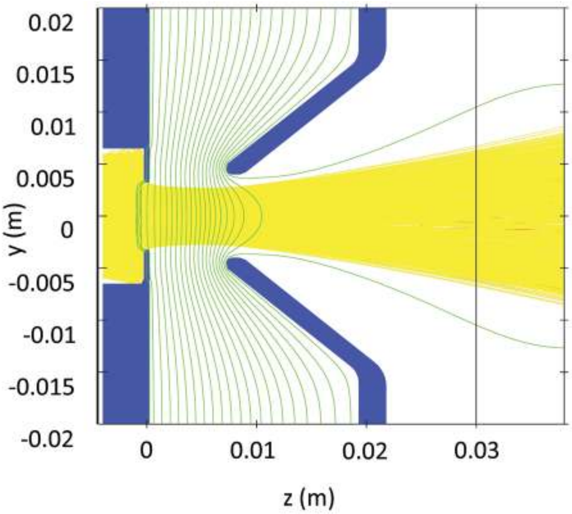

Figure 5.17: Simulation output for testing input parameters. This picture shows the horizontal (y) plane where the positive direction (up) is towards the right in reality. The beam comparisons have been made at 30 mm (black line).

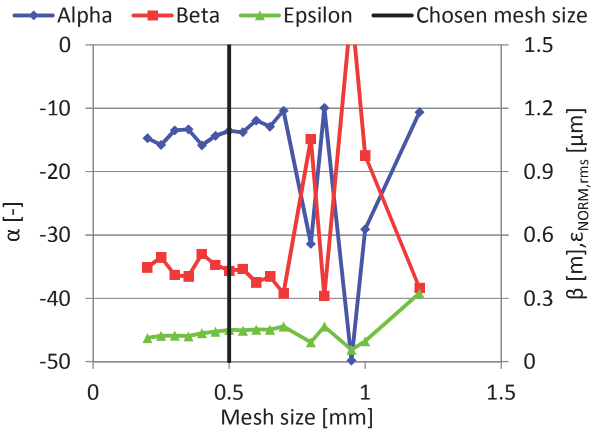

Figure 5.18: Twiss parameters alpha and beta, and emittance as a function of the mesh size.

Particle trajectory number The simulated beam current is distributed over a number of particle trajectories. The higher the number, the more precise the simulations. Between 50,000 and 100,000 trajectories, or 125-250 trajectories per square mesh, have typically been used for each particle type of the simulation.

Iterations of beam-induced space charge As shown in the flowchart in Figure 4.21, the simulations follow an iterative process. In the first iteration, the electrostatic field is calculated, then the particles are tracked through this field, and the space charge from the beam is added to the potential distribution. In the second iteration, the E-field is recalculated including the beam space charge, and the particles are again tracked through the converged solution of the E-field. This process continues for as many iterations as specified by the user. Figure 5.19 shows the emittance output from the simulation of the DESY source as a function of the number of iterations. For the new extraction system design, 30 iterations have been used, but this number could have been reduced as shown in the figure.

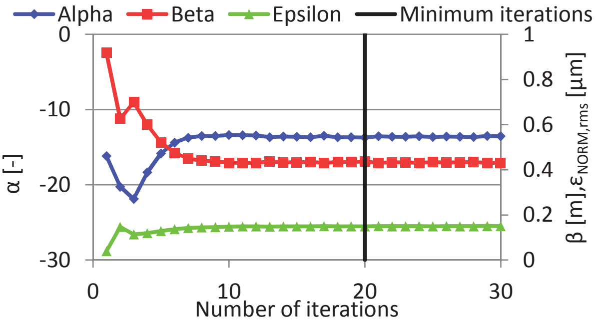

Figure 5.19: Twiss parameters alpha and beta, and emittance as a function of the number of iterations.

Particle energy and plasma temperature The particles are given an input energy in the direction of the extraction to initialize their velocity until they are accelerated by the extraction field. Transverse and parallel temperatures are also given to the plasma model. The influence of these parameters is shown in Figure 5.20. For the simulations, 5 eV has been used as input energy, and 0.5 eV and 0 eV have been used for the transverse and parallel temperature, respectively.

Plasma parameters The method for modelling the ion plasma was described in Sec-

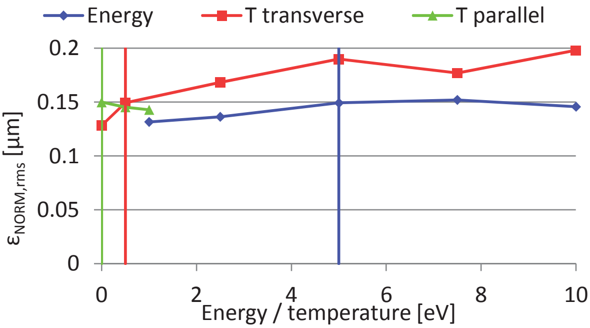

Figure 5.20: Influence of energy and transverse temperature for IBSimu simulations.

tion 4.4.2. For negative beam extracitons, the plasma potential has been fixed to 0 V, and the B-field suppression threshold voltage has been set to 10 V. Further, the user specifies the space charge densities and energies of the fast ions (ρ_{f0} and E_f) and the thermally trapped ions (ρ_{th0} and E_{th}). For all simulations $\rho_{f0} = \rho_{th0} = 0.5 \times \rho_{neg0}$, $E_f = 7.5$ eV, and $E_{th} = 1$ eV. ρ_{neg0} depends on the user input current densities of negative ions and electrons, and is calculated in the code after the first iteration.

5.3.2 Output from the simulations

Since the users program the IBSimu simulations themselves, the users can freely choose which output they desire. The database of particle trajectories can be stored for post-processing, or the information about the beam can be extracted at a plane for integration into another particle tracking code such as PATH [94]. Here are listed the most common outputs used in this dissertation:

Beam current The beam current extracted from the plasma generator, and the currents hitting all electrodes of the extraction system are stored. These currents are compared with the measured beam currents, and enables an overview of where each of the charged particles species (e.g. H⁻ ions, electrons, secondary electrons) have been measured.

Transverse beam profile IBSimu can store the beam profile from any plane. The most interesting is the plane perpendicular to the beam axis to compare with measurements of the transverse beam phase space. IBSimu calculates the rms emittance, the twiss parameters, average beam positions, and average beam angles.

Surface density IBSimu can calculate the surface power density of a beam impinging on a surface. This feature has been particularly useful for the design of the electron dump, in which the high power electron beam of the DESY single stage extraction system vaporized the material.

5.3.3 Simulations of the single stage extraction system of DESY

The first step was to simulate the single stage beam extraction of the DESY ion source. The simulation results were then compared with the measurements from the 35 keV commissioning, and used to benchmark the code and to understand the beam extraction dynamics. The electron beam power density calculations of the electron dump described in Section 5.1.2 were also output from this IBSimu model of the H$^-$ beam extraction.

The simulation output is shown in Figure 5.21. Because the collar electrode of the DESY plasma generator was tilted, and the simulations require a straight plasma aperture, the extraction geometry has been tilted instead. In the particle density plot we observe the high-density electron beam that is being deviated into the electron dump. In the particle trajectory plot, we can see that the H$^-$ beam is quite divergent out of the source and slightly offset with respect to the beam axis. Figure 5.22 shows a comparison between the measured and simulated beam projections of the horizontal and vertical position and angle. The profiles have a good resemblance, however, the horizontal offset is inverted. These measurements were performed in the early commissioning stage of the emittance meter, and it is possible that the horizontal axis was inverted at this stage.

5.3.4 Choice of extraction system type

Two types of extraction systems were considered for the Linac4 H$^-$ ion source [78]. In the first option, the electrons were dumped in a magnetized Einzel electron dump (Figure 5.23(a)), which had the advantage of tuning the puller voltage to optimize the plasma meniscus shape. It also corrected for the beam offset induced by the magnetic field of the electron dump by a puller tilt and/or offset. In the second extraction system, the electrons were dumped on a puller at low voltage (Figure 5.23(b)). With this early electron dumping, the emittance growth from the electrons would be reduced.

In terms of beam transport and emittance, the two systems showed similar performances. In the end, the extraction system with the magnetized Einzel electron dump

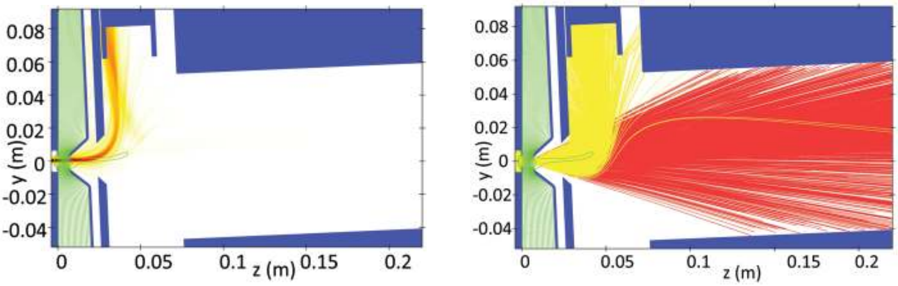

(a) Particle density plot. Red indicates higher density.

(b) Particle trajectory plot. H^- ions are in red and electrons in yellow.

Figure 5.21: Simulation of the DESY RF ion source beam extraction.

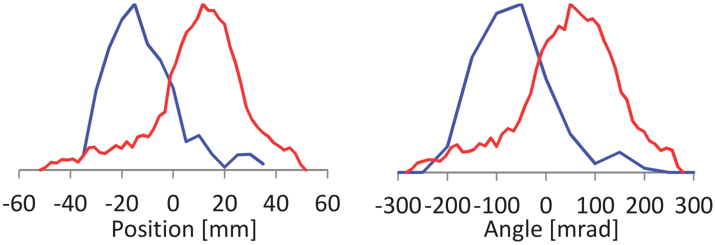

(a) Horizontal position

(b) Horizontal angle

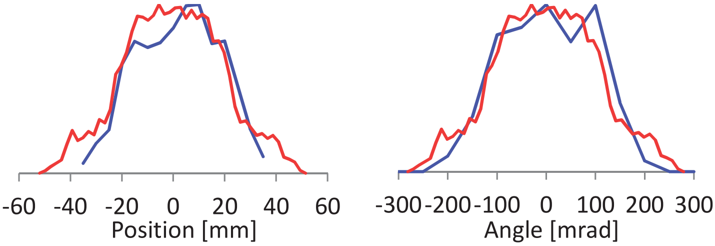

(c) Vertical position

(d) Vertical angle

Figure 5.22: Comparison between measured (blue) and simulated (red) beam projections. The intensities are normalized.

was preferred because of its flexibility, and because the electron dumping was done in a controlled way with a lower electron beam power density on the dump.

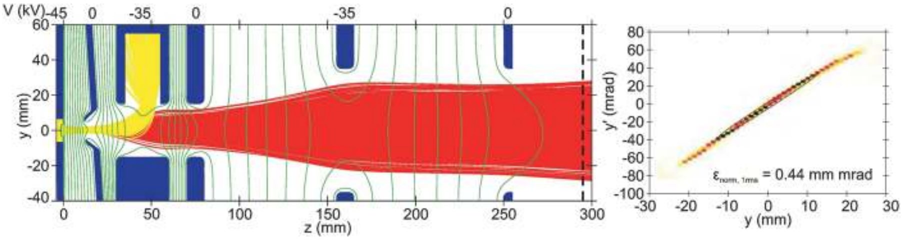

(a) Extraction system with a magnetized Einzel lens electron dump. A puller tilt corrects for the deviation of the H^- beam due to the magnetic field for the electron dump.

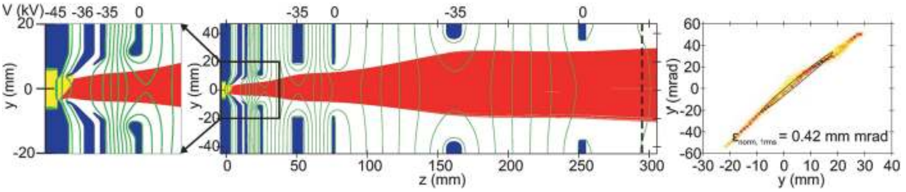

(b) Extraction system with the electron dump on an intermediate electrode.

Figure 5.23: Particle trajectory plots representing the two candidates for a new extraction system [78]. Both simulations were made with an H^- beam current of 30 mA, and an e/H^- ratio of 50. The H^- beam is shown in red, and the electron beam in yellow. The emittance is calculated at the LEBT entry, 295 mm from the plasma aperture.

5.3.5 Extraction system with a magnetized Einzel lens electron dump

The new H^- ion beam extraction system has a tunable puller electrode voltage to optimize the beam formation, and a magnetized Einzel lens for the electron dumping as shown in Figure 5.24. This section presents the different parts of the extraction system and their effect on the ion beam.

Beam optics tuning with the puller electrode

The puller electrode provides the first stage of acceleration of the H^- beam. It has in addition two tuning possibilities: (1) a variable voltage to give the best matched electrical field to the plasma density, and (2) a tilt and/or a displacement for correcting the misalignment of the H^- beam caused by the magnetic field in the electron dump.

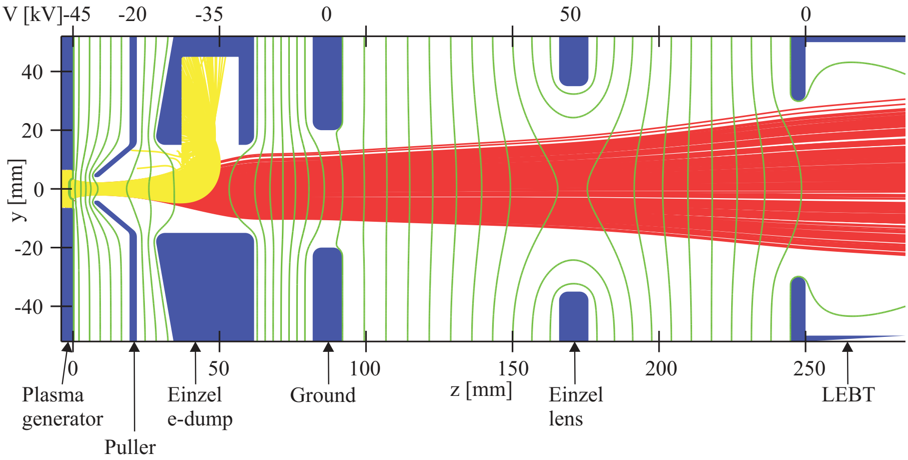

Figure 5.24: Simulation of the extraction system of the Linac4 ion source for an H^- current of 30 mA and an e/H^- ratio of 50 [95]. The electron beam in yellow is deviated and dumped into the magnetized Einzel lens. The H^- beam in red is focused by two Einzel lenses and transported to the LEBT.

1. The effect of the extraction voltage (i.e. $V_{\text{puller}} - V_{\text{plasma generator}}$) on the H^- ion beam can be visualized by systematic simulations. Here, we represent these beam properties by the H^- beam emittance, and the efficiency of the H^- transmission and electron dumping. The H^- transmission efficiency is the fraction of H^- ions that reaches the LEBT entry, and likewise, the electron dumping efficiency is the fraction of electrons that are dumped inside the magnetized Einzel lens. Electrons dumped on the sidewalls of the magnetized Einzel lens, outside the dumping cup, are not included in the calculation. Figure 5.25 shows the simulation results where these beam parameters vary as a function of the puller voltage for two different cases: (1) 20 mA H^-, e/H^- = 40, and (2) 30 mA H^-, e/H^- = 50. These plots show that for each of the two cases, there exists an optimum extraction voltage for minimum emittance and maximum transmission efficiency. The optimum extraction voltage is 17.5 kV for the first case, and 25 kV for the second case.

   Already from Figure 5.25 we see that for a higher extracted beam current, a stronger extraction field is required for minimum emittance and good transmission. We now assume that the beam size and emittance of the H^- beam is mainly defined by the extraction field and the space charge effects of the H^- ions and electrons, and depend less on the beam transport after the electron dump. We

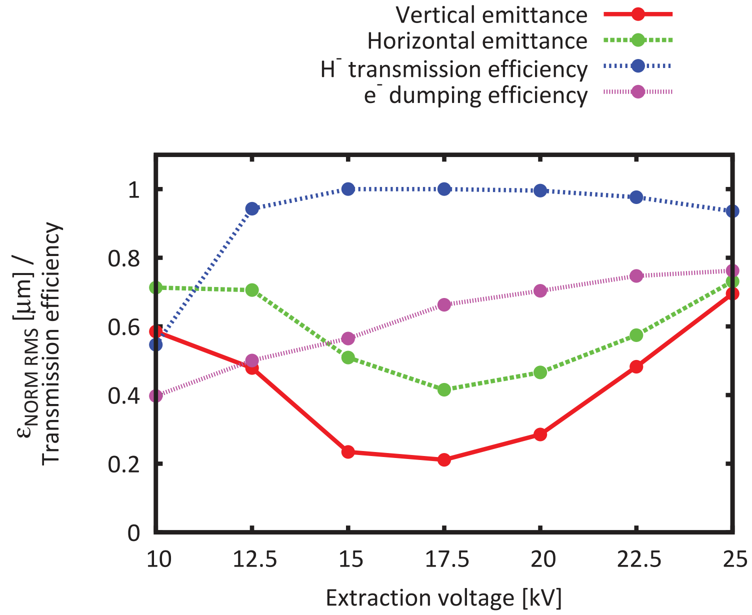

(a) 20 mA H^-, e/H^- = 40.

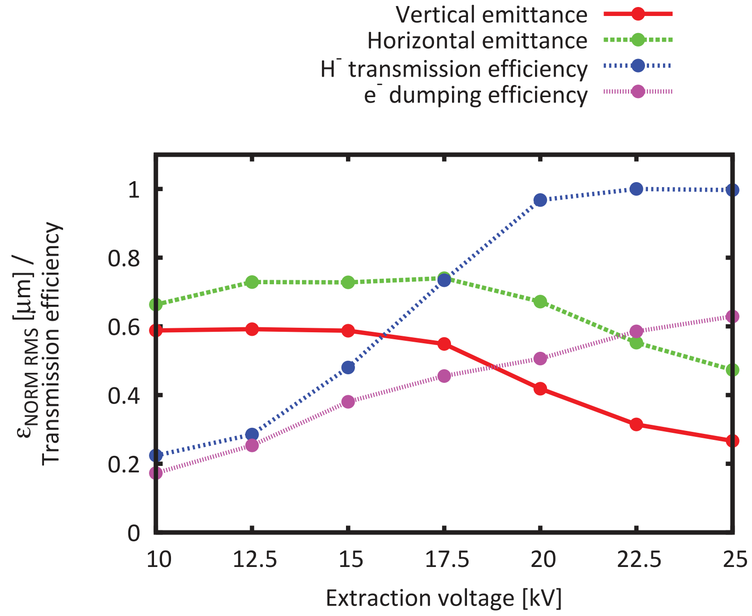

(b) 30 mA H^-, e/H^- = 50.

Figure 5.25: Emittance, H^- transmission and electron dumping efficiency as a function of the extraction voltage ($V_{\mathrm{puller}} - V_{\mathrm{plasma\ generator}}$) for two different beam currents.

then combine the space charge effects of the two components into what we call the total space charge equivalent H$^-$ current, $I_{tot\,H^-eqv}$, to better visualize the effect of the extraction voltage on the beam quality.

$$I_{tot\,H^-eqv} = I_{H^-} + I_e\sqrt{\frac{m_e}{m_{H^-}}}, \tag{5.1}$$

where I_{H^-} and I_e represents the extracted H$^-$ and electron currents, respectively, and m_{H^-} and m_e their respective masses.

Figure 5.26 shows the vertical and horizontal emittances, and the H$^-$ transmission and electron dumping efficiencies as a function of the extraction voltage and I$_{tot\,H^-eqv}$. The plots show that the highest H$^-$ transmission efficiency and lowest emittance is obtained with the puller voltage, which is a function of the extracted beam current. As expected, we see that for a higher extracted beam current (total space charge equivalent H^-), a higher extraction voltage is needed.

2. The second tuning possibility of the puller electrode compensates for the beam offset induced by the electron dump magnetic field. The correction is made by a tilt and/or offset of the puller in the horizontal plane. Figure 5.27 shows the impact of the puller tilt and offset that provides a zero position and angle of the H$^-$ beam at the LEBT entry. For these simulations, the H$^-$ beam current was 30 mA, the e/H$^-$ ratio 50, and the extraction voltage 25 kV. The crossing point of the two lines shows the condition that provides an H$^-$ beam with no offset and which is parallel to the beam axis. In this case, the lines converge to a tilt of $-5°$ and an offset of 0.85 mm. The beam position and angle are very sensitive to the offset of the puller (5.3 mm/mm and 10 mrad/mm, respectively). However, the variation is less dependent on the puller tilt (0.16 mm/deg and 0.12 mrad/deg, respectively). Because these values depend on the extracted beam current, the e/H$^-$ ratio and the puller voltage, the puller tilt and offset should be tunable *in situ*.

Electron dumping and beam focusing with a magnetized Einzel lens

The second electrode of the extraction system is a magnetized Einzel lens. This electrode focuses the H$^-$ beam, and dumps the electrons by a magnetic dipole field as illustrated in Figure 5.28. The deviation of the H$^-$ beam is not corrected by a second opposite dipole as for the DESY source. In this way, the electrode is short (30 mm) and the emittance growth at low beam energy (10 keV) is reduced. Because of the compact design and the strong magnetic field, a small fraction of the electrons (< 1 %) could

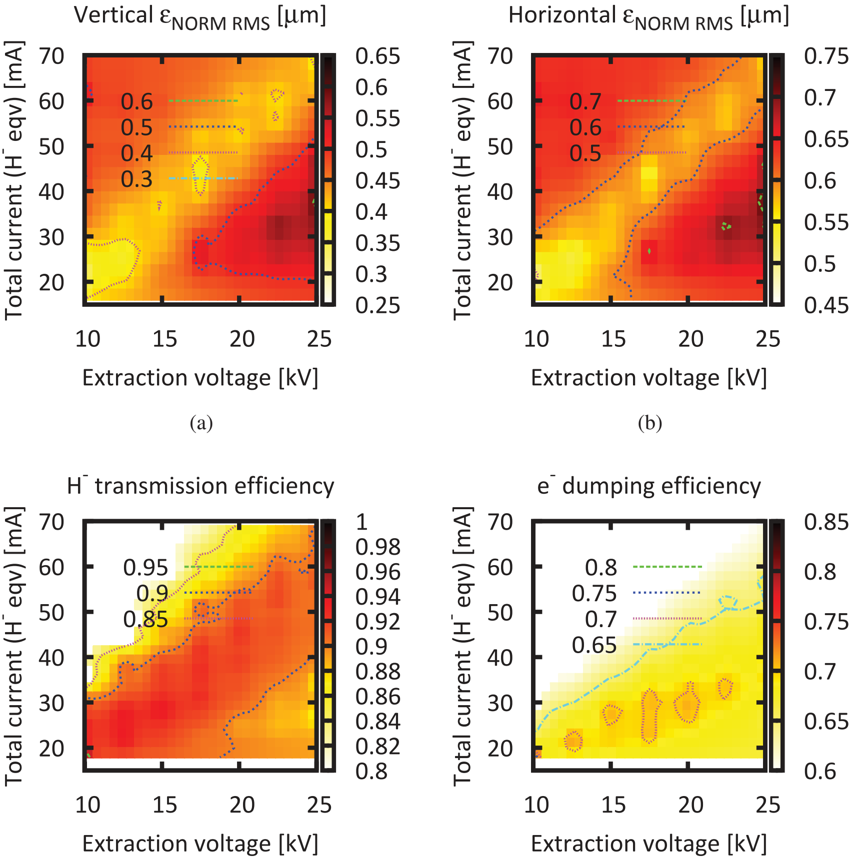

(a)

(b)

(c)

(d)

Figure 5.26: (a) Vertical emittance, (b) horizontal emittance, (c) H^- transmission efficiency, and (d) electron dumping efficiency as a function of the extraction voltage ($V_{\text{puller}} - V_{\text{plasma generator}}$) and the total space charge equivalent H^- current, $I_{tot\,H^-\,eqv}$.

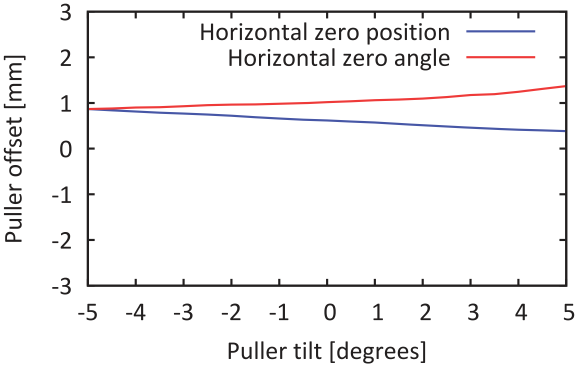

Figure 5.27: Puller tilt and offset that provides a horizontal zero position (blue line) and angle (red line) of the H^- beam at the LEBT entry.

return back to the puller, as is visible in Figure 5.24. The quantity depends on the beam current and the tuning of the extraction system. However, this situation is acceptable compared to the risk of having electrons being transported through the electrode and which follow the H^- beam or hit the grounded electrode with an energy of 45 keV. The H^- beam misalignment can be corrected by applying an offset and/or tilt to the puller as described in Section 5.3.5.

The dipole magnets are made of SmCo, which have a surface field strength of 1.05 T (Vacuumschmelze, Vacomax 170 [92]). Their dimensions are 38.1 mm × 9.9 mm × 6 mm, and they are spaced by 43 mm. A housing of ferromagnetic steel surrounds the magnets and forms a return yoke for the magnetic field lines. Figure 5.29 compares the simulated and measured B-fields along the z-axis, and in the xy-plane. The simulations were made with Vector Fields Opera, and a three axis Hall probe was used for the measurements. From the z-axis measurement, we see that the B-field is well confined inside the electron dump and rapidly drops to zero outside. On the other hand, in the xy-plane, we observe that the B-field is not uniform in the horizontal (y) or the vertical (x) direction. This means that electrons will see different magnetic field strength depending on their position in the beam, and they will thus be deflected differently. One way of creating a more uniform B-field is to use stronger magnets placed further away from each other. However, for such a compact structure as this electron dump, it is very difficult to achieve a uniform B-field because of the rapidly decreasing field strength from the magnet surface.

As described in Section 5.1.2, the electron dumping at 45 keV beam energy caused

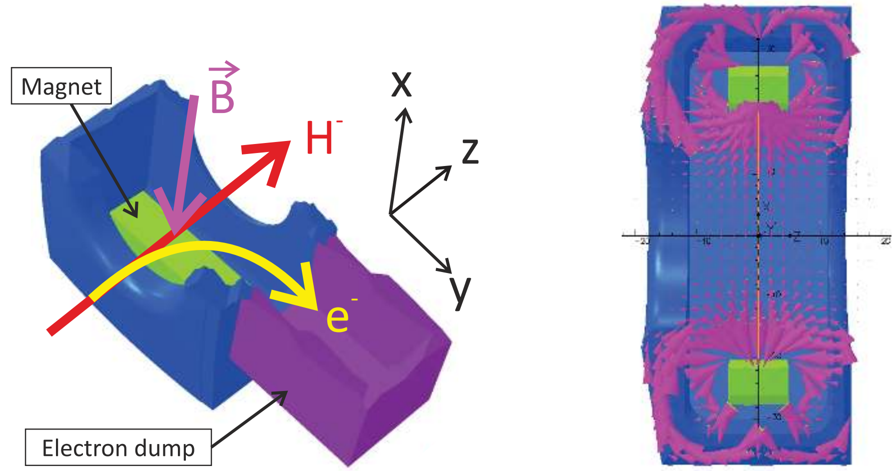

(a) Cross section of the magnetized Einzel lens electron dump.

(b) Magnetic field vectors (purple) in the zx-plane. The iron housing (blue) guides the B-field lines and confines the field inside of the magnetized Einzel lens.

Figure 5.28: A single dipole pair (one magnet shown in green) creates the magnetic field that separates the electrons from the H^- beam. The electrons are dumped in a tungsten cup (purple). A housing of ferromagnetic steel surrounds the magnets and forms a return yoke for the magnetic field lines.

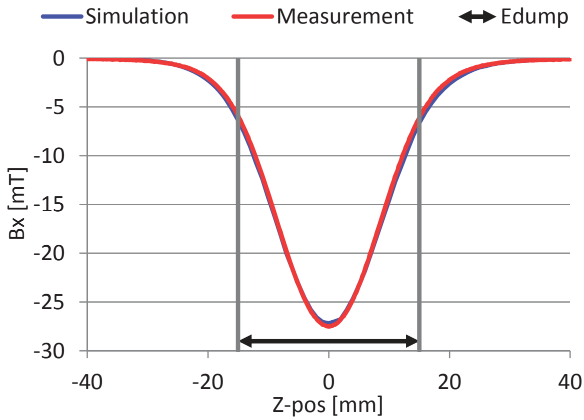

(a) Vertical B-field along the z-axis. The arrow indicates the length of the electron dump.

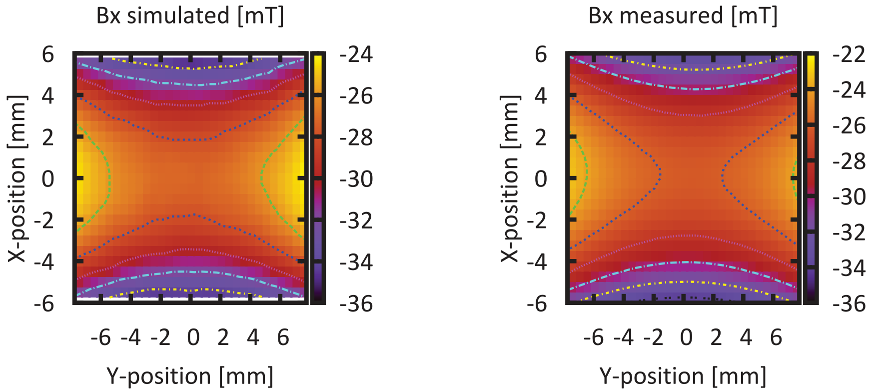

(b) Simulation of the vertical B-field in the xy-plane.

(c) Measurement of the vertical B-field in the xy-plane.

Figure 5.29: (a) Comparison of the simulated and measured vertical B-field along the z-axis. (b) Simulation of the B-field in the xy-plane. (c) Measurement of the B-field in the xy-plane. The electron dump is 30 mm long, and has a 30 mm diameter aperture.

sublimation of the dump material resulting in high voltage breakdowns in the source. The simulation of that extraction configuration showed a peak electron beam power density of 3.0 kW/mm^2 in the cup, and transient thermal simulations suggested that this value should be kept below 1 kW/mm^2 for a graphite surface. The new electron dump has a tungsten cup, which can accept a factor two higher electron beam power density before surface ablation. This is still not sufficient for avoiding thermally induced damage. In addition to changing the material, the electron beam energy in the dump is therefore reduced from 45 keV to 10 keV and the electron dump optics has been designed to spread the beam over a larger surface in the dump. Figure 5.30 shows the maximum power density in the magnetized Einzel electron dump as a function of the extraction voltage and the total space charge equivalent H$^-$ current. The figure illustrates that even the highest calculated power density is a factor 6 lower than the ablation limit for tungsten, and should be well within the safety margin for operation.

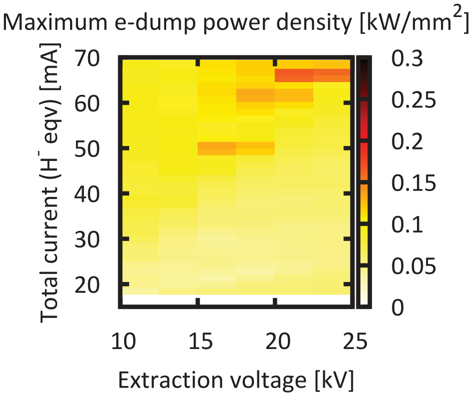

Figure 5.30: Maximum power density in the electron dump as a function of the extraction voltage and the total space charge equivalent H$^-$ current.

Because of the low duty factor of the ion source (2 Hz, 0.5 ms), no active cooling of the dump is implemented. Instead, the heat from the electron beam is evacuated by thermal radiation and conduction through a copper leg and a Shapal ceramic insulator to the stainless steel source body. The average heat distribution in the dump was studied by an ANSYS steady state thermal simulation showing that the temperature increases from room temperature to 57° C for a 1.8 A electron beam with 600 μs pulse length and a repetition rate of 2 Hz [95].

Ensuring the beam transport with an Einzel lens

The purpose of the second Einzel lens is to transport the H^- beam to the LEBT while keeping the beam size small, and to avoid excessive emittance growth. A negative bias will decelerate the beam and provide stronger focusing. However, it causes space charge induced emittance growth because of the low ion velocity inside the Einzel lens. A positive Einzel lens bias is thus preferred since the emittance is kept low. However, the applied voltage needs to be higher than for the decelerating Einzel lens to avoid particles hitting the beam pipe. Figure 5.31 demonstrates the improved emittance of the accelerating lens. The simulations have been made with voltages up to 50 kV for demonstration purpose. However, it should be noted that the Einzel lens insulation in the installed ion source only supports 35 kV.

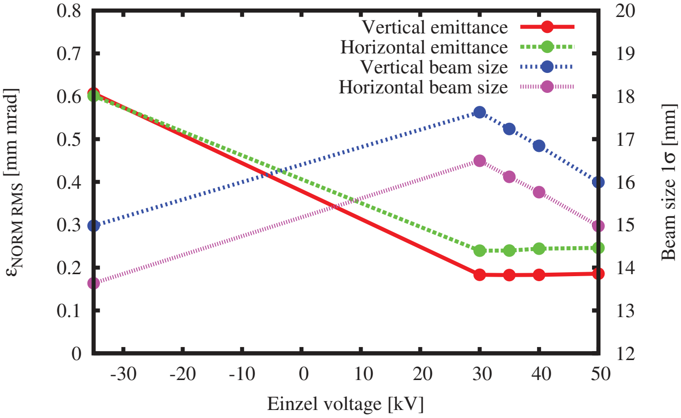

Figure 5.31: Simulation of the emittance and the beam size as a function of the Einzel lens voltage [95]. H^- beam current is 30 mA, e/H^- is 50 and puller voltage is -20 kV.

Extraction of a proton beam

In order to test the LEBT and RFQ in a higher space charge regime, the source will run in proton mode by reversing the polarity of the high voltage systems. Figure 5.32 shows that it should be possible to run the ion source with a proton beam of 80 mA being extracted through the same geometry as for the H^- beam.

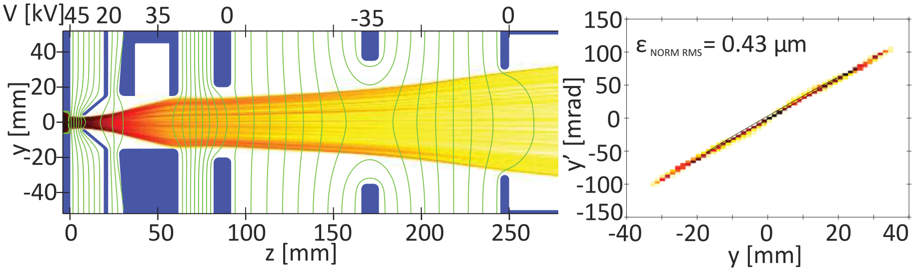

Figure 5.32: 80 mA proton extraction with inverted polarities on the electrodes. Left: proton particle density plot. Right: phase space plot at the simulation end.

Pulsed high voltage system

The extraction system electrodes are supplied by a set of pulsed high voltage transformers. These were designed with the purpose of avoiding high voltage breakdowns between beam pulses that would stop the ion source operation. In addition, they regulate the voltage during the beam pulse to keep a constant voltage, and thus a constant beam energy. From the beam quality point of view, this is a better solution than using a capacitively stored energy that has a voltage drop during the beam pulse depending on the extracted beam current as described in Section 5.1.2.

Figure 5.33 shows a diagram of the pulsed high voltage transformers, and Table 5.2 summarizes the parameters of the power converters. The first transformer sets the voltage of the plasma generator to −45 kV referenced to ground potential. The second and third transformer apply positive voltages to the puller and electron dump, respectively, both referenced to the plasma generator. The second Einzel lens uses a DC power converter. Two independent current measurement systems are implemented: one that measures inside the high voltage transformer rack, and a set of Pearson transformers that measure the current going through the cables connected to each independent electrode.

Table 5.2: High voltage system parameters and nominal settings [76].

	Voltage	Current	Duration	Nominal voltage
Plasma generator, racks	−50 kV	0.1 A	2 ms	−45 kV
Puller electrode	+25 kV	1 A	2 ms	−20 kV
Electron dump	+10 kV	1 A	2 ms	−35 kV
Einzel lens (DC + 30 nF)	+/− 50 kV	0.1 A	1 ms	+35 kV

Figures 5.34 and 5.35 show the measured voltages relative to ground and currents

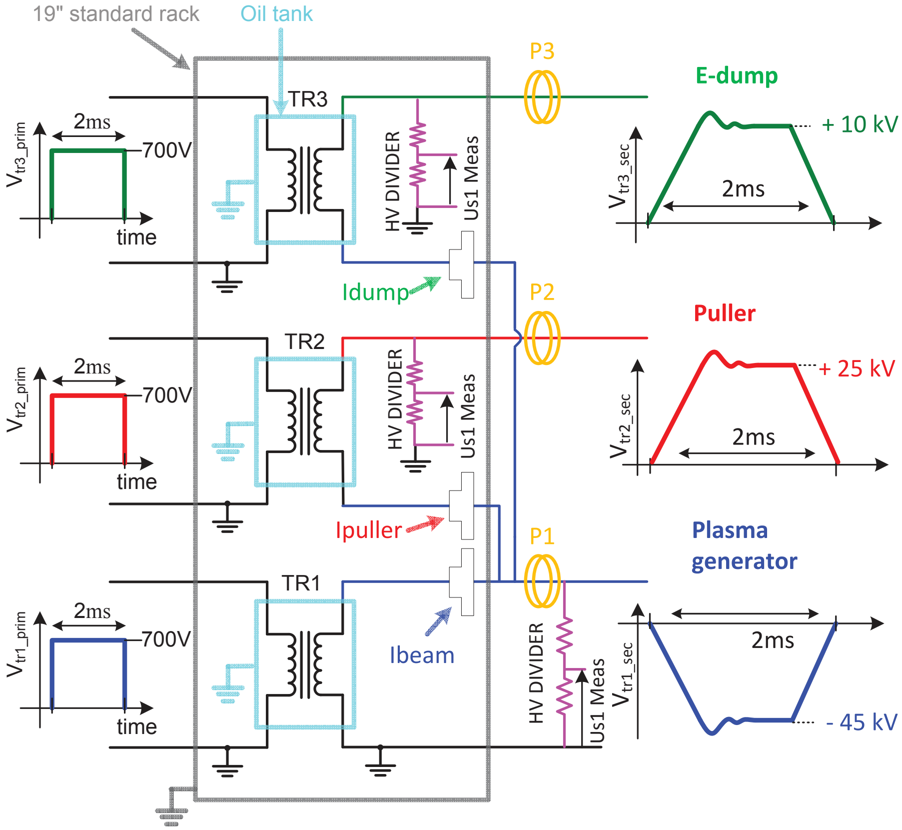

Figure 5.33: Schematics of pulsed high voltage power converters. The puller and electron dump are referenced to the plasma generator. Ibeam, Ipuller, and Idump indicate the location of the current measurement inside the rack. P1, P2, and P3 in yellow show the location of the Pearson transformers.

for one beam pulse. The voltage rise time is about 0.3 ms, and during this time there is a current on all three transformers approaching zero as the voltage stabilizes. The plasma is then ignited as seen from the perturbation of the voltage and current signals. In this way, there is no beam extracted during the voltage ramp-up. At t = 0, the voltages are stable for the beam duration of 0.4 ms, and we observe a stable current on the three transformers. The fall time is approximately 0.5 ms.

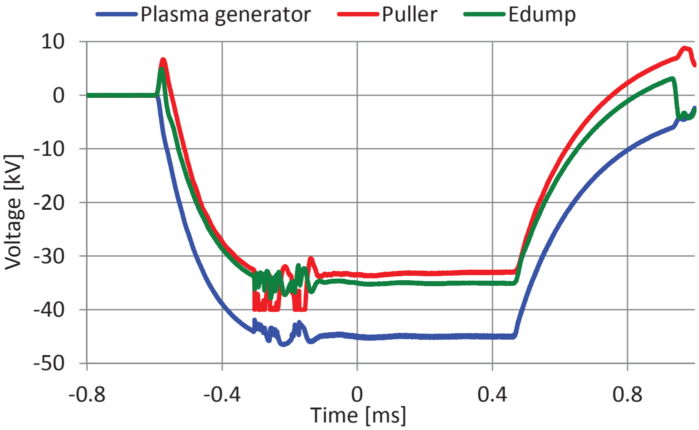

Figure 5.34: Measured voltages of the high voltage transformers with the measurement system inside the high voltage transformer rack.

5.3.6 First experiences with the extraction system

The new extraction system was first installed together with the plasma generator IS01 in December 2012, as shown in Figure 5.36. As explained in Section 5.2.1, this plasma generator did not produce a significant number of H^- ions. However, at that time it was not clear whether this was related to the plasma generator, or the extraction system. The next step was to install the DESY plasma generator, which was known to produce H^- ions. With this configuration, the ion source successfully produced the first H^- ion beam of 45 keV in February 2013. Figure 5.37 shows the beam current waveforms of one of the beam pulses measured with the Pearson transformers and the Faraday cup. Table 5.3 summarizes the ion source voltages and currents. A positive current means that negative charges leave the electrode and vice versa for a negative current.

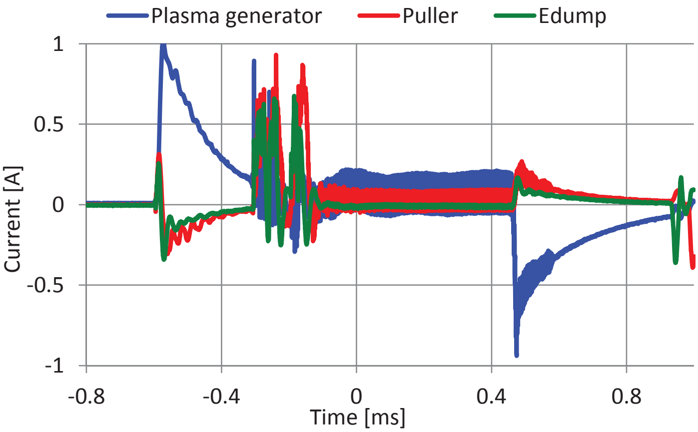

Figure 5.35: Measured currents of the high voltage transformers with the measurement system inside the high voltage transformer rack.

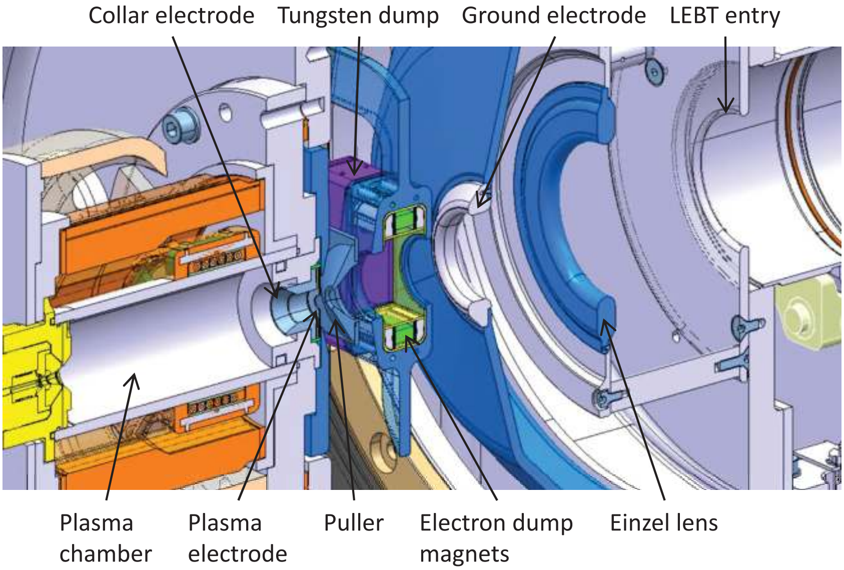

Figure 5.36: Cross section of the IS01 plasma generator, and the beam extraction system.

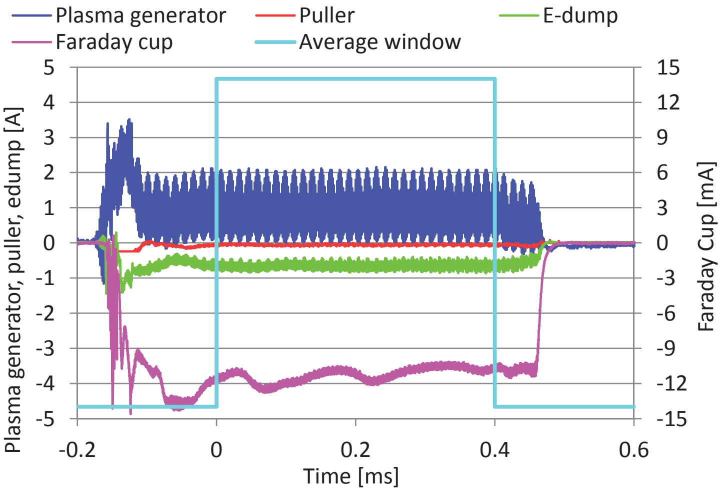

Figure 5.37: First beam currents measured with the new extraction system and the DESY plasma generator. The average H^- beam current from 0 to 0.4 ms was 11 mA, and the total current extracted from the plasma generator was about 800 mA.

Table 5.3: Summarized voltages and currents measured on the different electrodes of the extraction system. The values have been averaged between t = 0 and t = 0.4 ms.

	Voltage [kV]	Current [mA]
Plasma generator	−45	833
Puller	−28	−58
Electron dump	−36	−656
Einzel lens	+35, 0	−153, −45
Faraday cup	-	−11

We observe that most of the 800 mA negative charges that leave the plasma generator were collected in the electron dump. A small fraction of the electrons hits the puller, which consists of primary electrons extracted from the plasma generator that hit the puller directly, and/or secondary electrons emitted from the electron dump by impacting electrons and/or H^- ions. On the Einzel lens, we see a high negative current without any obvious reason. All the H^- ions should have stayed well clear of this electrode, and none of the electrons should pass the magnetic field of the electron dump. The measured current originated most likely from ionization of the rest gas by the beam, or from secondary electron emission of the electrodes at ground potential from impacting electrons or ions. With the Einzel lens at ground potential, the current was suppressed and reduced to -45 mA. The Faraday cup measured -11 mA of H^- ions.

5.4 Low energy beam transport

The ion source is connected to the LEBT, which is shown in Figure 5.38. The LEBT ensures the beam transfer from the ion source to the 352 MHz RFQ [96]. Two water-cooled, DC solenoid magnets with external magnetic shielding provide the matching into the RFQ, and two sets of horizontal and vertical dipole window DC magnets (steerers) correct the beam trajectory. The pre-chopper deflects the beam from the RFQ with a fast rising electric field. The purpose is to remove the start and the end of every beam pulse as required for the RFQ.

Several beam instruments are permanently installed in the LEBT. The beam current can be measured either with the retractable Faraday cup in the diagnostics tank, or non-destructively by the beam current transformer (BCT) in front of the second solenoid. Horizontal and vertical harps are located in the diagnostics tank for profile monitoring. In addition, a slit and grid emittance meter can be temporally installed in place of other equipment in, or at the end of the LEBT.

Figure 5.39 shows a comparison between the phase space image of the measured and simulated beam. For this measurement, the emittance meter was placed in the position of the BCT, which was removed together with the second solenoid. The simulated beam has been modelled and fully tracked with IBSimu. The plots show some similarities, with a dense beam core having the same orientation and a low-density halo that simulations show to be generated at the source extraction aperture. There is also a good correspondence between the two images with similar beam emittance values: 0.49 µm for the measurement and 0.52 µm for the simulation, both values normalized, 1 rms.

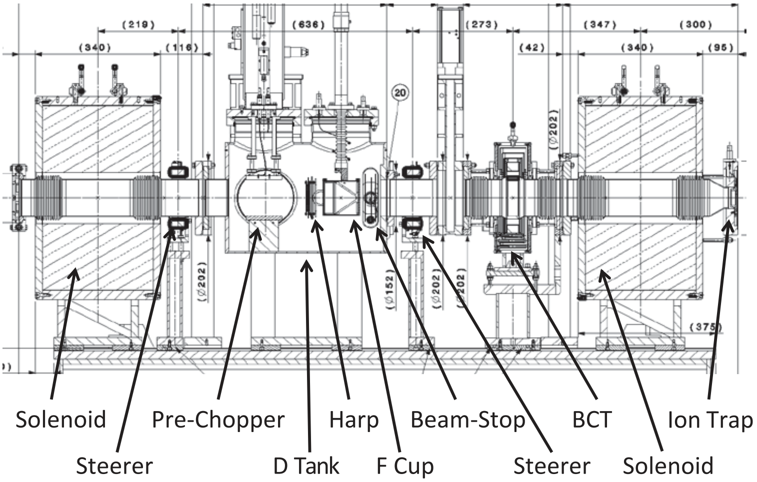

Figure 5.38: Layout of the LEBT as installed at the 3 MeV test stand [96]. D Tank = Diagnostic Tank, F Cup = Faraday Cup, Harp = Harp profile monitor, BCT = Beam Current Transformer. Beam travels from left to right.

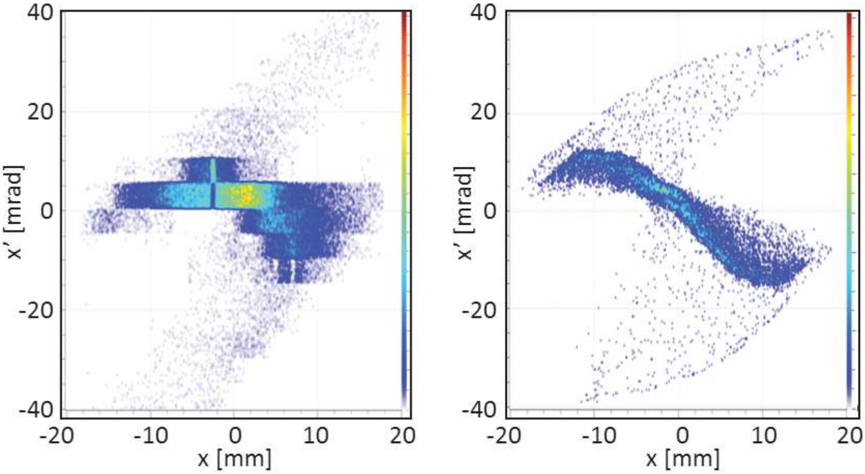

Figure 5.39: Phase space measurement (left) and simulated (right), colours represent the particle density. [55].

Chapter 6

Measurements and analysis

This chapter presents measurements of the beam extraction system, and comparisons with simulations. First, we will look at the detailed Linac4 requirements that were introduced in Section 3.1, and see how they can be measured. We proceed by characterizing the extraction system, and at the end we will discuss further improvements.

6.1 Methods of measuring particle accelerator requirements

Particles accelerator requirements for ion sources were described in Section 3.1, and summarized for the Linac4 ion source in Table 5.1. Here we will go through these requirements, and describe how they can be measured.

Particle type Linac4 is a negative hydrogen ion, H^-, linear accelerator. In addition to this particle type, the ion source also needs to be able to deliver a proton, H^+, beam for commissioning with higher beam intensity.

The source extracts H^- ions and electrons. The electrons are primarily separated according to the difference of momentum between the ions and electrons with a magnetic field in the electron dump. Further selection is performed by the different focusing properties of a solenoid magnet (selection by momentum per charge) and the RFQ (selection by velocity and energy per charge).

Energy The beam energy of the ion source is defined by the input energy of the first accelerating element, which, in the case of Linac4, is the RFQ. This structure requires a 45 keV beam for correct matching, and maximum 1 % beam energy spread for minimal beam losses.

The voltage applied to the plasma generator defines the ion beam energy at ground potential. This voltage is regulated during the beam pulse, and is specified to stay within 1 % of the reference value. Figure 6.1(a) shows the distribution of the measured mean voltages ($\langle V \rangle$ averaged between 0 and 400 µs) from the high voltage power converters. The variation within each beam pulse is shown in Figure 6.1(b), where the distribution of the standard deviation of the voltages (σ_V evaluated from 0 to 400 µs) from each beam pulse is plotted. The measurements were made during a weekend when the ion source was running undisturbed. The plots show that the voltage variation stays within the RFQ tolerance.

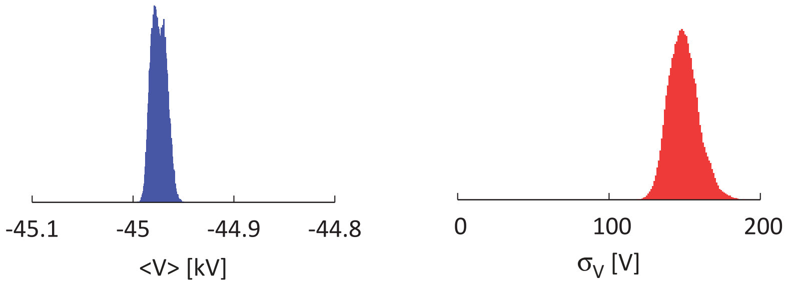

(a) Histogram of the measured mean voltage ($\langle V \rangle$ averaged between 0 and 400 µs).

(b) Histogram of the standard deviation of the voltage during the beam pulse.

Figure 6.1: High voltage stability of the plasma generator during one weekend of continuous ion source operation. The plasma generator voltage defines the beam energy, and is the main source of beam energy spread in the LEBT.

Intensity The beam intensity is measured by a Faraday cup or non-destructively by a Beam Current Transformer (BCT).

The Faraday cup includes a negatively biased guard ring at the entrance to prevent secondary electrons from being emitted from the measurement cup. If secondary electrons were allowed to escape, the measured H^- current would be lower than the real beam current. The opposite effect applies for a positive ion beam current. The necessary guard ring voltage also depends on the beam intensity. Figure 6.2 shows the effect of the guard ring voltage on the measured beam current. Beam intensity measurements require $-V > 100$ V for a 15 mA H^- beam, and $-V > 600$ V for a 40 mA proton beam. All ion beam intensity measurements presented have been made with the Faraday cup with a guard ring voltage of -1000 V.

The H^- beam intensity from the ion source has reached 60 mA with the cesiated IS02 plasma generator. This achievement was made with 90 kW RF-power. During one month of operation the beam current remained stable at 35 mA with 30 kW RF-power. The IS01 plasma generator demonstrated a stable 50 mA proton beam during a period of two weeks.

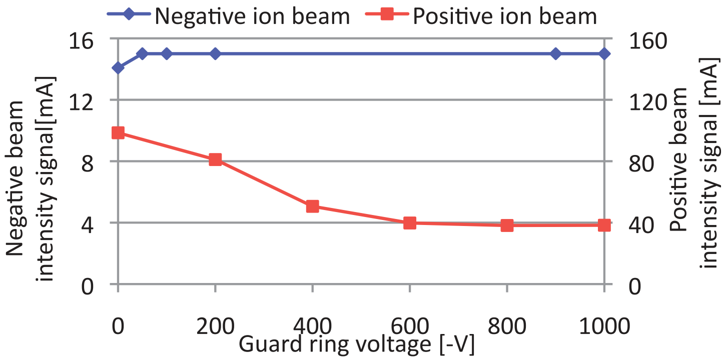

Figure 6.2: Effect of negative guard ring bias on the beam intensity signal. $-V > 100$ V is necessary for a 15 mA H^- beam, and $-V > 600$ V for a 40 mA proton beam.

Emittance Linac4 requires the source to deliver a beam within a normalized rms beam emittance of 0.25 μm [20].

A slit-grid emittance meter measures the emittance. This device consists of a horizontal (and a vertical) slit that allows beamlets at a certain position to pass through. A set of vertical (or horizontal) grid wires then measure the angular distribution of the beamlet passing through the slit.

The rms emittance can be calculated with Equation 3.10. There is, however, an error associated with this method because of background noise to the measurement. The background noise can be removed from the signal by thresholding, or by using more advanced algorithms such as SCUBEEx [97]. The ion source community is normally thresholding the signals at 10 %. A selection of measured emittances with different plasma generators is presented in Table 6.1.

Time structure The required beam pulse length is 400 μs at 2 Hz. Within these 400 us, the beam intensity should be stable, and the rise and fall times short. This is a square beam pulse.

Table 6.1: Measured emittances from the DESY plasma generator, IS01, and the non-caesiated and caesiated IS02.

	DESY	IS01	IS02	IS02 (Cs)
Beam intensity [mA]	17	11	29	50
$\varepsilon_{\text{norm,rms}}$ 0.4 % threshold [µm]	0.69	0.52	0.65	1.04
$\varepsilon_{\text{norm,rms}}$ 10 % threshold [µm]	0.40	0.30	0.16	0.37

To arrive at a quasi-square beam pulse, control of the pulsed source elements is needed as shown in Figure 6.3. The high voltage is pulsed, and in order not to load the high voltage during the rise of the pulse, the plasma is off during the voltage ramp. When the high voltage is stable, the RF switches on and ignites the plasma. Once the plasma is formed, a current will be drawn from the plasma generator, and this current causes a change in the plasma generator voltage. The beam characteristics at the start of the pulse can therefore vary out of tolerance. When the beam intensity has stabilized, the RF stays on for about 500 µs, and stops before the high voltage ramps down. A fast rising electrostatic pre-chopper deflects and dumps the unstable first part of the beam and the pulse end in the LEBT. The result is then a stable quasi-square pulse as illustrated in the figure. This is not the actual chopped beam, but an approximation made by removing parts of the Faraday cup signal. As the space charge compensation time for an electrostatic chopping system is in the order of hundreds of nanoseconds [56], the trace is a good approximation.

At present, the ion source runs with a repetition rate of 0.8 Hz (one pulse every 1.2 s), which is the repetition rate of Linac2. Tests at 2 Hz have already confirmed that the source is operational also at this repetition rate.

Efficiency/purity The efficiency of high intensity hydrogen ion sources is poor considering the amount of produced ions compared with the quantity of H_2 gas that is injected into the plasma generator. However, since hydrogen gas is quite cheap and not polluting, the efficiency is rarely considered. Hydrogen gas is flammable, and extra precautions need to be taken for safety reasons. It is also important that the evacuated gas is not confined for risks of accumulation and high explosive risk.

H^- ion beams have, on the other hand, a high purity. The beam consists mostly of H^- and electrons, but there could also be fractions of heavier ion impurities such as O^- or C^- originating from the air when the plasma generator has been under atmospheric pressure. Such impurities have not been observed and should

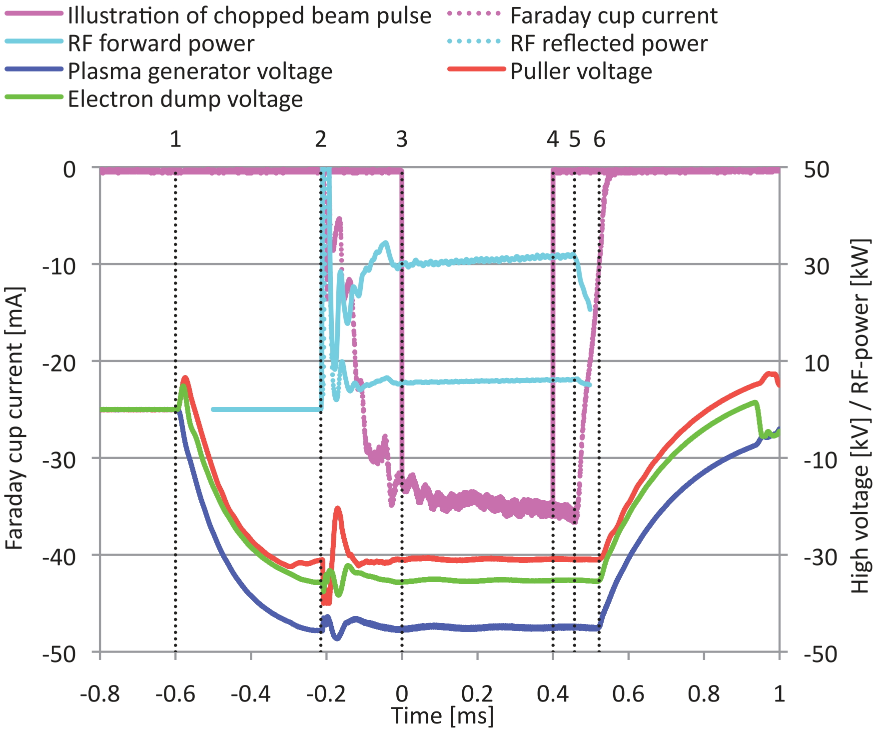

Figure 6.3: Time structure of an H^- beam pulse. 1: HV on, 2: RF on, 3: Pre-chopper off, 4: Pre-chopper on, 5: RF off, and 6: HV off. The result is a quasi-square H^- beam pulse.

in any case be insignificant after running the source for a few hours/days with plasma, which causes outgassing of the impurities from the chamber walls. When the beam has travelled through the beam extraction system with the magnetized Einzel lens electron dump, all the electrons should have been removed. Simulations have shown that a few secondary electrons emitted from the extraction electrodes may follow the H^- ion beam to the LEBT, but these are effectively stopped by the solenoid and are lost on the walls of the beam pipe. What remains of the beam after travelling through the LEBT should then be a very pure H^- ion beam.

In the case of a a positive hydrogen ion beam, fractions of H_2^+ and H_3^+ were measured from the DESY plasma generator using a dipole magnet for separating the masses. The ion beam contained approximately 80 % protons, and 10 % of H_2^+ and H_3^+ each, depending on the RF-power as shown in Figure 6.4. At higher RF-power, the fraction of protons increased.

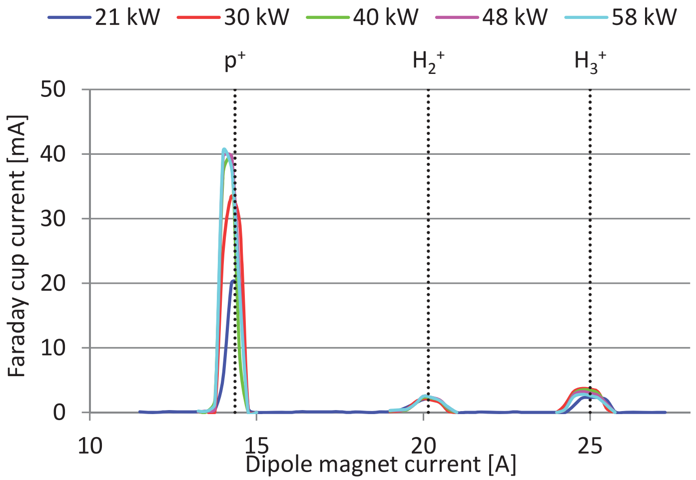

Figure 6.4: Measurement of proton, H_2^+ and H_3^+ fractions from the DESY plasma generator.

Reliability / stability Linac4 aims to achieve the same reliability as Linac2, which means 98.4 % per beam run that lasts for approximately 10 months. During a commissioning phase, however, it is very difficult to measure the long-term reliability. Many different sub-systems start up for the first time, and the ion source can stop frequently because of various reasons such as tuning or attempts to reach higher beam currents. Long-term reliability test will be performed on the Linac4 installation for a year before connecting to the PSB.

Short term reliability and stability tests are made continuously at the ion source test stand during week-end, when the source runs uninterrupted. The stability is good at this time scale, but has small variations. One parameter that influences the stability is the temperature. Especially the piezo valve for the pulsed gas injection is very temperature sensitive. A regulation of the applied voltage to the piezo valve has been implemented, which modifies this voltage according to the measured pressure in the ion source. Figure 6.5 shows the variation of the H^- beam current and the piezo valve temperature measured during two week-ends; one with the regulation of the piezo valve voltage on and one without the regulation. We clearly see from the plot that when the regulation of the piezo valve is off, the H^- current is strongly influenced. Figure 6.6 shows that without the regulation, the H^- beam current varies by approximately 5 mA per °C, whereas with the regulation, the current stays at a constant level.

6.2 Characterization of the extraction system

This section presents measurements that were done to characterize the extraction system, and compare its performance with simulations. All measurements were made with a negative ion beam from the DESY plasma generator, and the comparison with simulations was made with the currents measured on the plasma generator, puller and electron dump using Pearson transformers, and the H^- beam current measured in the Faraday cup. The layout for the experiments is shown in Figure 6.7. The simulations were made with input current densities of H^- and electrons that resulted in the best match to the measured currents. These results were presented in reference [98], which is included in Appendix C.

The following sections presents a measurement as a function of varying RF-power, a description of how the simulations need to include secondary electron emission, and finally a measurement with varying puller voltage.

6.2.1 The beam current density increases with the RF-power

In this measurement, the RF forward power was varied from 20 kW to 30 kW, and the currents on the electrodes and in the Faraday cup were measured. The results from the

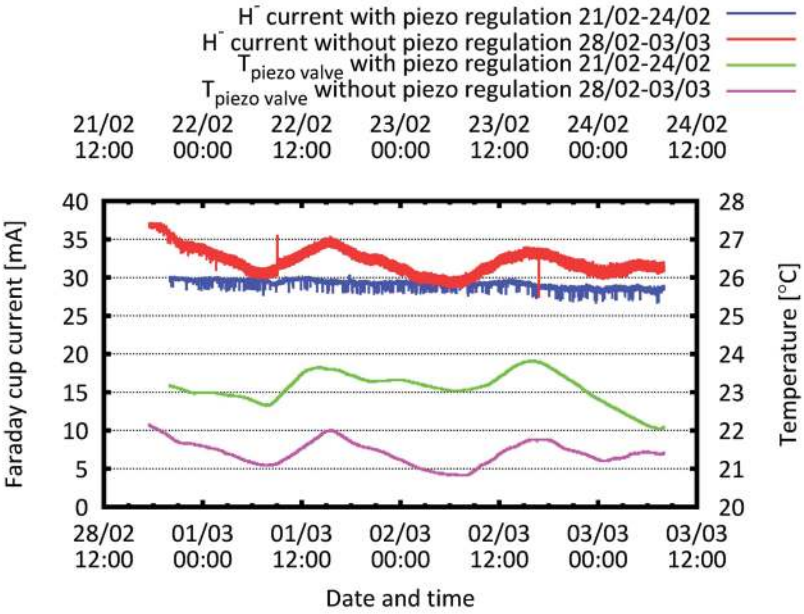

Figure 6.5: Temperature and H^- beam current illustrating the effect of the regulation of the piezoelectric valve.

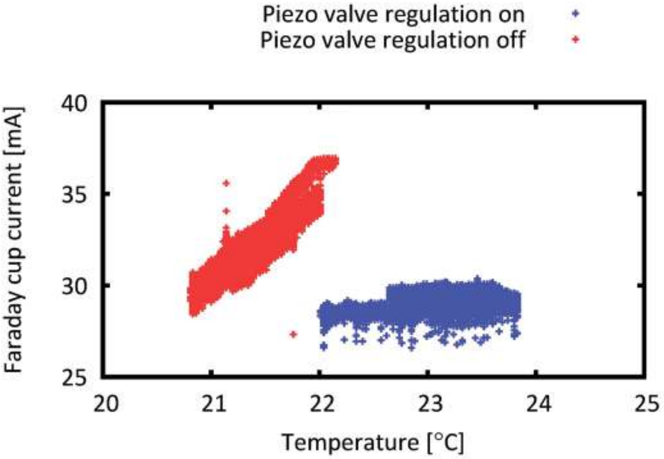

Figure 6.6: H^- beam current as a function of the temperature of the piezo valve.

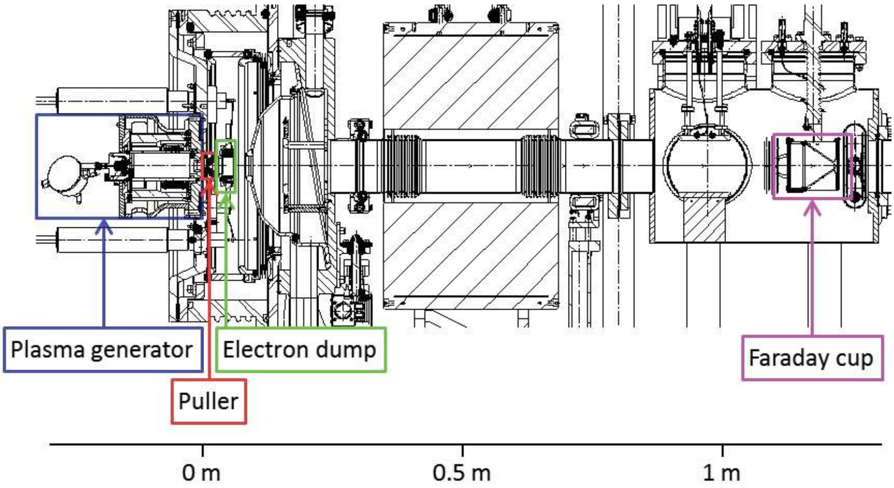

Figure 6.7: Layout of the Linac4 ion source and the first part of the LEBT. The boxes indicate the locations of the current measurements for comparison with simulations.

measurements and simulations are shown in Figure 6.8(a). The measurement shows an increase of the extracted beam current (marked Plasma generator Meas) as a function of higher RF-power, and the simulated values of the plasma generator and Faraday cup currents correspond well. The result is therefore consistent with the H^- and electron charge density in the plasma generator being proportional to the RF-power in the measured range.

6.2.2 Secondary electron emission needs to be included in the model

In Section 6.1 it was briefly described how a beam current measurement with a Faraday cup could give false results if secondary electrons were allowed to escape. In these measurements of the electrode currents, secondary electrons emitted from the electrodes affect the results in a similar way. Here is a description of what each of the electrodes should measure as current:

- The plasma generator measures the total current (H^- and electrons) that leaves the plasma, denoted as primary charges. Because this part has the lowest potential of the extraction system, no secondary electrons should be able to reach this electrode.

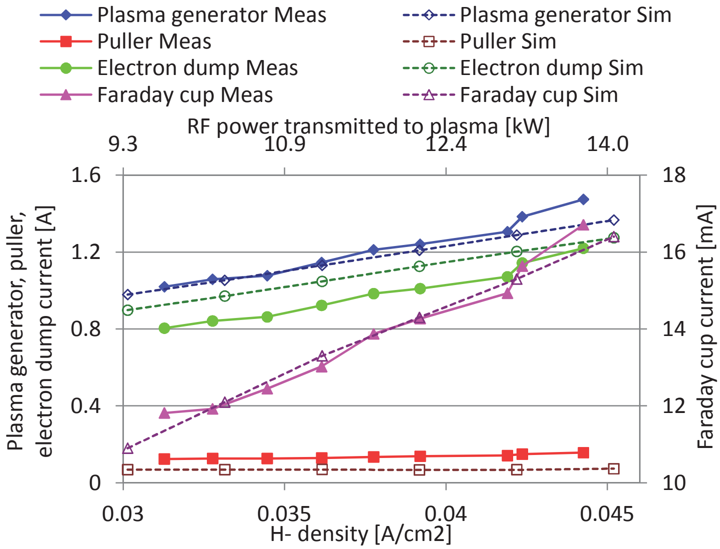

(a) Comparison between measurements of currents on the extraction system electrodes and simulations with varying RF-power. The RF-power that was transmitted to the plasma (i.e. the incident minus the reflected power) on the x-axis has been linearly scaled to match the H^- density used as input in the simulations.

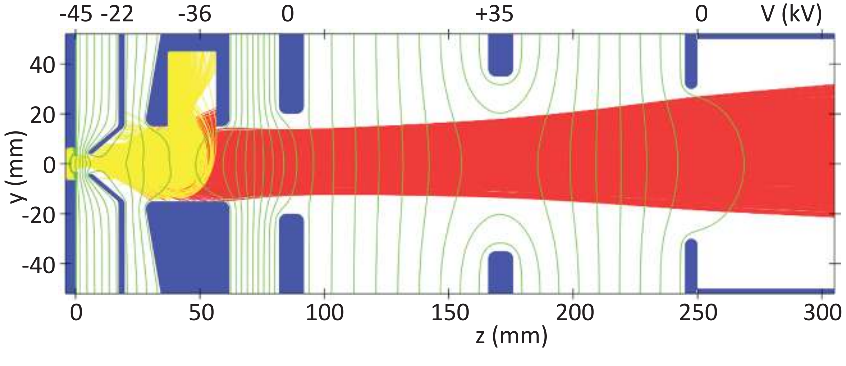

(b) Image from a simulation with an H^- current density of 0.03 A/cm^2 and an e/H^- ratio of 65. The beam is over-focused and parts of the H^- beam (red) scrape the inside of the electron dump. The electron trajectories are shown in yellow. Secondary electron emission is not included in this simulation.

Figure 6.8: Extracted beam as a function of the RF-power transmitted to the plasma.

- The puller electrode measures the impacting primary charges, either directly from the plasma generator, or deflected by the magnetic field of the electron dump. Secondary electrons emitted from the puller electrode cannot escape unless they have enough energy to overcome the potential barrier in the electron dump. Since the puller has a higher potential than the electron dump, this electrode also attracts secondary electrons emitted from the dump.

- The electron dump measures the impacting primary charges. Because the electrode is held at a low potential, secondary electrons are cleared by the electric fields, and escape easily. The exception are the electrons generated inside of the electron dump cup, which are repelled by the negative space charge of the incoming primary electrons.

- The Faraday cup has a guard ring that will prevent secondary electrons from escaping. As described in Section 6.1, the only charged particles that can be transported through the extraction system and the solenoid are H^- ions. The Faraday cup then provides a reliable measure of the extracted H^- beam transmitted to it.

The plot in Figure 6.8(a) shows that the measured puller current was higher than the expected value from the simulations, and the electron dump current was lower. Figure 6.9(a) shows the same plot with secondary electrons included in the simulation. The simulated currents now match the measurement. A simulation image is shown in Figure 6.9(b), and here we see that a large part of the secondary electrons in pink are travelling form the electron dump to the puller.

The emission of secondary electrons from surfaces was described in Section 4.3.3. The ratio of emitted electrons depended on various parameters, such as incoming particle type, energy, and incident angle. For these beam extraction simulations, a model has been used where the secondary electrons have the same current as the incoming particle, they are emitted with a random angle from the surface normal, and their energy is randomized between 0 eV and the energy of the impacting particle. This gives a correct order of magnitude estimation of the current carried by the secondary electrons.

6.2.3 The extracted beam current and optics depend on the puller voltage

The voltage of the puller electrode is adjustable to adapt the electric field near the plasma aperture to the current density, and optimize the shape of the plasma meniscus. Figure 6.10 shows the current dependencies of the extraction voltage (i.e. the difference

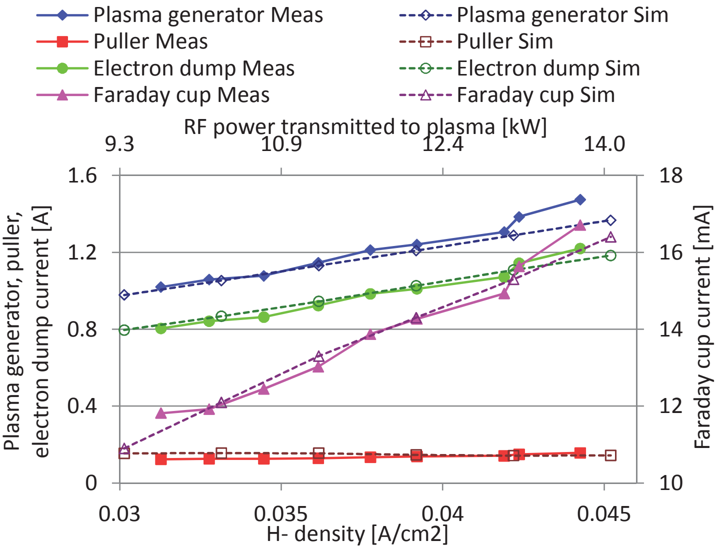

(a) Comparison between measurements of currents on the extraction system electrodes and simulations where secondary electron emission has been included. The effect of the secondary electrons is a lower electron dump current and a higher puller current in the simulations. The result is a better match between the measurements and the simulations.

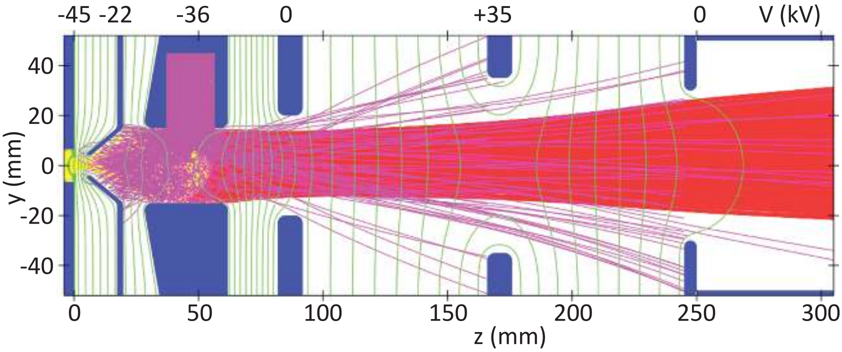

(b) Image from a simulation with an H^- current density of 0.03 A/cm^2 and an e/H^- ratio of 65. Secondary electrons (pink) are emitted from the electron dumps with some trajectories hitting the puller electrode.

Figure 6.9: Extracted beam as a function of the RF-power transmitted to the plasma including secondary electron emission from the electrodes in the extraction system.

between the puller and plasma generator voltages). The simulations agree well with the measurements. We make two observations of the total current extracted from the plasma generator: (1) it increases with higher extraction voltage, and (2) the measured current increases slightly more than the simulated one.

The first observation is explained in the simulations by the plasma meniscus that becomes more curved with higher extraction field. The meniscus surface is then increasing, allowing more particles to be extracted for a constant plasma density. The second observation suggests that when the plasma meniscus is being pushed further into the plasma, the plasma density increases. This effect is then causing a higher extracted beam current than the expected simulation value when the H^- density in the plasma is assumed to be constant. This variation of density as a function of depth of the plasma has previously been reported from Langmuir probe measurements with similar plasma generators [99, 47].

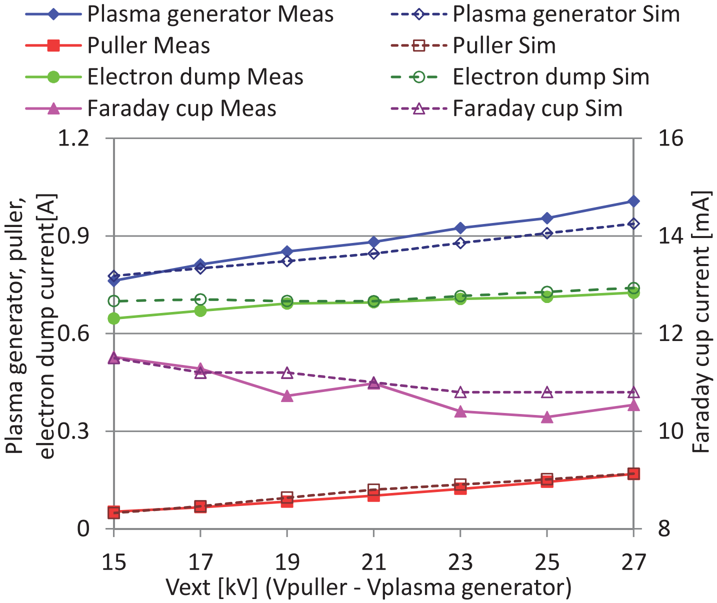

Figure 6.10: Comparison between measurements and simulation with varying puller voltage. The simulation model includes secondary electron emission from the extraction electrodes

As we can see from Figure 6.10, for a low extraction voltage and less extracted total beam current, the H$^-$ beam current in the Faraday cup is the highest. The reason is that the extraction field needs to be adapted to the ion density in the plasma, and shape the plasma meniscus to optimize the beam optics. Figure 6.11 shows two simulation images that correspond to the lowest and highest applied extraction fields. The figure shows that for this measurement, the lowest extraction field gives the best beam transport through the electron dump. We also see that the extraction field should actually be even lower for further improvement.

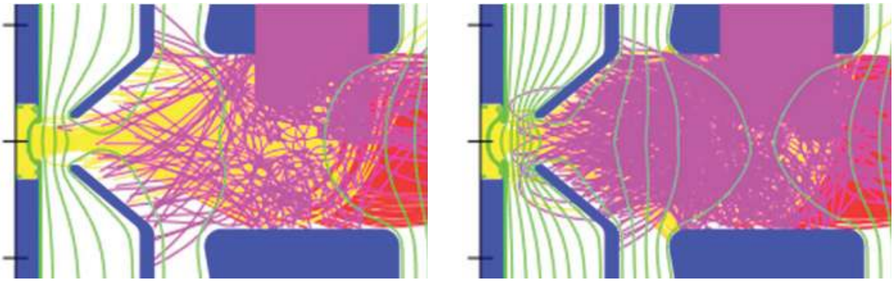

(a) 15 kV extraction voltage.

(b) 27 kV extraction voltage.

Figure 6.11: Two simulation images from the measurement in Figure 6.10. H$^-$ ions are shown in red, primary electrons in yellow, and secondary electrons in pink. The equipotential lines in greens show the shape of the plasma meniscus. For this measurement, the lowest extraction field (15 kV) was best matched to the ion density of the plasma generator. This is seen from the flat plasma meniscus shape and the low amount of secondary electrons emitted from the electron dump.

6.3 Estimation of the e/H$^-$ ratio

An important parameter to quantify for negative hydrogen ion sources is the ratio of co-extracted electrons to H$^-$ ions (e/H$^-$ ratio). This should be a straightforward calculation of the electron dump current divided by the Faraday cup current. However, as we have seen in the previous sections, errors are induced by beam losses and secondary electron emission. By instead calculating the electron current as the difference between the plasma generator current and the Faraday cup current, we obtain a result that is closer to the electron current extracted from the plasma generator. As explained in Section 6.2.2, the plasma generator current includes all the extracted electrons and H$^-$ ions, and is not perturbed by secondary electrons. The e/H$^-$ ratio then becomes

$$e/\mathrm{H}^- = \frac{I_{PG}}{I_{FC}} - 1, \tag{6.1}$$

where I_{PG} and I_{FC} are the currents measured on the plasma generator and Faraday cup, respectively. In the case of H$^-$ beam losses in the extraction system, the relation overestimates the e/H$^-$ ratio.

6.3.1 The e/H$^-$ ratio depends on the plasma electrode potential in the RF-volume source

The DESY plasma generator is equipped with two electrodes close to the extraction hole that can be biased individually relative to the plasma generator (Figure 6.12). In a series of systematic measurements, the currents on the two electrodes and the extracted beam currents have been measured as a function of the voltages applied to the two electrodes. Figure 6.13 shows the current measured on the two electrodes as a function of (1) the collar voltage, (2) the plasma aperture voltage, and (3) the voltage difference between the plasma aperture and collar electrodes. The collar current depends mostly on the collar voltage, and is little affected by the voltage applied to the plasma aperture. The plasma aperture current, on the other hand, depends on both the applied bias voltages, and shows a clear dependency of the voltage difference between the two electrodes.

The plasma aperture electrode is shielded from the reference potential of the plasma generator by the collar electrode. A bias on the collar electrode will thus change the reference potential in the vicinity of the plasma aperture. By biasing the plasma aperture electrode with respect to the collar and measuring the induced current, the plasma properties can then be estimated in a way analogous to a Langmuir probe. The plot in Figure 6.13(b) (as a function of Vp $-$ Vc), shows similarities with a Langmuir I-V curve with the ion saturation region below -25 V, the floating potential at -20 V, the plasma potential at -10 V, and the electron saturation region above -10 V.

Figure 6.14 shows the measured currents in the Faraday cup and on the plasma generator, and the e/H$^-$ ratio as a function of the voltage difference between the plasma aperture and collar electrodes. The Faraday cup current is little affected, but the plasma generator current reduces with a negative plasma aperture bias. The result is a reduction of the e/H$^-$ ratio.

The shape of the e/H$^-$ ratio is similar to the plasma aperture current, which can be explained as follows: When the plasma aperture is biased negatively, negative charges are repelled away from the extraction hole reducing the density of H$^-$ and electrons

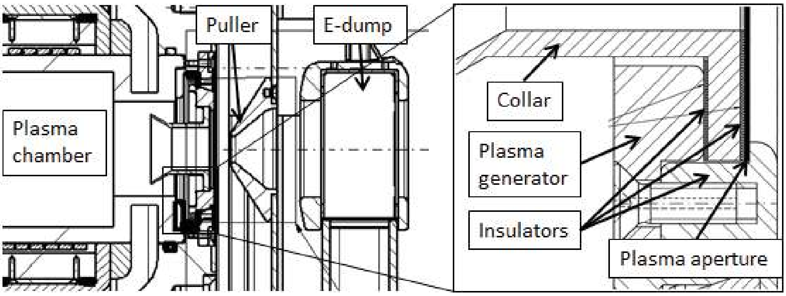

Figure 6.12: Detail of the extraction region. The collar and plasma aperture can be biased independently with respect to the plasma generator potential.

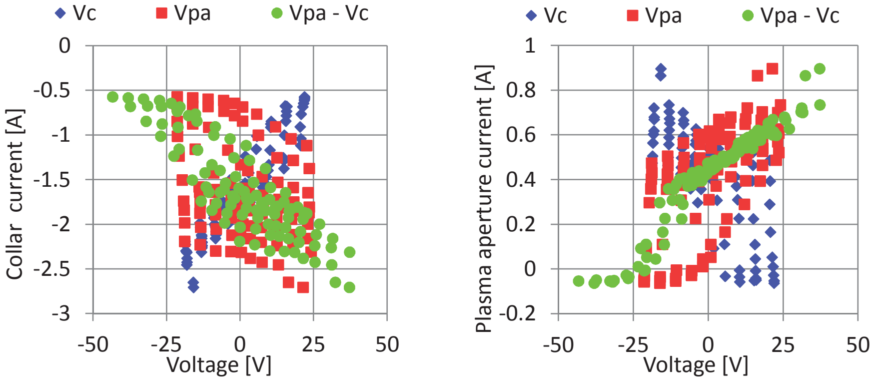

(a) Measured current on the collar electrode.

(b) Measured current on the plasma aperture electrode.

Figure 6.13: Measured currents on (a) the collar electrode and (b) the plasma aperture electrode as a function of (1) the collar voltage (Vc), (2) the plasma aperture voltage (Vpa), and (3) the voltage difference between the plasma aperture and collar electrodes (Vpa − Vc).

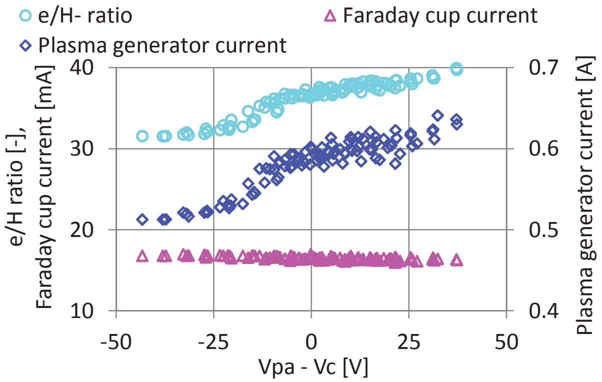

Figure 6.14: e/H$^-$ ratio ($\frac{I_{PG}}{I_{FC}} - 1$), and Faraday cup and plasma generator current as a function of the voltage difference between the plasma aperture and collar electrodes (Vpa − Vc).

in this region. Since the electrons have significantly less mass than the H$^-$ ions, they are strongly affected by this voltage difference, whereas the H$^-$ current remains nearly unchanged. By applying a voltage difference of −30 V, the e/H$^-$ ratio is reduced by 20 %. With a higher voltage difference, the plasma aperture current is in the positive ion saturation region, and there is no more gain.

Figure 6.15 shows measurements from three different days, with no applied extraction voltage on the third day. The shape of the plasma aperture current as a function of the voltage difference of the two electrodes was conserved, also when either of the two electrodes was fixed to the plasma generator potential. This measurement shows that the e/H$^-$ ratio only depends on the plasma aperture voltage with respect to the plasma potential.

6.4 Space charge limited ion beam extraction

The space charge limit of ion beam extraction was introduced with the Child-Langmuir law in Section 4.2.2. As we have seen from measurements described in the previous sections, the extracted beam current does not increase as a function of $V_{ext}^{3/2}$, but it depends linearly on the puller voltage. The reason is that the extraction field is sufficiently large to overcome the space charge limit, and the ion beam current becomes *emission*

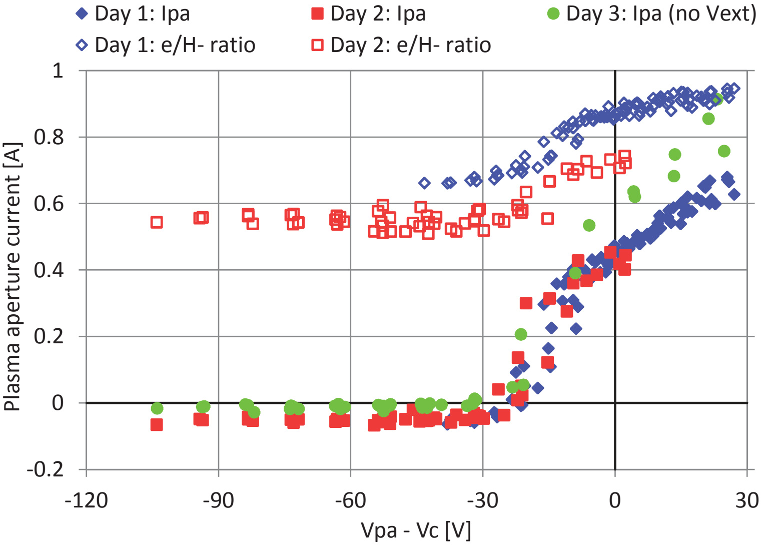

Figure 6.15: e/H$^-$ ratio and plasma aperture current (Ipa) measured at two different days as a function of the voltage difference between the plasma aperture and collar electrodes. The plasma aperture current keeps the same shape independently of the extraction voltage (Vext).

limited, i.e. the ion density in the plasma limits the current.

6.4.1 The RF plasma generator is emission limited

From a measurement made with the DESY plasma generator and a single stage extraction system, the transition between the space charge and emission limited extraction can be visualized. During the commissioning of this ion source at 35 keV, the DC voltage of the plasma generator was ramped up from 0 kV to -35 kV with the RF on. The total extracted current as a function of the extraction voltage is plotted with blue points in Figure 6.16. The red line corresponds to the theoretical space charge limit and has been calculated with Equation 4.42. The e/H$^-$ ratio for this measurement was roughly 40 (or $\sqrt{m_{H^-}/m_e}$), which means that we can rewrite the equation as

$$I_{max} \approx \frac{4}{9}\pi\varepsilon_0 \left(2q\right)^{1/2} V_0^{3/2} \frac{r^2}{d^2} \left(\frac{1}{2\sqrt{m_{H^-}}} + \frac{1}{2\sqrt{m_e}} \right), \tag{6.2}$$

with r = 3.25 mm and d = 6.5 mm. The densities of H$^-$ ions and electrons in the plasma were thus approximately equal during this measurement (from Equation 4.38 we have: $R_{H^-} \approx R_e \approx 1/2$). The measurement shows that the transition between the space charge limited and the emission limited beam extraction corresponds well with the theoretical estimation, and occurs at an extraction voltage of approximately 3 kV.

The green line shows the simulated value of the extracted beam current as a function of the plasma generator voltage. As the extraction voltage approaches 0 V, there is approximately 400 mA being extracted from the plasma generator, whereas the measured value becomes zero. In the simulation, the charged particles are given an initial energy of 5 eV towards the plasma aperture as described in Section 5.3.1. Even with no accelerating extraction field, the charges drift out of the plasma aperture, expanding the plasma meniscus and the ion beam. In this region it is therefore difficult to estimate the H$^-$ and electron current densities that are available from the plasma generator.

6.4.2 The magnetron is space charge limited

The magnetron ion source was presented in Section 5.2.3. The extracted H$^-$ beam current measured at BNL yielded 140 mA, and showed similarities with a dependency of the extraction voltage to the power of 3/2. We will now compare this result with simulations.

Figure 6.17 compares (1) the measured H$^-$ beam current with a Faraday cup, (2) the theoretical space charge limit of total extracted H$^-$ current, and (3) two simulations of

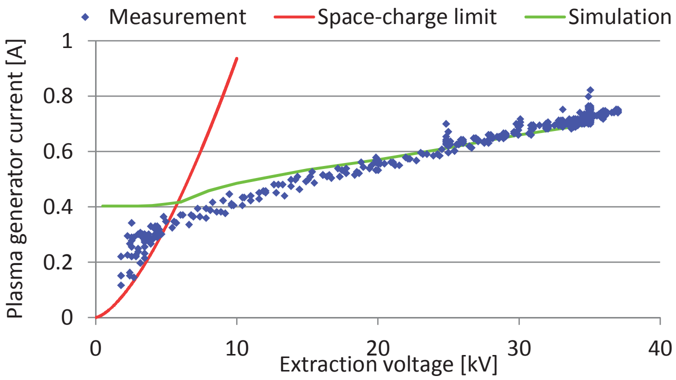

Figure 6.16: Blue points: total extracted beam current from the DESY plasma generator with a single stage extraction system as a function of the extraction voltage. The transition between space charge limited and emission limited beam extraction is located approximately at an extraction voltage of 3 kV. Red line: space charge current limit for assumed equal densities of H^- ions and electrons. Green line: simulation of the extracted current as a function of the extraction voltage.

the extracted H$^-$ beam current with different input current densities. The total extracted beam current from the plasma generator was not measured. The space charge limit curve has been calculated with Equation 4.42 using an e/H$^-$ ratio of 1, and with the dimensions of the magnetron ion source, i.e. $r = 2$ mm and $d = 5$ mm. The plotted curve includes only the contribution of H$^-$ ions, but the electrons are nevertheless included in the calculation, as well as in the simulations. The two simulations have used input densities of H$^-$ ions to reach beam currents of 50 mA and 200 mA extracted through a circular plasma aperture with a radius of 2 mm.

We observe that the measured Faraday cup current looks to be space charge limited because of the similar shape as the theoretical space charge limit. We also see that the simulated extracted beam currents stay at a constant value with an extraction voltage below the space charge limit, as we also observed for the measurement described in Section 6.4.1. With an extraction voltage below 20 kV, the current that reach the Faraday cup is similar even for a high (200 mA) or low (50 mA) simulated H$^-$ beam current. Above 20 kV, we see that only the highest simulated beam current follows the Faraday cup measurement. Because the ion source does not reach the emission limited extraction mode for the measured range of extraction voltages, it is difficult to estimate the H$^-$ and electron current densities that are available from the plasma generator.

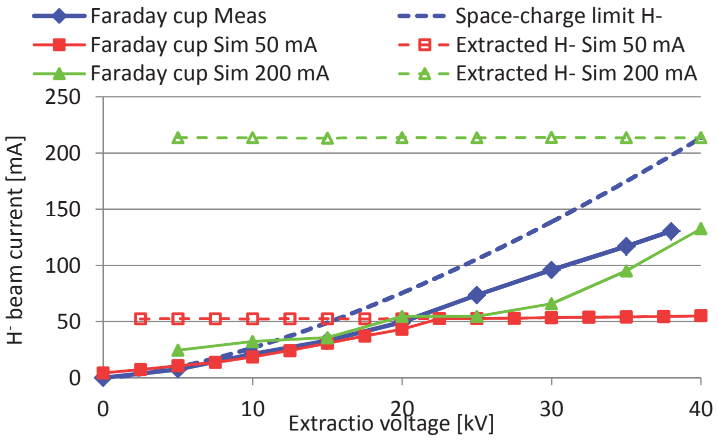

Figure 6.17: Comparison of a magnetron measurement, theoretical space charge limit of extracted H$^-$ current, and simulations with two different current densities.

Figure 6.18(a) shows an image from a simulation with a high current density (i.e.

200 mA through an aperture of 4 mm diameter) and with an extraction voltage of 40 kV. All the electrons are here deflected and dumped on the puller, and parts of the H^- beam are lost on the puller. Traces of the impacting particles on the puller have been confirmed by post-mortem observation, as shown in Figure 6.18(b).

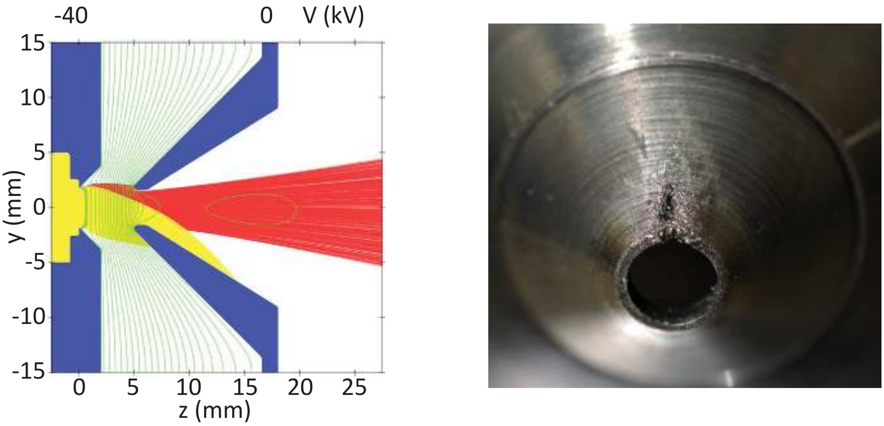

(a) Simulation of the magnetron beam extraction with 200 mA H^- beam current, and an extraction voltage of 40 kV.

(b) Picture of the magnetron puller electrode after a few days of testing. The traces originate from the deviated electron beam and the outer parts of the H^- beam.

Figure 6.18: Simulation of the magnetron ion source with an e/H^- ratio of 1. The beam extraction is space charge limited, and parts of the H^- beam are lost on the puller.

6.5 Measurements with a positive ion beam

The commissioning of other accelerator parts of Linac4 such as the RFQ will require a high intensity beam. In the case that the ion source cannot deliver a high intensity H^- beam in time, there is an option to switch polarity of the extraction electrodes, and extract a proton beam instead.

Figure 6.19 shows the results from a beam measurement made with the IS01 plasma generator with the extraction system polarities adapted for a positive ion beam. The figure compares measurements and simulations of the currents on the extraction system electrodes, and in the Faraday cup as a function of the RF-power transmitted to the plasma (i.e. the incident minus the reflected power). The simulation input current density of protons has been linearly scaled to this RF-power. In the simulations, the input beam includes the fractions of H_2^+ and H_3^+ that was measured with the DESY plasma generator (80 % p^+, 10 % H_2^+, and 10 % H_3^+), and the simulation model includes secondary electron emission from the electrode surfaces.

The current measured on the plasma generator and the Faraday cup in Figure 6.19 corresponds well with the simulated values. The currents measured on the puller and electron dump have not been reproduced in the simulations. These measured currents are of approximately same magnitude (50 mA) with opposite signs, and suggests that there was a current flowing between the two electrodes. The puller received positive charges and/or emitted negative charges, and this could be caused by the ion beam scraping the inside of the electrode causing a large fraction of secondary electrons because of the incident angle. These electrons could then travel to the electron dump, which has a higher applied potential.

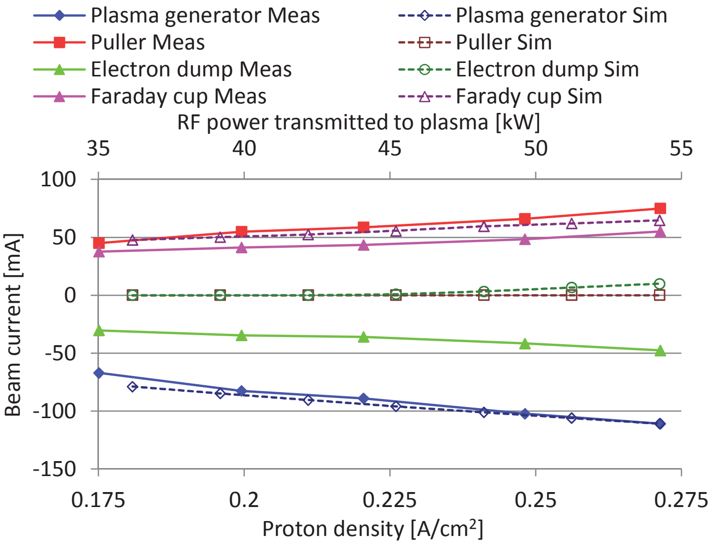

Figure 6.19: Comparison between measurements of currents on the extraction system electrodes and simulations with varying RF-power for a positive ion beam extraction. The RF-power on the x-axis has been linearly scaled to match the H^- density used as input in the simulations, and the simulation model includes secondary electron emission.

Figure 6.20 compares measurements and simulations of the plasma generator and Faraday cup currents with an RF-power of 50 kW. The measurement shows that with a higher extraction field, the beam transmission through the extraction system increased. The proton current yielded 60 mA. To arrive at higher beam currents, a redesign of the extraction system is necessary. The reason is shown in the simulation image in Figure 6.21. The image shows the highest simulated transmission of the positive ion beam with an RF-power of 50 kW. Parts of the beam are lost both on the electron dump, and at the LEBT entry. A higher extraction field would reduce the beam losses in the electron dump, but more beam would be lost on the LEBT entry. The opposite effect applies for a reduction of the extraction field. The space charge of the beam consisting of 80 % p^+, 10 % H_2^+, and 10 % H_3^+, is thus too high for this extraction system.

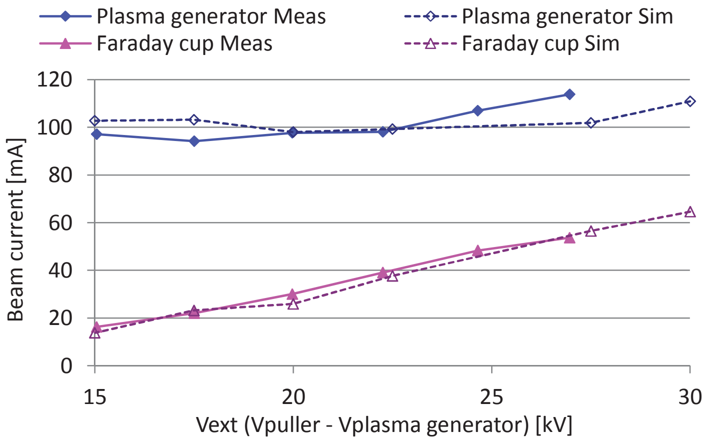

Figure 6.20: Comparison between measurements and simulations of the currents on the plasma generator and the Faraday cup as a function of the extraction voltage for a positive ion beam extraction with an RF-power of 50 kW.

6.6 Analysis and improvements of the ion beam optics

Measurements of the H^- ion beam extraction system fit well with simulations, and the first challenge has been achieved: to extract a 45 keV H^- ion beam. However, the beam current and emittance still needs to be improved to reach the Linac4 requirements. This

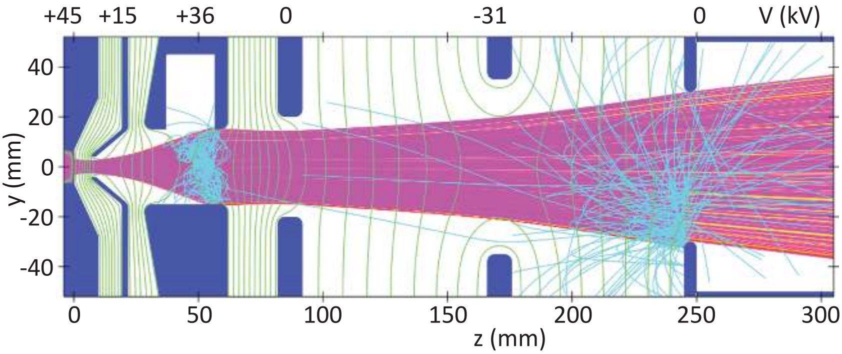

Figure 6.21: Simulation image of a proton beam extraction. The trajectories of p^+ (red), H_2^+ (yellow), and H_3^+ (pink) overlap each other because they in electrostatic devices depend on the energy per charge, and not on the charge-to-momentum ratio. Secondary electrons are shown in light blue.

section presents some of the limitations of the extraction system, and suggestions of how to address these challenges.

6.6.1 The beam intensity is limited by the plasma generator

The ion beam intensity is correlated with the beam emittance. In order to reach higher transported beam intensities, one could increase the size of the plasma aperture to extract more current. On the other hand, as the minimum emittance (Equation 3.12) is proportional to the plasma aperture radius, this would counteract the effect. In addition, a large beam size compared with the bore sizes of the extraction electrodes, causes aberrations in the beam that results in an increased rms emittance.

An increased extraction voltage increases the beam current, but also lowers the beam quality as the plasma meniscus becomes more concaved shaped. This effect then needs to be counteracted by increasing the RF-power of the plasma generator, and thus increasing the plasma ion density. The limiting factor is thus the plasma generator ion production capability.

Lowering the amount of co-extracted electrons would help on both the H^- ion intensity, and the emittance. Achieving this would require improving the plasma generator, e.g. by introducing caesium as a catalyst for surface production of negative ions.

6.6.2 The emittance growth in the extraction system has to be minimized

Keeping the emittance within 0.25 μm is a challenging requirement. As the beam travels through the extraction system, the emittance cannot decrease. The emittance growth has to be limited by optimizing the extraction system design, and omitting elements that cause beam aberrations. For instance, the magnetic fields of the plasma generator filter and the electron dump will induce emittance growth due to ion beam disorder, and by steering the beam off-axis.

When the beam is extracted from the plasma, it has a minimum emittance given by Equation 3.12. In the case of a plasma aperture of 6.5 mm diameter aperture that was installed in the tested plasma generators and an ion temperature of 1 eV that was used as input in the simulations, $\varepsilon_{N,rms} = 0.053$ μm. Most of the emittance at the LEBT entry is thus caused by emittance growth in the extraction system.

Plasma aperture

In Section 4.2.5, we saw how the shape of the plasma electrode influenced the shape of the plasma meniscus, and possibly reduced the ion beam emittance. By applying an angle to the plasma electrode of 65°, the emittance was reduced by more than a factor two in the given example. This plasma electrode shape is implemented in both IS01 and IS02, and was already present in the magnetron design.

Electron dump

The electron dump has been designed to dump the electrons at low energy to avoid sublimation of the electron dump surface material by the impacting electron beam. The drawback of this solution is that the space charge driven emittance growth is larger at low energies. The co-extracted electrons cause additional emittance growth before they are removed from the H^- beam. Figure 6.22 illustrates this effect by comparing a normal beam extraction simulation with a simulation where the electrons have been artificially removed at the puller electrode. Both simulations have been made with an input H^- beam current of 30 mA and an e/H^- ratio of 30.

Figure 6.23 shows the normalized rms emittance as a function of the distance in the extraction system. Before entering the magnetized Einzel lens electron dump, the emittance stays constant, whereas at the exit it is > 2.5 times the input value (blue trace). Since the beam at this stage includes electrons, the electron space charge will also contribute to the emittance growth. Plotted in red is the emittance for a simulation where

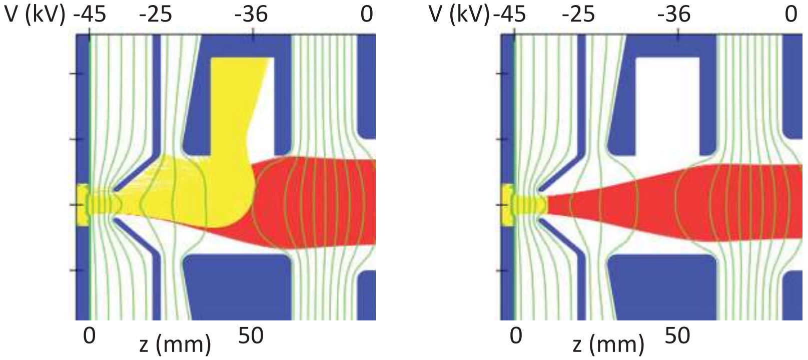

(a) Simulation image of the normal beam extraction.

(b) Simulation image with artifical removal of electrons before the beam enters the electron dump.

Figure 6.22: Simulation images of 30 mA H^- beam current with an e/H^- ratio of 30.

the electrons have been artificially removed from the beam before entering the electron dump. The electrons are still included in the first part to have the same conditions for the plasma extraction in both simulations. For the second simulation, the emittance growth is much less (about a factor 1.6), and shows that reducing the amount of co-extracted electrons will lead to reduced emittance.

We notice that the normalized rms emittance is decreasing at the exit of the electron dump. This is due to an artefact from the normalization of the emittance. The beam energy has been assumed to correspond to the voltage on the beam axis. However, since the equipotential lines curve into the electron dump, the outer particles actually have less energy than the ones located on the beam axis. The velocity of these particles will then be over-estimated, and because they have higher transverse velocities, the calculated emittance will be too high in this region. In the regions where the equipotential lines are perpendicular to the beam axis, the normalization of the emittance is correct.

Accelerating vs. decelerating Einzel lens

Einzel lenses can operate in either accelerating or decelerating mode. For a given absolute voltage on the lens, the decelerating mode produces more focusing, but can lead to larger emittance growth. For this reason the accelerating lens is normally preferred. For the Linac4 ion source, however, the choice needs to consider the emittance growth in the LEBT. In the end it is the emittance at the RFQ entry that counts, and the beam shape

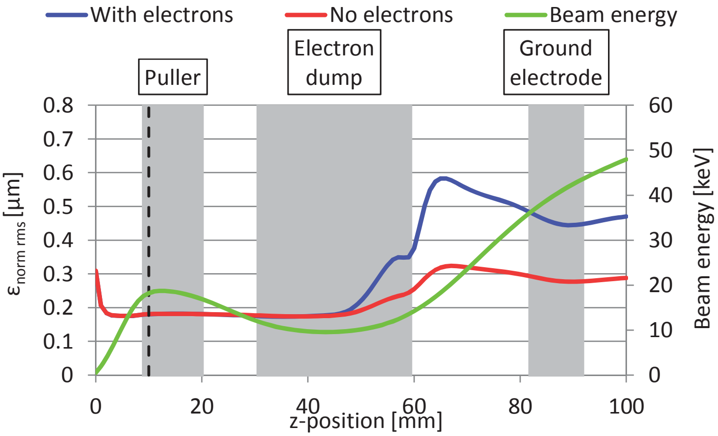

Figure 6.23: Comparison of a normal beam extraction, and a simulation where the electrons has been artificially removed at the dashed line. The green line shows the beam energy along the z-axis and the coloured areas indicate the locations of the puller, the electron dump, and the ground electrode.

out of the extraction system influences the emittance growth in the optical elements of the LEBT. Figure 6.24 shows two beam extraction simulations tracked through from the plasma generator through the first solenoid of the LEBT. The simulations only differ with the polarity of the Einzel lens voltage. As we can see, the beam size for the accelerating Einzel lens is larger, and the beam passes very close to the beam pipe wall.

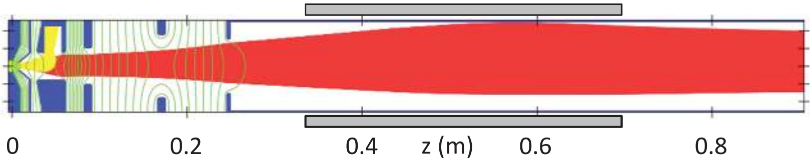

(a) Beam extraction with accelerating Einzel lens.

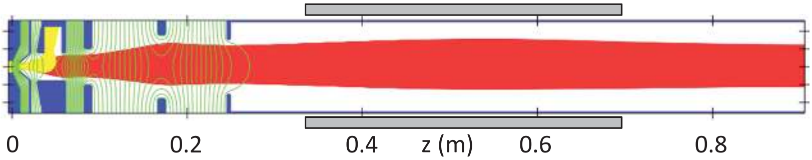

(b) Beam extraction with decelerating Einzel lens.

Figure 6.24: Comparison of accelerating and decelerating Einzel for a simulated H^- beam current of 30 mA with an e/H^- ratio of 30. The first solenoid of the LEBT is shown in grey.

Figure 6.25(a) shows the evolution of the emittance as a function of the position in the extraction system. We observe that the beam from the decelerating lens enters the solenoid with double the emittance of the accelerating Einzel lens beam. However, the emittance values are closer at the exit. In Figure 6.25(b), we see that the beam coming from the decelerating Einzel lens has lower beam size as it passes through the solenoid.

The reason for the differences in emittance growth inside the solenoid is due to the non-uniformity of the magnetic field. The field strength in the solenoid increases as one move away form the beam axis, making the particles close to the wall encounter a stronger field. This spherical aberration of the solenoid lens causes an emittance growth. For this particular ion beam extraction system, the polarity of the Einzel lens results in the same emittance after the beam has passed through the solenoid. A solution of reducing the emittance is to move the solenoid closer to the plasma generator, and to remove the Einzel lens.

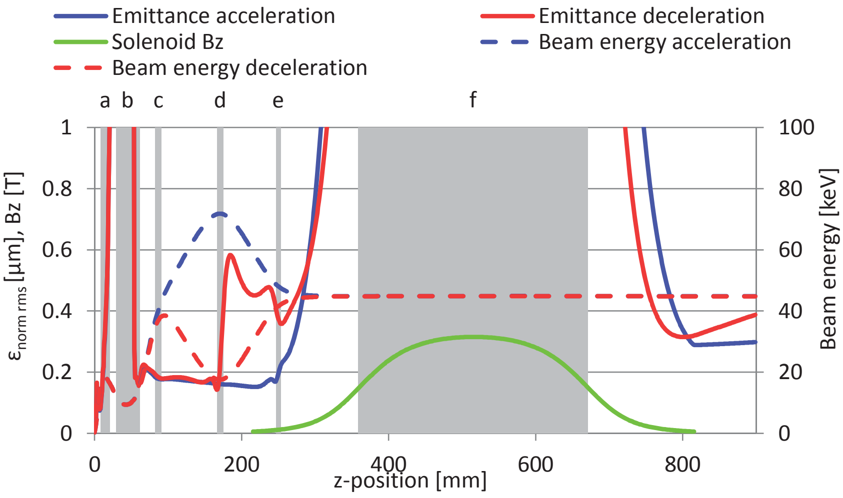

(a) Comparison of the emittance as a function of the position in the extraction system, for simulations with accelerating and decelerating Einzel lens.

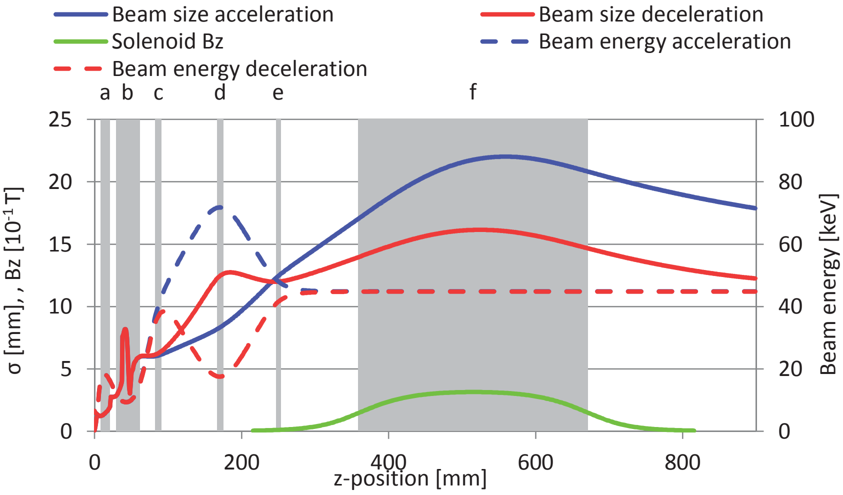

(b) Comparison of the beam size as a function of the position in the extraction system, for simulations with accelerating and decelerating Einzel lens.

Figure 6.25: Evolution of the emittance and the beam size along the beam axis for an accelerating (blue) and decelerating (red) Einzel lens. The beam energy is plotted in dashed lines, and the solenoid axial field in green. The grey areas indicate: (a) the puller, (b) the electron dump, (c) the ground electrode, (d) the Einzel lens, (e) the LEBT entry, and (f) the solenoid.

6.6.3 The electron dumping changes for different plasma generators

The purpose of the electron dump is to dump the electrons without sublimating the electron dump material. It should also collect all the co-extracted electrons for a precise measure of the e/H$^-$ ratio and thus the plasma generator performance. The e/H$^-$ ratio is of particular importance to follow the evolution of the caesiated surface plasma generator. We have previously seen (Section 6.2.2) that secondary electrons are emitted from the dump, which makes the measured current lower than the electrons current that is impinging the electron dump. The design of the electron dump could be improved to prevent secondaries form escaping. For instance, stronger permanent magnets with larger separation would create a more uniform dipole field inside the magnetized Einzel lens.

An unexpected result of the beam extraction from the IS02 plasma generator was that the electron dump current was close to zero, whereas the puller collected most of the current. A measurement plot from IS02 is shown in Figure 6.26, where the currents in the extraction system are plotted as a function of the extraction voltage. We see that the plasma generator current increased linearly with the extraction voltage, which implies that the ion source was operating in the emission limited mode. We also observe that the optimum extraction voltage was approximately 15 kV for a maximum H$^-$ beam current of 18 mA, measured in the Faraday cup.

When it comes to the puller and electron dump currents, we see that almost all the current hits the puller. The reason comes from the filter field inside the IS02 plasma generator. In order to make space for the surface production converter inside the plasma generator, the filter magnets were moved outside the plasma chamber, as was shown in Figure 5.13. To reach the same magnetic field strength on the axis as the DESY and IS01 plasma generator, stronger magnets were used. A comparison of the filter field strengths along the z-axis for the DESY, IS01 and IS02 plasma generators is shown in Figure 6.27. We see that the filter field of IS02 has a magnitude of about 10 mT at the plasma aperture, and cause an immediate deflection of the electrons after extraction.

Figure 6.28 shows a simulation image with an extraction voltage of 15 kV including secondary electron emission. The deflected electrons hit the sidewall of the electron dump instead of inside the cup. The secondary electrons are then accelerated by the electric field and hit the puller. From the plot in Figure 6.26, we can see the transition when the puller voltage has a lower voltage than the electron dump ($V_{ext} < 9$ kV). The puller then repels the secondary electrons, and the electron dump measures an increased current.

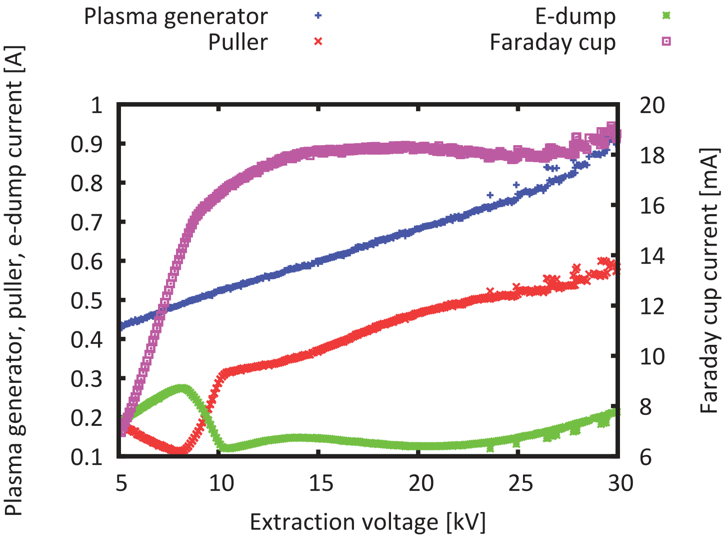

Figure 6.26: Measured beam currents extracted from the IS02 plasma generator as a function of the extraction voltage.

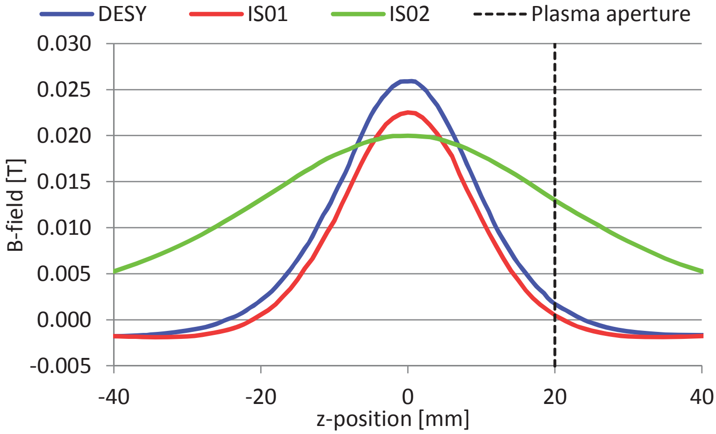

Figure 6.27: Simulated filter field strengths for the DESY, IS01 and IS02 plasma generators along the z-axis.

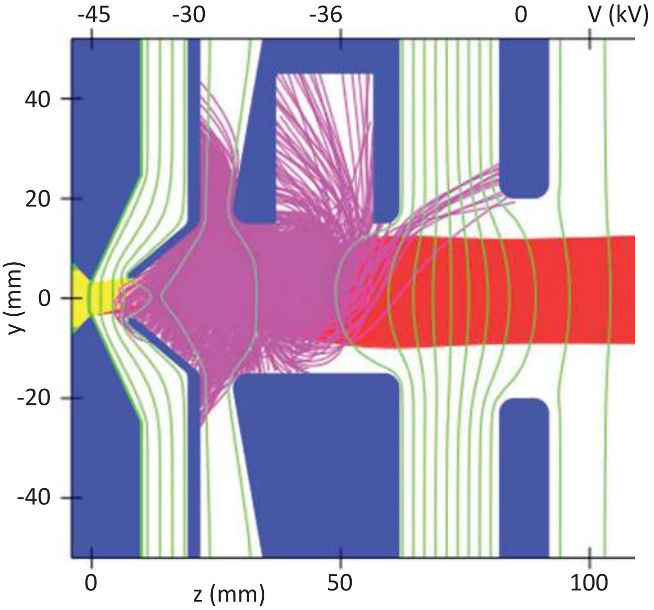

Figure 6.28: Simulation image for a beam extraction with IS02. The filter field inside the plasma generator deflects the electrons (yellow) immediately after being extracted. Secondary electrons (pink) emitted form the electron dump are collected on the puller.

Collecting the co-extracted electrons on the puller should be prevented first and foremost because its power supply is not designed to handle the high current. A simple solution is to install plates of magnetic steel on the plasma generator facing the extraction region. These plates would then shield off the magnetic field from the extraction region. Alternatively, the extraction system can be redesigned to extract the ion beam at low energy by connecting the electron dump power supply to a combined puller and electron dump electrode [100]. The filter field would then deviate the electrons onto the puller dump with the help of an additional dipole if necessary.

Chapter 7

Conclusion

Within the framework of this thesis, a new beam excitation system was designed, produced and commissioned for the 2 MHz RF negative hydrogen (H^-) ion source for Linac4 as part of CERN's injector chain upgrade. Key features of the extraction system include a tuneable puller voltage that adapts the extraction field to the ion plasma density for optimum beam optics, and a magnetized Einzel lens for electron dumping and focusing of the H^- ion beam.

The extraction system was developed by combining theories of beam extraction from a plasma and beam transport at low energy, together with simulations of the beam extraction and estimation of the power density on the electron dump with the plasma extraction code IBSimu [1]. The most important achievement was to reliably extract the H^- beam at 45 keV with up to 2 A of co-extracted electrons without causing high voltage breakdowns, which was previously not possible with a single stage extraction system. The H^- beam current yielded a maximum of 60 mA, extracted from the caesiated IS02 plasma generator, and stable beam currents of 35 mA were recorded for a period of two months.

7.1 Summary of extraction system characterization

The measured currents on the excitation system electrodes and in the Faraday cup verified and benchmarked the simulations. The measurements and simulations values corresponded well and helped to identify the locations of beam losses, and which parts of the beam extraction system needed further improvement. Including secondary electron emission from electrode surfaces to the simulation model allowed us to better understand the beam measurements.

7.1.1 Ion source performance

The matching of ion source prototypes to the Linac4 requirements was assessed at the ion source test stand. The ion source produced a stable and reliable 45 keV H^- ion beam with a beam extraction system that was adaptable for variations of the beam current densities supplied by the plasma generator. This extraction system no longer suffered from the high voltage breakdowns that were frequently observed with a single stage extraction system, and the ion source can run for $\sim$100 hours between faults.

There is still a need for improvement since the measured beam intensity was lower than the required 80 mA. 60 mA was reached, but only for a period less than 1 day. To achieve the final goal, both the plasma generator and the extraction system need to be upgraded. The emittance was measured to 0.37 µm for a beam current of 50 mA, when calculated with the standard 10 % thresholding of the signal. The Linac4 requirement is 0.25 µm. A comparison of the ultimate Linac4 requirements and what has been measured with a caesiated RF ion source at the test stand is summarized in Table 7.1.

Table 7.1: Linac4 ion source requirements [20] and achieved values at the test stand with the new extraction system and a caesiated plasma generator (IS02).

Parameter	Linac4	Test stand
Beam energy [keV]	45	45
Pulse length [ms]	0.5	0.5
Repetition rate [Hz]	2	0.8
H^- current [mA]	80	50
$\varepsilon_{\mathrm{norm,rms}}$ [µm]	0.25	0.37

7.1.2 Correspondence between measurements and simulations

The extraction system performance was characterized by measuring the current in four locations as a function of RF power and the puller electrode voltage, and these measurements were compared with simulations. The simulation output matched all of the measured values to within a few percent after selection of the best fitting H^- and electron current densities, when secondary electron emission by particle impact on the electrode surfaces was included. Tuning the puller voltage in order to match the extraction field to the plasma density can optimize the beam optics.

7.1.3 Plasma generator e/H$^-$ ratio

The e/H$^-$ ratio was measured via the ratio of the plasma generator and Faraday cup currents ($e/\mathrm{H}^- = \frac{I_{PG}}{I_{FC}} - 1$). The result is a slight over-estimation because it is not including H$^-$ losses. By applying a negative bias on the plasma aperture electrode of the DESY plasma generator, the e/H$^-$ ratio was reduced by 20 %.

7.1.4 Space charge limited beam extraction

Whereas the RF-source operated in emission limited mode, the magnetron ion source extraction was space charge limited as observed from measurements performed at BNL. The IBSimu simulations corresponded well to the measurements, when the extraction voltage was high enough to overcome the space charge limit (i.e. $V_{ext} > 3$ kV for the DESY RF source with an extraction gap of 6.5 mm.).

A challenge of the magnetron source is to achieve a high beam current with a low extraction field. The reason is to avoid damage of the puller material by electron beam impact. With the present extraction system design, a high extraction voltage is necessary to reach a high beam current. It would, however, be an advantage to extract the beam in the emission limited mode. In this way, the plasma meniscus surface would be concave, providing the beam a focus into the puller. The situation now is that the beam is diverging out of the plasma aperture, and the H$^-$ beam is collimated through the puller. When operating in emission limited mode, an increase of the current density can also be adjusted by increasing the extraction voltage.

In order to reach the emission limited mode with the magnetron source, the electric field has to be increased by either decreasing the extraction gap or increasing the extraction voltage and potentially use an accel-decel beam extraction. The former is the preferable option because the increased energy of the electrons would cause more damage to the puller electrode, which is being used as an electron dump in the magnetron ion source.

7.1.5 Positive ion beam extraction

A 60 mA proton beam was extracted and transported from the IS01 plasma generator. To arrive at higher beam currents, a redesign of the extraction system is necessary, inp articular because the dumping electrode reduces the beam energy causing a large space charge induced beam growth.

7.2 Further improvements of the ion beam extraction system

In order to achieve higher beam currents and lower emittance of the Linac4 H^- ion source, the following points can be addressed:

- Reduce the length of the extraction system to keep a small beam emittance and beam size into the first solenoid of the LEBT.
- Install a plasma aperture electrode with an angle that shapes the electric field lines and reduce the beam emittance.
- Study the focal effect of the electrode geometries such as angles, positions, and aperture sizes.
- Keep the e/H^- ratio as low as possible by caesiation of the converter surface in the plasma generator.

The use of a good simulation tool such as IBSimu is essential for the development of new extraction system designs. Batch processing automatizes the simulations and allows fast systematic parametric studies of both the excitation system design and for the reproduction of beam measurements.

Appendix A

Symbols and relations

A.1 List of abbreviations

BINP	Budker Institute of Nuclear Physics
BNL	Brookhaven National Laboratory
BCT	Beam Current Transformer
CERN	European Organization for Nuclear Research
DESY	German Electron Synchrotron
DTL	Drift Tube Linac
ECR	Electron Cyclotron Resonance
IPP	Max Planck Institute of Plasma Physics
JYU	University of Jyväskylä
LEBT	Low Energy Beam Transport
LHC	Large Hadron Collider
PS	Proton Synchrotron
PSB	Proton Synchrotron Booster
RAL	Rutherford Appleton Laboratory
RF	Radio Frequency
RFQ	Radio Frequency Quadrupole
SNS	Spallation Neutron Source
SPL	Super Proton Linac
SPS	Super Proton Synchrotron

A.2 List of symbols and constants

Symbol	**Description**	**Unit**
A	mass number	
A_e	electron affinity	eV
α	Twiss alpha	
$\mathbf{B}$	magnetic flux density	T
β	Twiss beta	m
$\mathbf{E}$	electric field	V m^{-1}
E	energy	eV
E_a	electron affinity	eV
E_i	ionization energy	eV
ε	Emittance	µm
$\mathbf{F}$	force	kg m s^{-2}
f	frequency	s^{-1}
γ	Twiss gamma	m^{-1}
I	current	A
J	current density	A m^2
$\mathcal{L}$	luminosity	$\text{cm}^{-2}\text{s}^{-1}$
λ_D	Debye length	m
m	mass	kg
N	number	
n	density	m^{-3}
ν	collision frequency	s^{-1}
Φ	potential	V
Q	synchrotron tune	
ΔQ	incoherent space charge tune shift	
q	charge	C
$q\pm$	charge state	
σ	cross section	m^2
$\sigma_{x,y}$	transverse beam size	m
T	temperature	K or °C
t	time	s
$\mathbf{v}$	velocity	m s^{-1}
v	speed	m s^{-1}
W	work function	eV
ω	oscillation frequency	s^{-1}

Constants

c	Speed of light	2.998×10^{8} m/s
e	Elementary charge	1.602×10^{-19} C
ε_0	Permittivity of free space	8.854×10^{-12} m^{-3} kg^{-1} s^{4} A^{2}
k	Boltzmann's constant	1.381×10^{-23} m^{2} kg s^{-2} K^{-1}
m_e	Electron mass	9.109×10^{-31} kg
m_p	Proton mass	1.673×10^{-27} kg

Relativistic parameters

$\beta = v/c$

$\gamma = \left(1-\beta^2\right)^{-1/2}$

Appendix B

Mathematical relation for work function changes

The work function of a material, W, can be reduced by covering the surface with a thin layer of an alkali metal. We express the work function as

$$W = W_0 - \Delta W_m, \tag{B.1}$$

where W_0 is the intrinsic work function of the base material surface, and W_m the maximum reduction of the material work function. W_m has been described by the following semi-empirical formula [40]:

$$\Delta W_m \simeq 0.62\,(E_i + E_a) - 1.24 W_0, \tag{B.2}$$

where E_i and E_a are the ionization energy and electron affinity of the adsorbate respectively. Here we see that the lowest sum of E_i and E_s gives the largest reduction of the work function. Caesium is then the best candidate as adsorbate with E_i + E_s = 4.37 eV.

The material work function can also be described as a function of relative coverage, $W(\theta)$. The result is a polynomial fit that has shown good agreement with measurements [40]:

$$W(\theta) \simeq W_0 + \frac{6\Delta W_m}{(3-\theta_m)\theta_m}\theta - \frac{3\Delta W_m(\theta_m + 1)}{(3-\theta_m)\theta_m^2}\theta^2 + \frac{2\Delta W_m}{(3-\theta_m)\theta_m^2}\theta^3, \tag{B.3}$$

where θ_m is the fractional coverage that gives the minimum material work function. θ_m needs to be found experimentally, and is normally located around 0.6 [38, 101]. This polynomial fit shows that for a full monolayer, the change in material work function is:

$$\Delta W_1 = \frac{3\theta_m - 1}{3 - \theta_m} \frac{\Delta W_m}{\theta_m^2}. \tag{B.4}$$

For one monolayer of caesium deposited on molybdenum, the work function estimated by this relation is 1.8 eV, which has been confirmed experimentally [38]. The work function of a molybdenum surface as a function of the fractional coverage of caesium is shown in Figure 3.17.

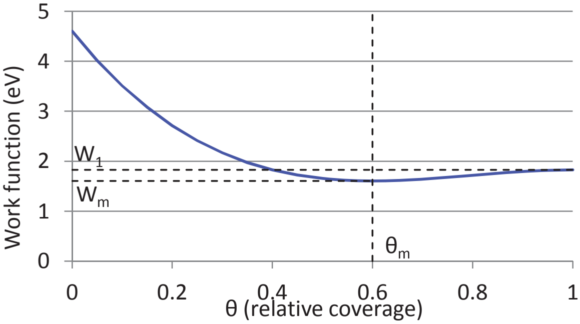

Figure B.1: Work function of a molybdenum surface with a fractional coverage of caesium

Appendix C

Collection of publications

C.1 A new extraction system for the Linac4 H^- ion source

This paper presents the commissioning of the non-caesiated 2 MHz DESY H^- volume source. This ion source was not able to produce a 45 keV H^- beam, which is the requirement of the Linac4 3 MeV RFQ, because of evaporated material from the electron dump in the single stage extraction system. Two new extraction systems were proposed, and the decision was to build a new extraction system with a magnetized Einzel electron dump.

The candidate was the main author of this paper and presented the results with a poster at the International Conference on Ion Sources 2011. The candidate simulated the beam extraction from the DESY source, and the second proposal of a new extraction system. This extraction system was chosen as the baseline for the new ion source at CERN. The simulation of the first proposal was made by M. Kronberger.

REVIEW OF SCIENTIFIC INSTRUMENTS **83**, 02B710 (2012)

A new extraction system for the Linac4 H^- ion source[a)]

Ø. Midttun,[1,2,b)] T. Kalvas,[3] M. Kronberger,[2] J. Lettry,[2] H. Pereira,[2] C. Schmitzer,[2] and R. Scrivens[2]
[1]*University of Oslo, P.O. Box 1048, 0316 Oslo, Norway*
[2]*CERN, 1211 Geneva 23, Switzerland*
[3]*Department of Physics, University of Jyväskylä, P.O. Box 35, FI-40014, Finland*

(Presented 12 September 2011; received 10 September 2011; accepted 23 October 2011; published online 13 February 2012)

As part of the CERN accelerator complex upgrade, a new linear accelerator for H^- (Linac4) is under construction. The ion source design is based on the non-caesiated DESY RF-driven ion source, with the goal of producing an H^- beam of 80 mA beam current, 45 keV beam energy, 0.4 ms pulse length, and 2 Hz repetition rate. The source has been successfully commissioned for an extraction voltage of 35 kV, corresponding to the one used at DESY. Increasing the extraction voltage to 45 kV has resulted in frequent high voltage breakdowns in the extraction region caused by evaporating material from the electron dump, triggering a new design of the extraction and electron dumping system. Results of the ion source commissioning at 35 kV are presented as well as simulations of a new pulsed extraction system for beam extraction at 45 kV. © *2012 American Institute of Physics*. [http://dx.doi.org/10.1063/1.3670344]

I. LINAC4 ION SOURCE COMMISSIONING

The new Linac4 ion source is based on the non-caesiated, 2 MHz DESY H^- volume source,[1] shown in Fig. 1. The gas is injected by a pulsed piezo-electric valve from the back side into a spark gap, triggering the ignition of the plasma. The plasma is heated by an external solenoidal RF antenna and confined in an Al_2O_3 ceramic plasma chamber by a dodecapole multicusp magnetic field. A magnetic filter field separates the plasma into two regions, creating a low electron energy plasma in the collar for enhanced H^- production. The negative ion beam is extracted over a 8.5 mm gap and the co-extracted electrons are deflected and dumped in a graphite cup by a permanent dipole magnetic field, whereas an opposite dipole field corrects the deviation of the H^- beam.

The commissioning of the source was completed for an extraction voltage of 35 kV in 2009, achieving stable pulsed beam operation with a current of 23 mA.[2] When increasing the extraction voltage to 45 kV, which is the requirement for a correct matching to the radio frequency quadrupole (RFQ), it was no longer possible to hold the voltage over the extraction gap for more than a few beam pulses. Inspection of the electron dump showed great damage on the graphite surface from the electron beam impact, and it was concluded that the evaporated material caused the high voltage breakdowns. The damage on the graphite dump had also been observed when operating at 35 kV, however, as the breakdowns were much less frequent (15 per 24 h), it was believed to be a problem of high voltage training.

In order to be on schedule for the commissioning of the RFQ, the source is producing a 45 keV proton beam by inverting the polarity of the extraction voltage. It is worth mentioning that during the proton beam tests, the high voltage breakdown rate has been approximately 1 per 24 h, which is consistent with the dumping of the electrons and evaporation of dump material being the cause of the breakdowns when H^- is extracted.

II. SIMULATIONS OF THE LINAC4 H^- SOURCE

The negative ion beam extraction of the Linac4 ion source has been simulated with IBSimu (Ref. 3) for verification and understanding the observations resulting from the source commissioning. For this simulation, a set of plasma parameters have been chosen, which are believed to give good agreement between simulations and measurements. The most important being the transverse temperature ($T_t = 0.5$ eV) and the initial energy ($E_0 = 5.0$ V) of ions and electrons. The negative ion beam current has been set to 30 mA with an electron to H^- (e/H) ratio of 50. These parameters have been kept constant in all simulations shown in this paper if otherwise is not stated.

Simulations of the extracted H^- beam have shown good agreement with emittance measurements, giving confidence in the simulation tool and chosen plasma parameters for further improvement of the ion source. Fig. 2 compares the state of the graphite cup used in the electron dump after the 35 kV commissioning with a simulation showing the surface power density of a 1.5 mA electron beam impact. The power distribution following from the simulation coincides well with the finding from the commissioning. A peak power density of 1.8 kW/mm^2 is reached in the middle of the cup at the same position as the hole from the electron beam. Transient thermal simulations made with ANSYS show that a pulsed power density above 1 kW/mm^2 (for 500 μs pulses) is sufficient to vaporize the graphite surface. For simulations of the beam extraction at 45 kV, the maximum power density is 3.0 kW/mm^2, corresponding to more material being evapo-

---

[a)] Contributed paper, published as part of the Proceedings of the 14th International Conference on Ion Sources, Giardini Naxos, Italy, September 2011.

[b)] Author to whom correspondence should be addressed. Electronic mail: oystein.midttun@cern.ch.

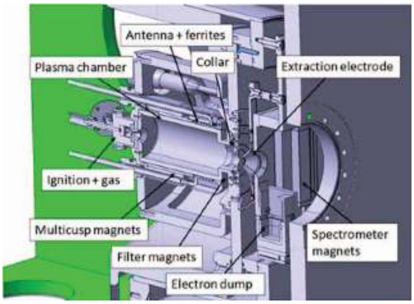

FIG. 1. (Color online) Cross section of the Linac4 ion source 3D model.

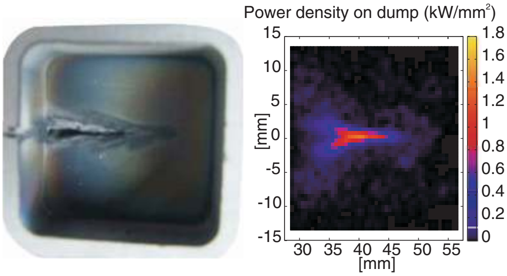

FIG. 2. (Color online) Comparison between a photo of the graphite electron dump used during the 35 kV commissioning and an IBSimu simulation of the surface power density from the electron beam on the dump. The groove from the center of the cup to the left results from the beam extraction at lower energy (0–35 keV) during the source commissioning.

rated, thus explaining the increase of high voltage breakdowns during beam extraction.

A quick solution for solving the problem of evaporating material from the electron dump could be to apply a negative voltage to the dump, lowering the energy of the electrons. The approach is however difficult to implement due to the lack of space in the present source design for the required insulation. In addition, simulations show that it does not allow a reduction of power density of at least one order of magnitude that will be required to safely operate the source at higher H^- currents up to 80 mA.

III. PROPOSAL OF A NEW EXTRACTION SYSTEM

The results of the 45 kV commissioning triggered the design of a new extraction system for the H^- source. The extraction system design will be based on IBSimu simulations of particle extraction from a plasma and simulations of beam transport using the CERN developed software PATH Manager.[4] Particle trajectories simulated in IBSimu can be exported and used as input in PATH Manager, making it possible for a full simulation of the source, low energy beam transport (LEBT) and RFQ.

The extraction system needs an improved handling of the electron dumping, where the co-extracted electrons are dumped in a controlled way at low energy. They should also be separated as early as possible from the ion beam to avoid excessive increase of beam size and emittance due to space charge. Furthermore, the beam properties need to be optimized for having the best matched emittance and divergence at the entry of the LEBT. Measurements have shown evidence of beam loss on the walls in the first part of the LEBT, which should be avoided in order to have the maximum current available for the RFQ. A steering possibility should also be implemented to counteract on the deflection on the H^- beam by the magnetic field for electron dumping, and the extraction system should be able to handle different H^- and electron currents without changing any mechanical parts.

Following these criteria, two design proposals have been made: One where the electrons are dumped at low energy on an intermediate extraction electrode and the H^- beam is post-accelerated to its full energy, and a second where the electrons are dumped in a magnetized Einzel lens. The length of the extraction system, from the plasma electrode to the connection of the LEBT, has a minimum length of 295 mm due to the space required by pumping ports and high voltage insulation.

A. Electron dump on intermediate electrode

A first proposed design for an extraction system with intermediate dumping electrode is shown in Fig. 3. The design is similar to the design of the one presently used at the Spallation Neutron Source (SNS). The beam is extracted using a low voltage of ~9 kV, and a magnetic dipole field dumps the electrons on the first electrode. A screening electrode prevents secondary electrons from being accelerated to the puller, whereas two Einzel lenses ensure good beam transport to the LEBT. The power density on the dumping electrode is 0.6 kW/mm^2 and thus below the vaporization limit.

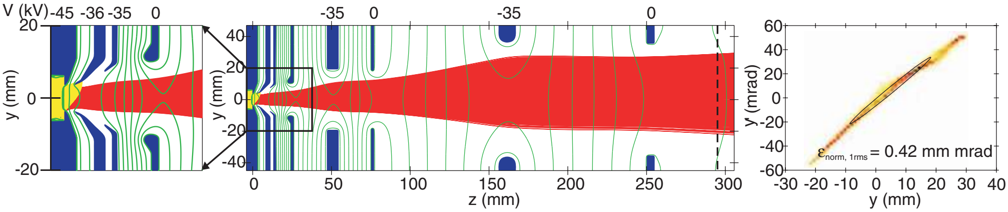

FIG. 3. (Color online) Particle trajectory plot from a simulation of the extraction system with electron dump on intermediate electrode. The electron beam [light grey (yellow)] is dumped on the first extraction electrode and the H^- beam [dark grey (red)] is guided to the LEBT entry (emittance plot at 295 mm).

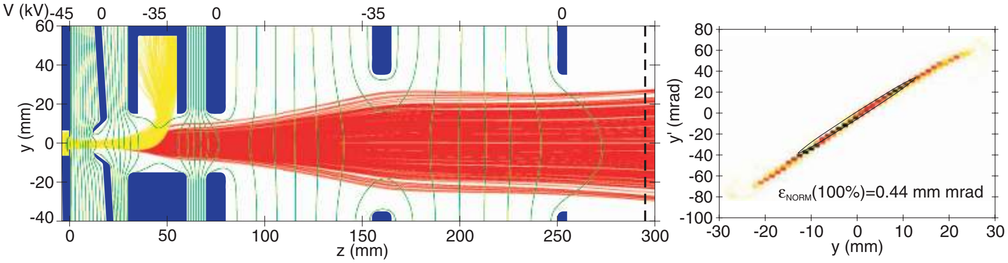

FIG. 4. (Color online) Particle trajectory plot from a simulation of the extraction system with electron dump in Einzel lens. The electron beam [light grey (yellow)] is dumped in an Einzel lens and the H^- beam [dark grey (red)] is guided to the LEBT entry at z = 295 mm. A tilt is applied to the puller to correct for the deviation of the H^- beam due to the magnetic field for the electron dumping.

B. Electron dump in magnetized Einzel lens

The second proposal uses a puller electrode to accelerate the beam from the source potential of −45 kV to ground (Fig. 4). The second electrode, which is a combined electron dump and Einzel lens at −35 kV, decelerates the beam and separates the electrons from the ion beam by a magnetic dipole field, lowering the maximum surface power density to 0.18 kW/mm^2. The H^- beam is then accelerated to full extraction energy. Again, a second Einzel is implemented for beam transport and beam optics tuning into the LEBT.

The negative ion beam displacement due to the electron dump field can be corrected by tilting and/or displacing the puller so that the negative ion beam is parallel and on axis at the entry of the LEBT (Fig. 4). In the case of different beam currents (e.g., e/H = 15), the beam optics can in addition be tuned by adjusting the puller voltage as shown in Fig. 5.

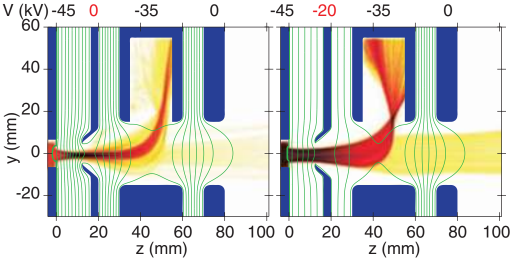

FIG. 5. (Color online) Example of beam optics optimization by adjusting the voltage on the puller. Particle density plot (arbitrary unit) of a simulation with an e/H ratio of 15, using the same geometry as in Fig. 4 without tilt or offset on the puller.

IV. CONCLUSION AND OUTLOOK

Two extraction systems have been designed using the simulation code IBSimu. The designs already satisfy the most crucial requirements for the Linac4 ion source upgrade and are still being optimized for better electron handling and H^- beam emittance. The simulated emittance values are similar for the two systems; however the second proposal, described in Sec. III B, is preferred since it has the possibility to correct for both beam alignment and different beam currents. The electron dumping is also done in a more controlled way with a lower electron beam power density on the dump.

A decision has been made to start the mechanical design and production of the extraction system with the electron dump in the magnetized Einzel lens, shown in Fig. 4. For further source development with the aim of reaching 80 mA H^- current, the introduction of caesium will ensure a higher H^- current by surface plasma production and a lower electron density in the extracted beam.

[1] J. Peters, AIP Conf. Proc. **925**, 79 (2007).
[2] M. Kronberger, D. Küchler, J. Lettry, Ø. Midttun, M. O'Neil, M. Paoluzzi, and R. Scrivens, Rev. Sci. Instrum. **81**, 02A708 (2010).
[3] T. Kalvas, O. Tarvainen, T. Ropponen, O. Steczkiewicz, J. Ärje, and H. Clark, Rev. Sci. Instrum. **81**, 02B703 (2010).
[4] A. Perrin, J.-F. Amand, T. Mütze, J.-B. Lallement, and S. Lanzone, *Travel v4.07 User Manual* (2007).

C.2 A magnetized Einzel lens electron dump for the Linac4 H^- ion source

This paper presents the extraction system with the magnetized Einzel electron dump. The design was based on simulations with IBSimu [1], which are presented together with the final extraction system design. The paper describes the different electrodes, and how they affect the optics of the ion beam.

The candidate was the main author of this paper and gave an oral presentation of the results at the International Symposium on Negative Ions, Beams and Sources (NIBS) 2012. The candidate made the simulations leading to the new ion beam extraction design and prepared all the figures for the paper.

A magnetized Einzel lens electron dump for the Linac4 H$^-$ ion source

Ø. Midttun[*,†], T. Kalvas[**], M. Kronberger[†,**], J. Lettry[†], H. Pereira[†] and R. Scrivens[†]

[*] *University of Oslo, P.O. Box 1072 Blindern, 0316 Oslo, Norway*
[†] *CERN, 1211 Geneva 23, Switzerland*
[**] *Department of Physics, University of Jyväskylä, P.O. Box 35, 40014, Finland*

Abstract. Linac4 is a 160 MeV linear accelerator which will inject negative hydrogen ions (H$^-$) into CERN's Proton Synchrotron Booster, a required upgrade to improve the beam brightness in the LHC injector chain. A volume production RF ion source, based on the design of the DESY RF source was implemented, but showed considerable electron dump ablation during operation at 45 keV beam energy. To reduce the electron beam power density in the dump, a magnetized Einzel lens is designed that reduces the beam energy to 10 keV before permanent magnets dump the electrons on a tungsten surface. Presented in this paper are simulations of the design using IBSimu, the tunable range of parameters depending on the extracted H$^-$ and electron current, as well as details of the implementation, the choice of pulsed power converters and the electrode alignment system. In addition, simulations of proton extraction from this source will be shown.

Keywords: H- ion source, beam optics, extraction, simulation
PACS: 41.75.Cn, 41.85.Ar, 52.65.Ff

INTRODUCTION

A prototype of a new ion source for Linac4 has been constructed at CERN and is ready for commissioning [1]. The initial design based on the non-caesiated, 2 MHz DESY H$^-$ volume source [2] has undergone major modifications of the plasma generator and extraction system to meet Linac4 requirements. The specification for the Linac4 ion source is a pulsed H$^-$ beam of 500 μs, 45 keV beam energy, 80 mA beam current with a normalized rms emittance of 0.25 mm mrad at a repetition rate of 2 Hz. The goal has proven to be challenging when it comes to the requirements of beam current, emittance and extraction voltage.

In 2009, an H$^-$ beam of 23 mA with an energy of 35 keV and 0.26 mm mrad emittance was demonstrated from the non-caesiated source as reported in [3] and [4]. However, when the extraction voltage was increased to 45 kV in 2010, ablation of the electron dump caused frequent high voltage breakdowns between the plasma generator and the puller, making it impossible to operate the source. In 2011, two new extraction systems were proposed to ensure that the co-extracted electrons would be dumped in a controlled manner and that the high current beam would be transported to the two solenoid Low Energy Beam Transport (LEBT) with low emittance and beam loss. Both systems were designed and optimized with the simulation code IBSimu. A decision was made to construct a new extraction system where the electrons are dumped in a magnetized Einzel lens, lowering the electron beam energy in the dump and at the same

Third International Symposium on Negative Ions, Beams and Sources (NIBS 2012)
AIP Conf. Proc. 1515, 481-490 (2013); doi: 10.1063/1.4792819

time focusing the H^- beam [5]. The source will in addition use pulsed high voltage power supplies to avoid breakdowns occurring in between beam pulses and to reduce damage from sparks with the 2 μF capacitively backed DC high voltage system that was previously used. The first prototype of the ion source is designed to produce a beam of 20-30 mA for the commissioning of the LEBT, Radio Frequency Quadrupole (RFQ) and beam chopping system.

During the upgrade of the negative ion source, the plasma generator and extraction system was operated with inverted polarity to provide a proton beam (with ∼10% fractions of H_2^+ and H_3^+) at 45 keV for commissioning of the LEBT.

SIMULATION AND DESIGN OF EXTRACTION SYSTEM

During the commissioning of the ion source, different parameters (e.g. H_2 gas pressure, RF-power) that will affect the plasma properties and beam formation will be iteratively tuned in order to optimize the extracted H^- and electron currents and the beam emittance. Thus, the extraction system is designed to be flexible and the optics of the system is tunable *in-situ* for the optimum transmission of the negative ion beam. This choice of design makes the extraction system complex, however at this stage of the development, the adaptability of the system is required for systematic studies of the ion source.

The new extraction system, shown in Fig. 1, has a design based on simulations with IBSimu, a general-purpose three-dimensional (3D) simulation code for charged particle optics with space charge [6]. The ion source uses a multiple electrode extraction system for transporting the beam to a two solenoid LEBT. The puller accelerates the beam from the source before the beam enters a magnetized Einzel lens where the electrons are dumped. A second Einzel lens is implemented for H^- beam transport and beam optics tuning into the LEBT. The effect of each of the electrodes is described in the following sections. The geometry for the simulation has been imported to IBSimu as a DXF file and the magnetic field for the electron dump has been calculated with Vector Fields OPERA/TOSCA [7].

Initial conditions for simulation

For all simulations described in this paper, a set of plasma parameters which previously have shown good agreement between simulations and measurements [5], has been chosen and kept constant. The most important are the transverse temperature (T_t = 0.5 eV) and the initial energy (E_0 = 5.0 eV) of ions and electrons. The simulations use a rectangular mesh with a step size of 0.5 mm. The simulated beam current of H^- and electrons has been distributed over 30,000 particle trajectories for each specie, starting from a plane inside a defined plasma volume. Approximately one third of these trajectories exit the plasma generator and are tracked through the extraction system. The parameter space of H^- currents and electron to H^- (e/H^-) current ratios have been selected based on measurement results from the 35 keV commissioning of the Linac4 ion source made in 2009 [3]. The H^- current has been varied from 10 to 30 mA and the e/H^- ratio from 20 to 60. The potentials of the plasma generator at -45 kV, the magne-

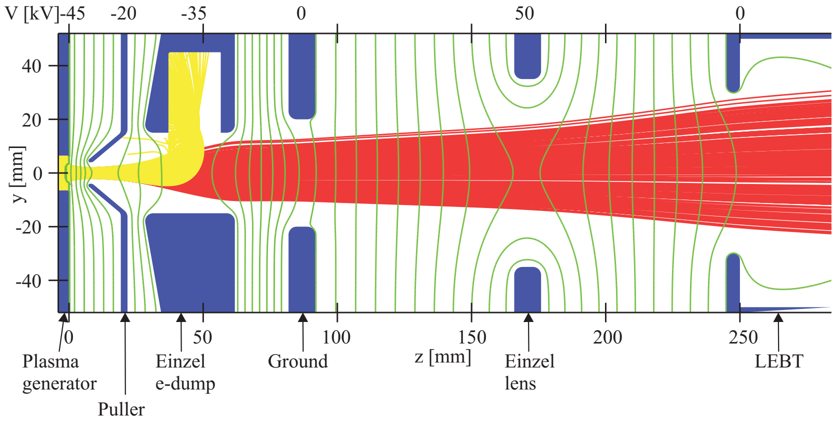

FIGURE 1. Simulation of the extraction system of the Linac4 ion source. The electron beam in yellow (light grey) is deviated and dumped in the magnetized Einzel lens. The H^- beam in red (dark grey) is focused by two Einzel lenses and transported to the LEBT.

tized Einzel lens at -35 kV, and the grounded electrode and LEBT at 0 V have been kept constant in all simulations.

Puller electrode

The puller electrode provides the first stage of acceleration of the H^- beam and has, in addition, two tuning possibilities: (1) A variable voltage to give the best matched electrical field for the plasma meniscus. (2) The possibility to tilt and move for correcting the misalignment of the H^- beam caused by the magnetic field in the electron dump.

Plasma meniscus tuning

When extracting a beam from a plasma, the process of beam formation will vary with the properties of the plasma, i.e. plasma density, electron and ion temperature and electron to ion ratio. In Fig. 2, three simulated cases of beam extraction are illustrated. All simulations use an extraction voltage of -30 kV, giving a beam energy of 15 keV. Only the H^- beam current density has been varied while the e/H^- ratio has been fixed to 50. Case (a) shows an extraction of a 5 mA H^- beam, which with the strong electrical field gives an over-focused beam. In (b), the beam current is 20 mA and shows the ideal case where the plasma meniscus is slightly convex giving a close to parallel beam. In case (c), the beam current is 50 mA, and here the beam is divergent and part of it is even lost on the puller.

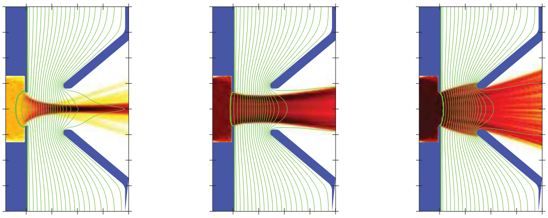

(a) (b) (c)

FIGURE 2. Illustration of beam extraction from under-dense, matched density and over-dense plasmas. (a) 5 mA H$^-$: Over-focused beam, (b) 20 mA H$^-$: Matched puller voltage to beam current density, (c) 50 mA H$^-$: Divergent beam. All three cases use an e/H$^-$ ratio of 50 and an extraction potential of 15 kV.

A set of simulations was made to visualize the effect of the puller voltage on the beam properties of the Linac4 ion source, notably the H$^-$ beam emittance and the efficiency of the H$^-$ transmission and electron dumping. The H$^-$ transmission efficiency is defined as the fraction of H$^-$ ions that reaches the LEBT entry. Likewise, the electron dumping efficiency is the fraction of electrons being dumped inside the tungsten dump in the magnetized Einzel lens. Electrons dumped on the side walls of magnetized Einzel lens are not included in the calculation. Figure 3 shows a case where the beam parameters vary as a function of the puller voltage with a constant H$^-$ current of 20 mA and an e/H$^-$ ratio of 40. These conditions give an optimum puller voltage of -28 kV for minimum emittance and maximum transmission efficiency.

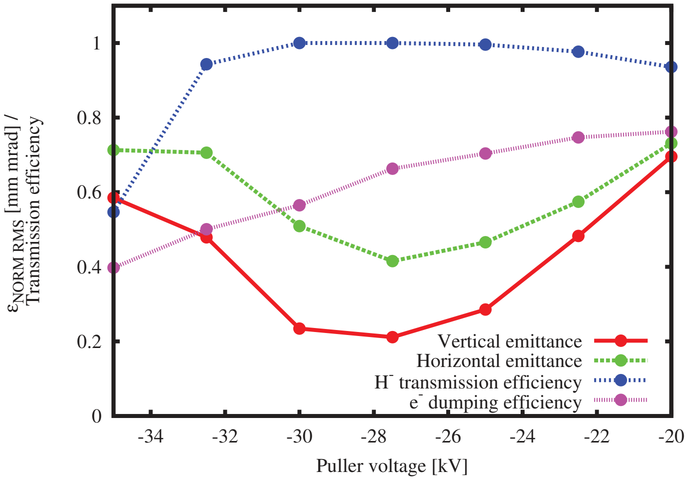

FIGURE 3. Emittance, H$^-$ transmission and electron dumping as a function of the puller voltage. H$^-$ current is 20 mA and e/H$^-$ ratio is 40.

Assuming that the beam size and emittance mainly is defined by the shape of the plasma meniscus and the beam acceleration until the electron dump, the data set can be expanded to take into account the different extracted beam currents. It is then possible to visualize a voltage range within where one should work for optimal beam optics depending on the total space charge equivalent H$^-$ current extracted from the source:

$$I_{tot\,H^-\,eqv} = I_{H^-} + I_e\sqrt{\frac{m_e}{m_{H^-}}}, \tag{1}$$

where I_{H^-} and I_e represents the extracted H$^-$ and electron current and m_e and m_{H^-} the mass of electrons and H$^-$ respectively. Figure 4 shows the H$^-$ transmission efficiency and the horizontal emittance of the H$^-$ beam as a function of the puller voltage and I$_{tot\,H^-\,eqv}$. The plots show that the highest H$^-$ transmission efficiency and lowest emittance is obtained with the same matching of puller voltage to extracted beam current.

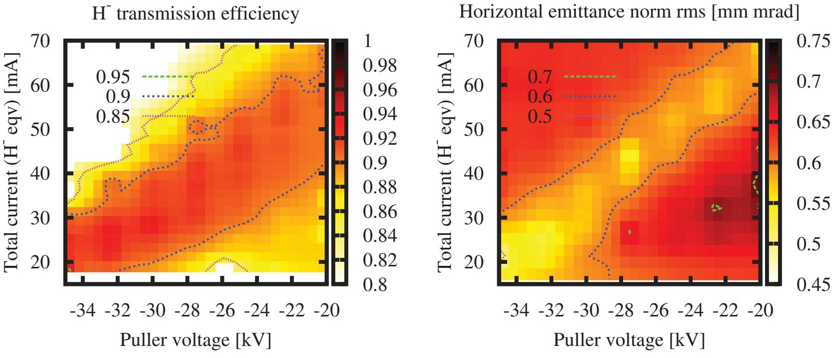

(a) (b)

FIGURE 4. (a) H$^-$ transmission efficiency and (b) horizontal emittance as a function of the voltage on the puller and the total space charge equivalent H$^-$ current.

H$^-$ beam steering

For compensating the offset of the beam induced by the electron dump magnetic field, the puller can be tilted and moved in the horizontal plane parallel to the electron dump direction. Shown in Fig. 5 is the impact of the puller tilt and offset on the position of the beam at the LEBT entry. The H$^-$ beam current has been kept constant at 30 mA and the e/H$^-$ ratio to 50 with a puller voltage of -20 kV. The two contour lines show under which conditions the beam is located centrally on axis and parallel to it. The plot shows that the beam position and angle are very sensitive to the offset of the puller (5.3 mm/mm and 10 mrad/mm respectively), however, the variation is less dependent of the puller tilt

(0.16 mm/deg and 0.12 mrad/deg respectively). The two zero lines converge to a value of puller tilt and offset giving an average zero position and angle of the beam at the entry of the LEBT. In this case, the optimum value of tilt is -5°and the offset is 0.85 mm, however this could vary for different beam currents and puller voltages.

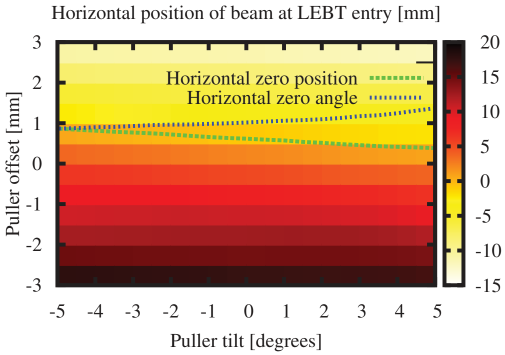

FIGURE 5. Optimum tilt and offset of the puller electrode.

Einzel electron dump

The second electrode of the extraction system is a magnetized Einzel lens, focusing the H^- beam and dumping the electrons with a magnetic dipole field, illustrated in Fig. 6 (a). The H^- beam will also be deviated from the beam axis by this field and should be corrected. A second magnet dipole may be used, however, it has not been implemented in the present design, making the electrode shorter and reducing the emittance growth at low energy (10 keV). Due to the compact design and high magnetic field, a small fraction of the electrons (< 1 %) could return back to the puller, as is visible in Fig. 1. The quantity depends on the beam current and the extraction system tuning, however, this situation is acceptable compared to the risk of having electrons being transported through the electrode and follow the H^- beam or hit the grounded electrode with an energy of 45 keV. A correction of the H^- beam misalignment is still possible by applying an offset and/or tilt to the puller as previously described.

Electron beam power density

As reported in [5], the electron dumping at 45 keV beam energy caused sublimation of the dump material resulting in high voltage breakdowns in the source. The simulation of that extraction configuration showed a peak electron beam power density of 3.0 kW/mm^2

in the cup. Transient thermal simulations made with ANSYS have shown that a pulsed power density above 1 kW/mm^2 for a 500 μs beam pulse is sufficient for sublimating a graphite surface, the material used in the DESY source. For a tungsten surface, the accepted power density is approximately a factor 2 higher, however, this is still not sufficient for avoiding thermally induced damage. In addition to changing the material, the electron beam energy in the dump thus was reduced from 45 keV to 10 keV and the dump has been designed to spread the beam over a larger surface in the dump. The electron beam power density was calculated for all surfaces of the new dump design and was shown to be always one order of magnitude below the critical power density for tungsten. Figure 6 (b) shows that even for highest electron currents extracted, the dumped electron beam power density is acceptable.

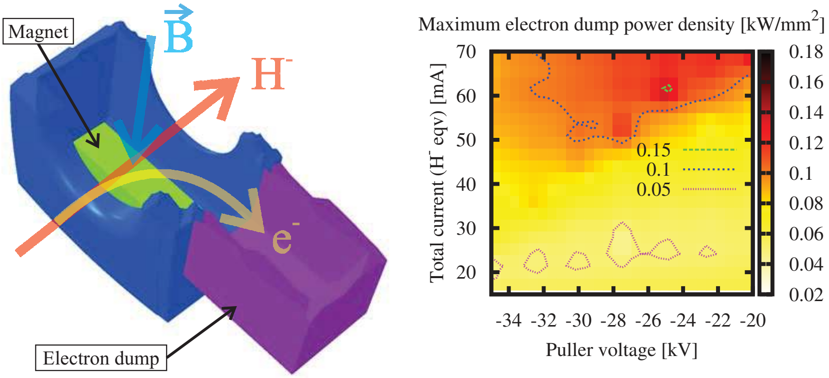

(a) (b)

FIGURE 6. (a) Cross-section of the electron dump. (b) Maximum power density in the electron dump as a function of the voltage on the puller and the total space charge equivalent H$^-$ current.

Due to the low duty factor (2 Hz, 0.5 ms), no active cooling of the dump is implemented. Instead, the heat from the electron beam is evacuated by thermal radiation and conduction through a copper leg and a Shapal ceramic insulator to the stainless steel source body. The average heat distribution in the dump was studied by an ANSYS steady state thermal simulation showing that the temperature increases from room temperature to 57°C for a beam pulse length of 600 μs.

Einzel lens

The purpose of the second Einzel lens is to transport the H$^-$ beam to the LEBT keeping the beam size small and avoiding excessive emittance growth. The power supply for the lens is bipolar with a maximum voltage of 50 kV. A negative bias decelerates the beam and is a good method for keeping the beam size small. It causes, however, space charge induced emittance growth due to the low ion velocity inside the lens. A positive bias is preferable since the emittance is kept low, but the voltage needs to be higher to avoid particles hitting the beam pipe. Figure 7 demonstrates the improved emittance of the accelerating lens. Optimization of the positive bias Einzel lens geometry is pending.

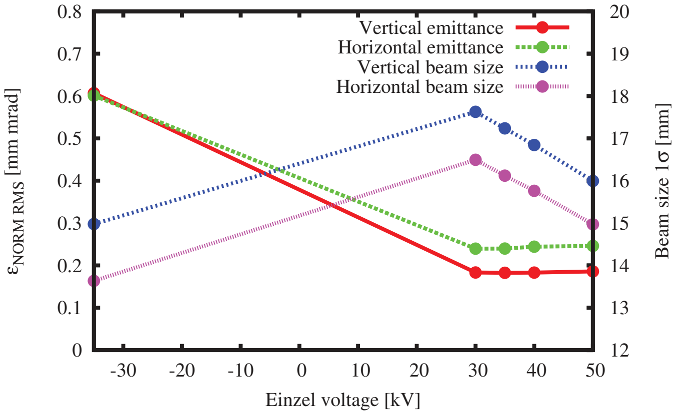

FIGURE 7. Emittance and beam size as function of Einzel lens voltage. H^- beam current is 30 mA, e/H^- is 50 and puller voltage is -20 kV.

Proton simulation

During the commissioning of the volume source, the H^- current is limited below 30 mA. In order to test the LEBT and RFQ in a higher space charge regime, the source will run in proton mode by reversing the polarity of the high voltage systems. Figure 8 shows that it is possible to run the ion source with a proton beam of 80 mA being extracted through the same geometry as for the H^- beam.

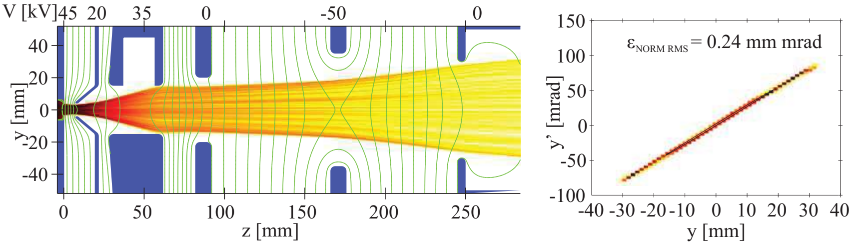

(a) (b)

FIGURE 8. 80 mA proton extraction with inverted polarities on the electrodes. (a) Proton particle density plot. (b) Phase space plot at the simulation end.

DETAILS OF IMPLEMENTATION

Figure 9 shows a cut of the 3D model of the new plasma generator and extraction system for the Linac4 ion source with the beam travelling from bottom right to top left. The design of the extraction system was based on the geometry that was found to give the best results in the IBSimu simulations. At the exit of the plasma chamber sits the molybdenum plasma electrode with an aperture of 6.5 mm diameter. The puller is also made of molybdenum with an aperture of 8.0 mm diameter and is located at a distance of 7.0 mm from the plasma generator. It gives the first stage of acceleration up to 25 keV. The body of the magnetized Einzel lens is built of ARMCO, magnetic steel, to confine the magnetic dipole field within the electrode. The dipole is made from a pair of SmCo permanent magnets which are nickel and then copper coated to prevent reaction of the micro-structure of the magnets under low pressure of hydrogen [8]. The electron dump target is made of tungsten for minimizing the ablation by the electron beam. The tungsten dump is brazed to a copper arm held on a Shapal insulator for heat evacuation by conduction.

The final acceleration stage to 45 keV is made by the grounded electrode. Between the grounded electrode and the LEBT entry , a > 150 mm gap provides space for the high voltage insulators and vacuum pumping. A second Einzel lens that can be biased either positively or negatively is used to keep the beam size small for minimum particle loss. The voltages for the plasma generator, the puller and the magnetized Einzel dump will be pulsed, whereas a DC voltage will be used for the Einzel lens.

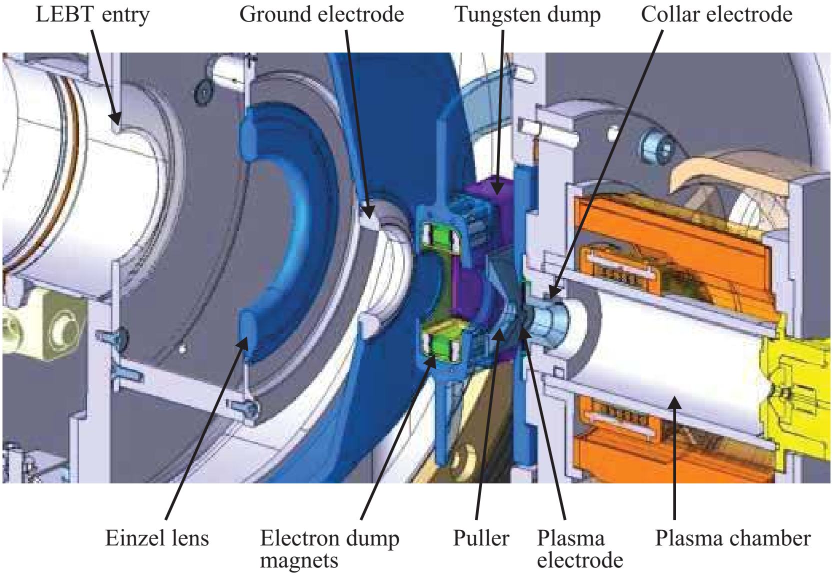

FIGURE 9. Cross-section of the Linac4 plasma generator and extraction system.

CONCLUSION AND OUTLOOK

A new extraction system has been designed and built for the Linac4 H^- ion source. It is a flexible system well suited for the ion source and LEBT commissioning where systematic studies of the different source parameters will be made in order to optimize the extracted beam current and its emittance.

In parallel with the upgrade of the plasma generator and extraction system, an effort is started to caesiate the collar electrode near the extraction hole of the plasma chamber to meet the final requirement of beam current [1]. The caesiation will lower the work function of the collar surface and increase the surface production rate of H^- ions. The higher population of H^- in the plasma will also help to reduce the ratio of co-extracted electrons, which again will reduce the electron beam impact on the electron dump. A lower emittance of the H^- beam is expected due to less space charge from the electrons.

Future possible upgrades of the extraction system include:

- Motorization of the puller tilt and offset for *in-situ* tuning. For the first prototype, the extraction system has to be dismantled to manually move the position of the puller.
- An increase of the extraction voltage of the puller. The 25 kV power supply for the puller is biased relative to the source body, however, by connecting it to ground instead, it is possible to increase the extraction voltage up to 70 kV provided improvement of the insulation.
- Optimization of the dipole field in the magnetized Einzel lens in order to collect all electrons inside the electron dump with a maximum spread of the electron beam.
- Optimization of the shape of the second Einzel lens to achieve better focusing.
- A reduction the overall length of the extraction system for minimum emittance growth.

REFERENCES

1. J. Lettry, et al., *Proceedings of NIBS 2012, Jyväskylä, Finland* (2012).
2. J. Peters, *AIP Conference Proceedings* **925**, 79–86 (2007), URL `http://link.aip.org/link/?APC/925/79/1`.
3. M. Kronberger, D. Küchler, J. Lettry, Ø. Midttun, M. O'Neil, M. Paoluzzi, and R. Scrivens, *Review of Scientific Instruments* **81**, 02A708 (2010), URL `http://link.aip.org/link/?RSI/81/02A708/1`.
4. B. Cheymol, E. Bravin, C. Dutriat, A. Lokhovitskiy, U. Raich, F. Roncarolo, R. Scrivens, and E. Zorin, *Proceedings of IPAC10, Kyoto, Japan* p. 1092 (2010), URL `http://accelconf.web.cern.ch/AccelConf/IPAC10/papers/mope053.pdf`.
5. Ø. Midttun, T. Kalvas, M. Kronberger, J. Lettry, H. Pereira, C. Schmitzer, and R. Scrivens, *Review of Scientific Instruments* **83**, 02B710 (2012), URL `http://link.aip.org/link/?RSI/83/02B710/1`.
6. T. Kalvas, O. Tarvainen, T. Ropponen, O. Steczkiewicz, J. Ärje, and H. Clark, *Review of Scientific Instruments* **81**, 02B703 (2010), URL `http://link.aip.org/link/?RSI/81/02B703/1`.
7. Vector fields opera (2012), URL `http://vectorfields.com/`.
8. *Rare-Earth permanent magnets Vacodym-Vacomax*, Vacuumschmelze GmbH & Co (2007), URL `http://www.vacuumschmelze.com/fileadmin/documents/broschueren/dmbrosch/PD-002_e_310807.pdf`.

C.3 Measurements of Linac4 H$^-$ ion source beam with a magnetized Einzel lens electron dump

This paper presents a selection of the first measurements of the ion beam with the extraction system. The results were compared with measurements and showed good similarity. It was demonstrated that secondary electron emission from the electrodes had to be included in the simulations to match the measured beam currents.

The candidate was the main author of this paper and gave an oral presentation of the results at the International Conference on Ion Sources (ICIS) 2013. The candidate made all the measurements and comparisons with simulations.

REVIEW OF SCIENTIFIC INSTRUMENTS **85**, 02A701 (2014)

Measurements of Linac4 H^- ion source beam with a magnetized Einzel lens electron dump[a)]

Øystein Midttun,[1,2,b)] Jacques Lettry,[2] and Richard Scrivens[2]
[1]*Department of Physics, University of Oslo, P.O. Box 1072 Blindern, 0316 Oslo, Norway*
[2]*CERN, 1211 Geneva 23, Switzerland*

(Presented 9 September 2013; received 6 September 2013; accepted 20 September 2013; published online 16 October 2013)

Linac4 is a part of the upgrade of CERN's accelerator complex for increased luminosity in the Large Hadron Collider (LHC). A new system to extract the ion beam from the plasma generator has been designed and tested, in order to improve the reliability and beam optics of the pulsed H^- ion source. This paper presents the successfully implemented extraction system and three different beam measurements. The simulations compare well to the measurements and show that the plasma density was too low for the extraction system design during the measurements. © *2013 AIP Publishing LLC*. [http://dx.doi.org/10.1063/1.4824814]

I. INTRODUCTION

Linac4 is a 160 MeV negative hydrogen linear accelerator that will replace the ageing 50 MeV proton accelerator, Linac2, as an injector to the Proton Synchrotron Booster (PSB). This upgrade is the first step of a long-term program aiming for an increase in the Large Hadron Collider (LHC) luminosity.[1] The specification for the ion source is a pulsed H^- beam of 500 μs, 45 keV beam energy, and 80 mA beam current within a normalized rms emittance of 0.25 mm mrad at a repetition rate of 2 Hz.

The ion source, based on the non-caesiated, 2 MHz DESY H^- volume source, has been designed with a new extraction system to provide a more flexible and reliable operation, where co-extracted electrons are safely dumped with an energy below 10 keV.[2–4] At the present stage of the ion source development program, the extraction system is designed for a maximum H^- beam current of 30 mA with an electron to H^- (e/H^-) ratio of 50.[5,6]

II. ION SOURCE DESIGN

The ion source, as shown in Fig. 1, consists of two independent parts: the plasma generator and the front end. These two parts are exchangeable, and the ion source has been designed with sufficient flexibility to host plasma generators based on different ion production modes:[6]

1. A DESY type RF-driven plasma generator (volume production).
2. A version of the DESY plasma generator upgraded to high RF-power—IS01 (volume production).
3. A RF-driven plasma generator with a caesiated molybdenum surface—IS02 (surface production).
4. A magnetron type plasma generator—IS03 (arc discharge).

The measurements presented in this paper have been made with the DESY plasma generator.

The plasma generator is kept at −45 kV during operation, and the newly implemented multi-stage extraction system sits inside the front-end.[5] A puller electrode gives the first acceleration from the plasma generator and shapes the plasma meniscus, which depends on the electric extraction field and the ion density in the plasma. The electrons are dumped inside a magnetized Einzel lens kept at high voltage to reduce the electron energy and to distribute the electrons over a large surface. A second Einzel lens ensures suitable beam size to enter the Low Energy Beam Transport (LEBT).

The extraction system has been designed with IBSimu, a general-purpose three-dimensional simulation code for charged particle optics with space charge.[7] In IBSimu, the input values for the H^- and electron beam currents are given as uniform current densities (A/m^2) within the plasma volume, and the extracted beam consists of those particle trajectories that are caught by the electric field at the plasma aperture. These input values are estimated from the final measured beam current and the outlet aperture size, but this can lead to a significant error when beam loss is involved, and also depend on the setting of the plasma generator. The simulation results presented in this paper use input current densities of H^- and electrons that give the best match to the results of electrical currents measured on all the electrodes in the extraction region.

III. MEASUREMENTS

In this paper, three sets of measurements are presented, each as a function of a different ion source parameter.

1. RF-power: It changes the H^- density in the plasma.
2. Puller voltage: It defines the electric extraction field.
3. Plasma aperture potential: It modifies the ion and electron densities close to the plasma aperture.

The comparison with simulations is made by using the currents measured on the plasma generator, puller, and

---

[a)] Contributed paper, published as part of the Proceedings of the 15th International Conference on Ion Sources, Chiba, Japan, September 2013.

[b)] Author to whom correspondence should be addressed. Electronic mail: oystein.midttun@cern.ch

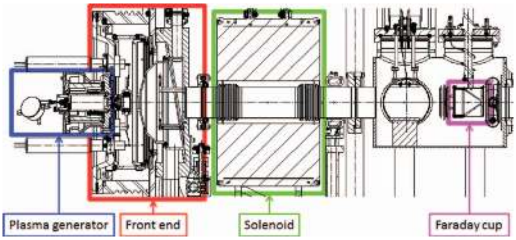

FIG. 1. Layout of the Linac4 ion source and the first part of the LEBT.

electron dump using Pearson transformers, and the H^- beam current measured in the Faraday cup.

A. RF-power

In this measurement, the RF forward power was varied from 20 kW to 30 kW. Increased RF-power should lead to a higher degree of ionization in the plasma, which means a higher plasma density, and higher extracted beam current. The results are shown in Fig. 2. For measured currents, the x-axis corresponds to the current density linearly scaled from the RF-power transmitted to the source (i.e., the incident minus the reflected power). The extraction system electrodes are illustrated in Fig. 3.

The measurement shows an expected increase in extracted beam current, and the simulated values correspond well. Included in the simulation are secondary electrons emitted from the electron dump by the impacting H^- and electron beam, illustrated in black in Fig. 3. Since these negative charges leave the electron dump, the measured current here is lower than the simulation output without secondary electron emission. Likewise, the measured puller current is higher because of these electrons. The few secondary electrons that follow the H^- to the LEBT are lost on the walls of the beam pipe in the solenoid and do not affect the Faraday cup measurement.

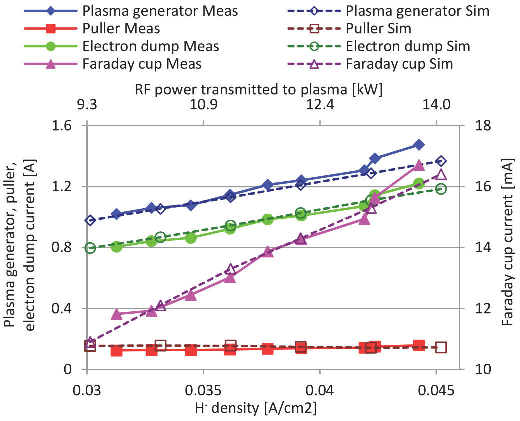

FIG. 2. Comparison between measurements and simulation with varying RF-power. The RF-power on the x-axis has been linearly scaled to match the H^- density used as input in the simulations.

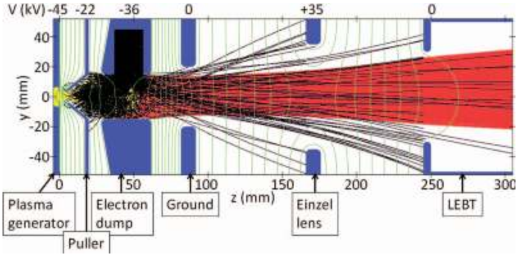

FIG. 3. Image from a simulation. The beam is over-focused and parts of the H^- beam (red/dark grey) scrape the inside of the electron dump. Secondary electrons from the electron dump are shown in black.

B. Puller voltage

The extraction system has been designed with a tunable puller voltage to change the electric field near the plasma aperture, and modify the shape of the plasma meniscus. With this option, it is then possible to tune the ion beam optics without changing the final energy of the ion beam.

Figure 4 shows that there is good agreement between simulations and measurements. We make two observations of the total current extracted from the plasma generator: (1) it increases with higher extraction voltage, and (2) the measured current increases slightly more than the simulated one.

The first observation is explained by the plasma meniscus that becomes more curved with higher extraction field. The meniscus surface is then increasing, allowing more particles to be extracted for a constant plasma density. The second observation suggests that when the plasma meniscus is being pushed further into the plasma, the plasma density increases. This effect is then causing a higher extracted beam current than the expected simulation value when the H^- density in

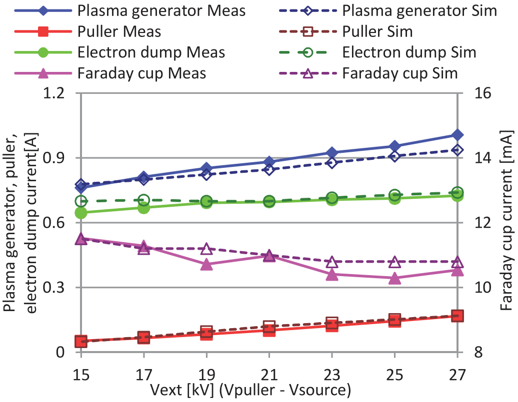

FIG. 4. Comparison between measurements and simulation with varying puller voltage.

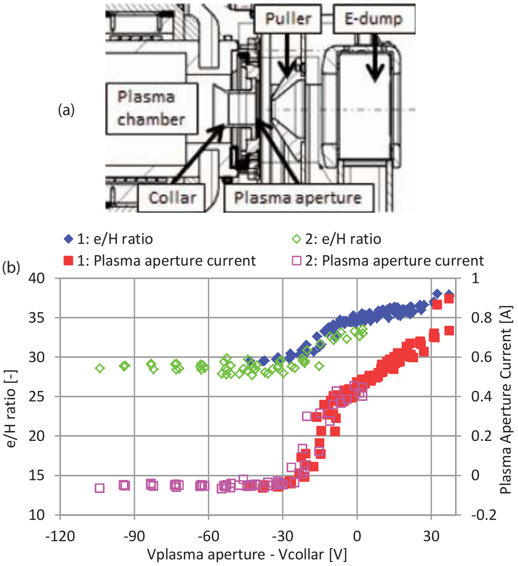

FIG. 5. (a) Detail of the extraction region. (b) e/H$^-$ ratio and plasma aperture current measured at two different days as a function of the voltage difference between the plasma aperture and collar electrodes.

the plasma is assumed to be constant. This variation of density as a function of depth of the plasma has previously been reported from Langmuir gauge measurements with a similar plasma generator.[8]

C. Plasma aperture voltage

The DESY plasma generator is equipped with two electrodes close to the extraction hole that can be biased individually relative to the plasma generator (Fig. 5(a)). The collar is the largest electrode and will locally change the reference potential, whereas the plasma aperture electrode can be used to change the potential close to the extraction hole. In one way, we can treat the plasma aperture as a Langmuir probe measuring the charges in the plasma with respect to the plasma potential set by the collar. This behavior is clearly visible on the plot in Fig. 5(b), where the plasma aperture current looks similar to a Langmuir I-V curve, when plotted as a function of the voltage difference between the plasma aperture and the collar. The plot shows measurements made on two different days, and the plot shape is conserved even when connecting either of the electrodes to the plasma generator potential.

The e/H$^-$ ratio, plotted in Fig. 5(b), has been estimated from the measured ratio between the plasma generator current minus the Faraday cup current (electrons) and the Faraday cup current (H$^-$). This ratio shows a similar shape as the plasma aperture current which can be explained as follows: When the plasma aperture is biased negatively, negative charges are repelled away from the extraction hole reducing the density of H$^-$ and electrons in this region. Since the electrons have significantly less mass than the H$^-$, they are much more affected by this voltage difference, whereas the H$^-$ current remains nearly unchanged. By applying a voltage difference of −30 V, the e/H$^-$ ratio is reduced by 20%. With a higher voltage difference, the plasma aperture current is in the positive ion saturation region, and there is no more gain.

IV. CONCLUSION

The new extraction system has been implemented with success and has improved the ion source reliability drastically. During the first three months of operation, the source was running 24 h/day without high voltage breakdowns, and the electron dump has no visible spots from the electron beam.

The simulations compare well with the measurements. These results show that the plasma is lower in density than the extraction system is designed to handle, causing secondary electron emission from beam scraping in the electron dump.

[1] R. Garoby *et al.*, "Status and plans for the upgrade of the lhc injectors," Technical Report CERN-ATS-2013-059 (CERN, Geneva, 2013).
[2] J. Peters, AIP Conf. Proc. **1097**, 171 (2009).
[3] D. Küchler, T. Meinschad, J. Peters, and R. Scrivens, Rev. Sci. Instrum. **79**, 02A504 (2008).
[4] Ø. Midttun, T. Kalvas, M. Kronberger, J. Lettry, H. Pereira, C. Schmitzer, and R. Scrivens, Rev. Sci. Instrum. **83**, 02B710 (2012).
[5] Ø. Midttun, T. Kalvas, M. Kronberger, J. Lettry, H. Pereira, and R. Scrivens, AIP Conf. Proc. **1515**, 481 (2013).
[6] J. Lettry *et al.*, AIP Conf. Proc. **1515**, 302 (2013).
[7] T. Kalvas, O. Tarvainen, T. Ropponen, O. Steczkiewicz, J. Ärje, and H. Clark, Rev. Sci. Instrum. **81**, 02B703 (2010).
[8] J. Peters, AIP Conf. Proc. **639**, 42 (2002).

Bibliography

[1] T. Kalvas, O. Tarvainen, T. Ropponen, O. Steczkiewicz, J. Ärje, and H. Clark. IBSIMU: A three-dimensional simulation software for charged particle optics. *Review of Scientific Instruments*, 81(2):02B703, 2010.

[2] W. Henning and C. Shank. Accelerators for America's Future. Technical report, U.S. Department of Energy, 2010.

[3] D. C. Faircloth, S. R. Lawrie, A. P. Letchford, C. Gabor, M. Whitehead, et al. Latest results from the Front End Test Stand high performance H^- ion source at RAL. *AIP Conf.Proc.*, 1390:205–215, 2011.

[4] M. P. Stockli, B. X. Han, T. W. Hardek, Y. W. Kang, S. N. Murray, T. R. Pennisi, C. Piller, M. Santana, and R. Welton. Producing persistent, high-current, high-duty-factor H^- beams for routine 1 MW operation of Spallation Neutron Source. *Review of Scientific Instruments*, 83(2):02A732, 2012.

[5] H. Oguri, Namekawa Y., Ohkoshi K., Ueno A., and Ikegami K. Status of the J-PARC Negative Hydrogen Ion Source. *Proceedings of LINAC2010, Tsukuba, Japan*, pages 1016–1018, 2010.

[6] P. Franzen, R. Gutser, U. Fantz, W. Kraus, H. Falter, M. Fröschle, B. Heinemann, P. McNeely, R. Nocentini, R. Riedl, A. Stäbler, and D. Wünderlich. Performance of multi-aperture grid extraction systems for an iter-relevant rf-driven negative hydrogen ion source. *Nuclear Fusion*, 51(7):073035, 2011.

[7] Cern Accelerator Complex. `http://home.web.cern.ch/about/accelerators`.

[8] ATLAS Collaboration. The ATLAS Experiment at the CERN Large Hadron Collider. *JINST*, 3:S08003, 2008.

[9] CMS Collaboration. The CMS experiment at the CERN LHC. *JINST*, 3:S08004, 2008.

[10] ALICE Collaboration. The ALICE experiment at the CERN LHC. *JINST*, 3:S08002, 2008.

[11] LHCb Collaboration. The LHCb Detector at the LHC. *JINST*, 3:S08005, 2008.

[12] B. Jonson and K. Riisager. The ISOLDE facility. *Scholarpedia*, 5(7):9742, 2010.

[13] S. A. Baird et al. Design study of the antiproton decelerator: AD. Technical Report CERN-PS-96-043-AR, CERN, Geneva, Nov 1996.

[14] nTOF Collaboration. The neutron Time-Of-Flight facility, nTOF, at CERN (I): Technical Description. *nTOF Public Notes*, Feb 2013. First draft version.

[15] K. Elsener. General description of the CERN project for a neutrino beam to Gran Sasso (CNGS). Technical Report CERN-AC-Note-2000-03, CERN, Geneva, 2000.

[16] J. P. Delahaye. The CLIC study of a multi-TeV linear collider. *Annu. Rev. Nucl. Part. Sci.*, 62:105–131. 27 p, 2012.

[17] The history of CERN. `http://timeline.web.cern.ch/timelines/The-history-of-CERN`.

[18] CERN. *CAS - CERN Accelerator School: Intermediate Course on Accelerator Physics*, Geneva, 2006. CERN.

[19] K. Hanke, M. Chanel, and K. Schindl. The PS Booster hits 40. *CERN Courier*, Sep 2012.

[20] F. Gerigk and M. Vretenar. Linac4 Technical Design Report. Technical Report CERN-AB-2006-084 ABP/RF, CERN, 2006.

[21] B. Goddard et al. Can the proton injectors meet the HL-LHC requirements after LS2? *Chamonix 2012 Workshop on LHC Performance*, pages 325–331, 2012.

[22] E. Wilson. *An introduction to particle accelerators*. Oxford Univ. Press, Oxford, 2001.

[23] P. Allison, J. D. Sherman, and H. V. Smith. Comparison of measured emittance of an H^- ion beam with a simple theory. Technical Report LA-8808-MS, Los Alamos National Laboratory, 1981.

[24] R. Becker and W. B. Herrmannsfeldt. Why pi and mrad. *Rev.Sci.Instrum.*, 77:03B907, 2006.

[25] F. Wenander, B. Jonson, L. Liljeby, and G. H. Nyman. REXEBIS the Electron Beam Ion Source for the REX-ISOLDE project. Technical Report CERN-OPEN-2000-320, CERN, Geneva, Dec 1998.

[26] I. Langmuir and K. H. Kingdon. Thermionic effects caused by vapours of alkali metals. *Proceedings of the Royal Society of London. Series A*, 107(741):61–79, 1925.

[27] M. N. Saha. Ionization in the solar chromosphere. *Philosophical Magazine Series 6*, 40(238):472–488, 1920.

[28] M. J. Copley and T. E. Phipps. The surface ionization of potassium on tungsten. *Phys. Rev.*, 48:960–968, Dec 1935.

[29] A. S. Schlachter and T. J. Morgan. Formation of H^- by charge transfer in alkaline earth vapors. *AIP Conference Proceedings*, 111(1):149–161, 1984.

[30] A. Zelenski. Review of polarized ion sources. *Review of Scientific Instruments*, 81(2), 2010.

[31] M. Bacal. Physics basis and future trends for negative ion sources. *Review of Scientific Instruments*, 79(2):–, 2008.

[32] Y. Xu, A. K. Kazansky, and I. I. Fabrikant. Low-energy e-H_2 scattering: Separation of dissociative attachment and dissociation channels. *Phys. Rev. A*, 63:014703, Dec 2000.

[33] R. I. Hall, I. Čadež, M. Landau, F. Pichou, and C. Schermann. Vibrational excitation of hydrogen via recombinative desorption of atomic hydrogen gas on a metal surface. *Phys. Rev. Lett.*, 60:337–340, Jan 1988.

[34] J. R. Hiskes. Cross sections for the vibrational excitation of the $H_2X^1\Sigma_g^+(\nu)$ levels generated by electron collisional excitation of the higher singlet states. *Journal of Applied Physics*, 70(7):3409–3417, 1991.

[35] R. K. Janev, D. Reiter, and U. Samm. *Collision Processes in Low-temperature Hydrogen Plasma*. Berichte des Forschungszentrums Jülich. Forschungszentrum, Zentralbibliothek, 2003.

[36] B. Rasser, J. N. M. Van Wunnik, and J. Los. Theoretical models of the negative ionization of hydrogen on clean tungsten, cesiated tungsten and cesium surfaces at low energies. *Surface Science*, 118(3):697 – 710, 1982.

[37] J. K. Nørskov and B. I. Lundqvist. Secondary-ion emission probability in sputtering. *Phys. Rev. B*, 19:5661–5665, Jun 1979.

[38] W. G. Graham. Properties of alkali metals adsorbed onto metal surfaces. *2. international symposium on the production and neutralization of negative hydrogen ions and beams*, pages 126–133, 1980.

[39] O. Tarvainen, T. Kalvas, J. Komppula, H. Koivisto, E. Geros, J. Stelzer, G. Rouleau, K. F. Johnson, and J. Carmichael. Effect of Ion Escape Velocity and Conversion Surface Material on H^- Production. *AIP Conference Proceedings*, 1390(1):113–122, 2011.

[40] G. D. Alton. Semi-empimcal mathematical relationships for electropositive adsorbate induced work function changes. *Surface Science*, 175(1):226 – 240, 1986.

[41] R. F. Welton. Overview of high-brightness H^- ion sources. *Proceedings of LINAC2002, Gyeongju, Korea*, pages 559–563, 2002.

[42] D.P. Moehs, J. Peters, and Joseph Sherman. Negative hydrogen ion sources for accelerators. *Plasma Science, IEEE Transactions on*, 33(6):1786–1798, Dec 2005.

[43] F. F. Chen. *Introduction to plasma physics and controlled fusion; 2nd ed.* Springer, Boston, 1984.

[44] M. A. Lieberman and A. J. Lichtenberg. *Principles of plasma discharges and materials processing; 2nd ed.* Wiley, Newark, NJ, 2005.

[45] H. L. Pécseli. *Waves and Oscillations in Plasmas*. Series in Plasma Physics. CRC Press, Taylor & Francis Group, 2012.

[46] Vector Fields Opera, Cobham plc. `http://www.cobham.com/`.

[47] C. Schmitzer. *Characterisation of an inductively coupled plasma generator for the new Linac 4 H^- source at CERN*. PhD thesis, Technische Universität Wien, 2012.

[48] R. Becker and W. B. Herrmannsfeldt. igun—a program for the simulation of positive ion extraction including magnetic fields. *Review of Scientific Instruments*, 63(4):2756–2758, 1992.

[49] R. Becker. Mathematical Formulation and Numerical Modelling of the Extraction of H^- ions. *AIP Conference Proceedings*, 763(1):194–200, 2005.

[50] M. Reiser. *Theory and design of charged particle beams*. Wiley series in beam physics and accelerator technology. Wiley, New York, NY, 1994.

[51] I. Langmuir and K. B. Blodgett. Currents limited by space charge between concentric spheres. *Phys. Rev.*, 24:49–59, Jul 1924.

[52] J. R. Pierce. Rectilinear electron flow in beams. *Journal of Applied Physics*, 11(8):548–554, 1940.

[53] H. Liebl. *Applied Charged Particle Optics*. SpringerLink: Springer e-Books. Springer, 2008.

[54] CERN. *CAS - CERN Accelerator School, Ion Sources*, Geneva, 2013. CERN. Organised in collaboration with Slovak University of Technology in Bratislava.

[55] C. A. Valerio-Lizarraga, J.-B. Lallement, I. Leon-Monzon, J. Lettry, Ø. Midttun, and R. Scrivens. Space charge compensation in the Linac4 low energy beam transport line with negative hydrogen ions. *Review of Scientific Instruments*, 85(2):–, 2014.

[56] N. Chauvin, O. Delferrière, R. Duperrier, R. Gobin, P. A. P. Nghiem, and D. Uriot. Transport of intense ion beams and space charge compensation issues in low energy beam lines. *Review of Scientific Instruments*, 83(2), 2012.

[57] R. Gobin, P.-Y. Beauvais, R. Ferdinand, P.-A. Leroy, L. Celona, G. Ciavola, and S. Gammino. Improvement of beam emittance of the cea high intensity proton source silhi. *Review of Scientific Instruments*, 70(6):2652–2654, 1999.

[58] E. W. Thomas. Particle-impact induced electron ejection from surfaces. *INDC(NDS)-322*, Feb 1995.

[59] G. Lakits, A. Arnau, and H. Winter. Slow-particle-induced kinetic electron emission from a clean metal surface: A comparison for neutral and ionized projectiles. *Phys. Rev. B*, 42:15–24, Jul 1990.

[60] E. W. Thomas. Particle interactions with surfaces. *ORNL-6088/V3*, 3, 1985.

[61] W. M. Haynes. *Handbook of chemistry and physics*. CRC Press, New York, NY, 2013.

[62] R. A. Baragiola, E. V. Alonso, and A. Oliva Florio. Electron emission from clean metal surfaces induced by low-energy light ions. *Phys. Rev. B*, 19:121–129, Jan 1979.

[63] K. R. Crandall and Rusthoi D. P. *TRACE 3-D Documentation*, 1997.

[64] T. Kalvas. *Development and use of computational tools for modelling negative hydrogen ion source extraction systems*. PhD thesis, Department of Physics, University of Jyväskylä, 2013.

[65] J. E. Boers. A digital computer program for the simulation of positive or negative particle beams on a PC. *Particle Accelerator Conference, 1993., Proceedings of the 1993*, pages 327–329 vol.1, May 1993.

[66] R. Becker and W. B. Herrmannsfeldt. igun-A program for the simulation of positive ion extraction including magnetic fields. *Review of Scientific Instruments*, 63(4):2756–2758, 1992.

[67] P. Spädtke and S. Wipf. *KOBRA 3: a code for the calculation of space-charge-influenced trajectories in 3-dimensions*. GSI, Darmstadt, 1989.

[68] IBSimu web page. `http://http://ibsimu.sourceforge.net`.

[69] T. Kalvas, O. Tarvainen, H. Clark, J. Brinkley, and J. Arje. Application of 3D code IBSimu for designing an H^-/D^- extraction system for the Texas A&M facility upgrade. *AIP Conf.Proc.*, 1390:439–448, 2011.

[70] F. Gerigk and M. Vretenar. Design of a 120-MeV H^- linac for CERN high-intensity applications. Technical report, CERN, 2002.

[71] C. E. Hill, D. Kuchler, C. Mastrostefano, M. O'Neil, R. Scrivens, et al. H^- source developments at CERN. *Rev.Sci.Instrum.*, 77:03A521, 2006.

[72] J. Peters. Internal versus extrernal RF coupling into a volume source. *Proceedings of EPAC 2002*, pages 1727–1729, 2002.

[73] J. Peters. The new HERA H^- RF volume source. *Proceedings of LINAC2002, Gyeongju, Korea*, pages 422–424, 2002.

[74] B. X. Han, M. P. Stockli, R. F. Welton, S. N. Murray Jr., T. R. Pennisi, and M. Santana. Emittance characterization of the spallation neutron source H^- injector. *AIP Conference Proceedings*, 1515(1):473–480, 2013.

[75] J. Alessi. Performance of the Magnetron H^- Source on the BNL 200 MeV Linac. *AIP Conference Proceedings*, 642(1):279–281, 2002.

[76] J. Lettry et al. H^- ion sources for CERN's Linac4. *AIP Conference Proceedings*, 1515(1):302–311, 2013.

[77] A. Lombardi, C. Rossi, and M. Vretenar. Design of an RFQ Accelerator optimised for Linac4 and SPL. Technical Report AB-Note-2007-027. CERN-AB-Note-2007-027, CERN, Jun 2007.

[78] Ø. Midttun, T. Kalvas, M. Kronberger, J. Lettry, H. Pereira, C. Schmitzer, and R. Scrivens. A new extraction system for the Linac4 H^- ion source. *Review of Scientific Instruments*, 83(2):02B710, 2012.

[79] U. Fantz, P. Franzen, W. Kraus, H. D. Falter, M. Berger, S. Christ-Koch, M. Fröschle, R. Gutser, B. Heinemann, C. Martens, P. McNeely, R. Riedl, E. Speth, and D. Wünderlich. Low pressure and high power rf sources for negative hydrogen ions for fusion applications (ITER neutral beam injection). *Review of Scientific Instruments*, 79(2):–, 2008.

[80] E. Mahner, P. Chiggiato, J. Lettry, S. Mattei, M. O'Neil, H. Neupert, C. Pasquino, and C. Schmitzer. Gas injection and fast pressure-rise measurements for the Linac4 H^- source. *AIP Conference Proceedings*, 1515(1):425–432, 2013.

[81] J. Lettry, U. Fantz, M. Kronberger, T. Kalvas, H. Koivisto, J. Komppula, E. Mahner, C. Schmitzer, J. Sanchez, R. Scrivens, O. Midttun, P. Myllyperkiö, M. O'Neil, H. Pereira, M. Paoluzzi, O. Tarvainen, and D. Wünderlich. Optical emission spectroscopy of the Linac4 and superconducting proton Linac plasma generators. *Review of Scientific Instruments*, 83(2):–, 2012.

[82] H. Pereira, D. Faircloth, and J. Lettry. Operation and thermal modeling of the ISIS H^- source from 50 to 2 Hz repetition rates. *AIP Conference Proceedings*, 1515(1):114–120, 2013.

[83] S. Mattei, M. Ohta, M. Yasumoto, A. Hatayama, J. Lettry, and A. Grudiev. Plasma ignition and steady state simulations of the Linac4 H^- ion source. *Review of Scientific Instruments*, 85(2):–, 2014.

[84] T. Yamamoto, T. Shibata, M. Ohta, M. Yasumoto, K. Nishida, A. Hatayama, S. Mattei, J. Lettry, K. Sawada, and U. Fantz. Modeling of neutrals in the Linac4 H^- ion source plasma: Hydrogen atom production density profile and H_α intensity by collisional radiative model. *Review of Scientific Instruments*, 85(2):–, 2014.

[85] S. Mochalskyy, J. Lettry, T. Minea, Mattei S., and Ø. Midttun. Study of the different Cs conditioning states of the Linac4 negative hydrogen ion source by 3D PIC-MCC numerical simulations using ONIX code. *AIP Conference Proceedings*, 2015.

[86] M. Kronberger, D. Küchler, J. Lettry, Ø. Midttun, M. O'Neil, M. Paoluzzi, and R. Scrivens. Commissioning of the new H^- source for Linac4. *Review of Scientific Instruments*, 81(2):02A708, 2010.

[87] G. Bellodi, A. Akroh, O. Andreassen, J.-F. Comblin, V. Dimov, J.-B. Lallement, C. Martin, O. Midttun, E. Ovalle, U. Raich, F. Roncarolo, C. Rossi, R. Scrivens, J. Vollaire, M. Yarmohammadi Satri, and Z. Zocca. 3 MeV Test Stand commissioning report. Technical Report CERN-ACC-2013-0259, CERN, Geneva, Nov 2013.

[88] R. F. Welton, V. G. Dudnikov, B. X. Han, S. N. Murray, T. R. Pennisi, R. T. Roseberry, M. Santana, and M. P. Stockli. Developing reliable internal antennas and standardizing performance of H^- RF ion sources. *AIP Conference Proceedings*, 1515(1):341–348, 2013.

[89] M. Kronberger. Simulations of an alternative extraction system for the Linac4 H^- source. *Not published*, Sep 2011.

[90] D. Aguglia. Design of a system of high voltage pulsed power converters for CERN's Linac4 H^- ion source. In *Pulsed Power Conference (PPC), 2013 19th IEEE*, pages 1–6, June 2013.

[91] J. Lettry, M. Kronberger, R. Scrivens, E. Chaudet, D. Faircloth, G. Favre, J.-M. Geisser, D. Küchler, S. Mathot, O. Midttun, M. Paoluzzi, C. Schmitzer, and D. Steyaert. High duty factor plasma generator for CERN's Superconducting Proton Linac. *Review of Scientific Instruments*, 81(2):–, 2010.

[92] Vacuumschmelze GmbH & Co. *Rare-Earth permanent magnets Vacodym-Vacomax*, 2007.

[93] S. Mochalskyy, J. Lettry, T. Minea, A. F. Lifschitz, C. Schmitzer, O. Midttun, and D. Steyaert. Numerical modeling of the Linac4 negative ion source extraction region by 3D PIC-MCC code ONIX. *AIP Conf.Proc.*, 1515:31–40, 2012.

[94] A. Perrin, J. F. Amand, T. Mütze, J.-B. Lallement, and S. Lanzone. *Travel v4.07 User Manual*, 2007.

[95] Ø. Midttun, T. Kalvas, M. Kronberger, J. Lettry, H. Pereira, and R. Scrivens. A magnetized Einzel lens electron dump for the Linac4 H^- ion source. *AIP Conference Proceedings*, 1515(1):481–490, 2013.

[96] R. Scrivens, G. Bellodi, O. Crettiez, V. Dimov, D. Gerard, E. Granemann Souza, R. Guida, J. Hansen, J.-B. Lallement, J. Lettry, A. Lombardi, Ø. Midttun, C. Pasquino, U. Raich, B. Riffaud, F. Roncarolo, C. A. Valerio-Lizarraga, J. Wallner, M. Yarmohammadi Satri, and T. Zickler. Linac4 low energy beam measurements with negative hydrogen ions. *Review of Scientific Instruments*, 85(2):–, 2014.

[97] M. P. Stockli, R. F. Welton, and R. Keller. Self-consistent, unbiased root-mean-square emittance analysis. *Review of Scientific Instruments*, 75(5):1646–1649, 2004.

[98] Ø. Midttun, J. Lettry, and R. Scrivens. Measurements of Linac4 H^- ion source beam with a magnetized Einzel lens electron dump. *Review of Scientific Instruments*, 85(2), 2014.

[99] J. Peters. The New HERA H^- RF Volume Source and Selected Results of Plasma Investigations. *AIP Conference Proceedings*, 639(1):42–46, 2002.

[100] D. A. Fink, J. Lettry, Ø. Midttun, and R. Scrivens. Optimization of the beam extraction systems of the Linac4 H^- ion source. *AIP Conference Proceedings*, 2015.

[101] L. W. Swanson and R. W. Strayer. Field-Electro-Microscopy Studies of Cesium Layers on Various Refractory Metals: Work Function Change. *The Journal of Chemical Physics*, 48(6):2421–2442, 1968.